Cold atom physics using ultra-thin optical fibres

Dissertation

zur
Erlangung des Doktorgrades (Dr. rer. nat.)
der
Mathematisch-Naturwissenschaftlichen Fakultät
der
Rheinischen Friedrich-Wilhelms-Universität Bonn

vorgelegt von
Guillem Sagué Cassany
aus
Barcelona

Bonn 2008

Angefertigt mit Genehmigung
der Mathematisch-Naturwissenschaftlichen Fakultät
der Rheinischen Friedrich-Wilhelms-Universität Bonn

1. Gutachter: Prof. Dr. Dieter Meschede
2. Gutachter: Prof. Dr. Arno Rauschenbeutel

Tag der Promotion: 15.12.2008

Dedicat al meu germà Joan.

Lebenslauf

- 14.10.1979 Geburt in Barcelona (Spain).

- 1982-1986 Besuch der Grundschule Escola Dofí, Premià de Mar (Spain).

- 1986-1993 Besuch der Grundschule Escola Pere Vergés, Badalona (Spain).

- 1993-1996 Besuch des Kollegs Escola Pia de Diputació, Barcelona (Spain).

- 1996-1997 Besuch des Kollegs Institut Jaume Bofill, Barcelona (Spain)

- 1997-2003 Physikstudium. Universidad Autònoma de Barcelona, Barcelona (Spain)

- 2003-2004 Physikstudium (Austauschprogramm). Universidad de La Laguna, Tenerife (Spain).

- 2005- Beginn der Promotion, AG Meschede, Institut für Angewandte Physik, Rheinische Friedrich-Wilhelms Universität Bonn. Thema: *Cold atom physics using ultra-thin optical fibres.*

  - 2006 Anerkennung der *Licenciatura* als Physik-Diplom.
  - 2007 Publikation: G. Sagué, E. Vetsch, W. Alt, D. Meschede and A. Rauschenbeutel, *Cold Atom Physics Using Ultra-Thin Optical Fibers: Light-Induced Dipole Forces and Surface Interactions*, Phys. Rev. Lett. **99**, 163602 (2007).
  - 2008 Publikation: G. Sagué, A. Baade and A. Rauschenbeutel, *Blue-detuned evanescent field surface traps for neutral atoms based on mode interference in ultra-thin optical fibres*, New J. Phys. 10 113008 (2008).

Summary/Zusammenfassung

In this thesis I present experiments concerning the investigation and manipulation of cold neutral atoms using ultra-thin optical fibres with a diameter smaller than the wavelength of the guided light. In such a fibre-field configuration the guided light exhibits a large evanescent field that penetrates into the free-space surrounding the fibre thus enabling to couple laser cooled atoms to the fibre mode. By trapping and cooling caesium atoms in a magneto-optical trap formed around the fibre I investigated the interaction of the atoms with the evanescent field at sub-micrometre distances from the fibre surface.

Chapters 1 and 2 provide the theoretical foundations of this work. Chapter 1 describes the propagation of light in optical fibres. The general solution of the Maxwell's equations in the fibre that complements the description is provided in Appendix A. In Chapter 2, the theory of the interaction of atoms with time-varying electric fields is described.

In Chapter 3 the resonant interaction of laser cooled caesium atoms with the evanescent field of a probe laser launched through a 500-nm diameter fibre is studied. A detailed analysis of the atomic absorption at sub-micrometre distances from the fibre surface is given. I have performed Monte-Carlo simulations of atomic trajectories inside the cold atom cloud surrounding the fibre. From the simulations, the atomic density at the vicinity of the fibre is deduced and the absorbance profiles of the atoms measured during the experiments can be modelled. By carefully investigating the linewidths of these profiles, clear evidence of dipole forces, van der Waals interaction, and a significant enhancement of the spontaneous emission rate of the atoms is found.

The atomic spontaneous emission into the guided mode of a 500-nm diameter optical fibre is the focus of Chapter 4. Here, I show that the fibre can be used as an efficient tool to collect and guide the spontaneous emission of the atoms.

The dipole force induced by the evanescent field on the atoms is the central idea of the experiments performed in Chapter 5. I have built a new version of the experimental setup that opens the route towards atom trapping in the evanescent field in an array of surface microtraps around the fibre. Such traps are created by the combination of two laser fields with opposite sign of the detuning with respect to the excitation frequency of the atoms. The first experimental results reporting the influence of the two-colour evanescent field on the spectral properties of the atoms are presented.

Die vorliegende Arbeit berichtet über Experimente zur Untersuchung und Manipulation kalter neutraler Atome mittels ultradünner Glasfasern, deren Durchmesser kleiner als die Wellenlänge des geführten Lichts ist. In dieser Konfiguration besitzt die geführte Fasermode ein starkes evaneszentes Feld, das in den freien Raum um die Faser hineinreicht und damit die Kopplung kalter Cäsiumatome ermöglicht.

Die Kapitel 1 und 2 liefern die theoretischen Grundlagen dieser Dissertation. In Kapitel 1 werden die Eigenschaften der Lichtleitung in Glasfasern beschrieben. Die allgemeine Lösung der Maxwellgleichungen in der Faser liefert Anhang A. In Kapitel 2 wird die Theorie der Wechselwirkung neutraler Atome mit einem zeitabhängigen elektrischen Feld behandelt.

In Kapitel 3 wird die Wechselwirkung lasergekülter Atome mit dem evaneszenten Feld resonanter Laserstrahlung untersucht, die in einer Glasfaser mit einem Durchmesser von 500 nm geleitet wird. Es wird eine detaillierte Analyse der atomaren Absorption in einer Submikrometerentfernung von der Faseroberfläche präsentiert. Ich habe Monte-Carlo Simulationen von Trajektorien der lasergekühlten Atome durchgeführt. Daraus kann die atomare Dichte in der Nähe der Faser abgeleitet werden. Dies erlaubt die Modellierung der gemessenen atomaren Absorbanzkurven. Eine sorfältige Untersuchung der Linienbreite solcher Absorbanzkurven liefert eine deutliche Signatur lichtinduzierter Dipolkräfte, der van der Waals Kraft und einer Erhöhung der spontanen Emissionsrate der Atome.

Die spontane Emission in die Mode einer ultradünnen Glasfaser steht im Zentrum von Kapitel 4. Hier untersuche ich die Effizienz solcher Fasern als Werkzeug zum Sammeln und Übertragen atomarer spontanen Emission.

Die durch das evaneszente Feld induzierte Dipolkraft ist der Kerngedanke des Experiments von Kapitel 5. Ich habe eine erweiterte Version des expereimentellen Aufbaus entwickelt, die den Weg zum Fangen von Cäsiumatomen im evaneszenten Feld der Faser geebnet hat. Solche Fallen bestehen aus einer Kombination von zwei Lasern mit entgegengesetzter Verstimmung gegenüber der atomaren Anregungsfrequenz. Zudem werden die ersten Messungen des spektralen Einflusses des zweifarbigen evaneszenten Feldes auf die kalte Atomwolke präsentiert.

Parts of this thesis have been published in the following journal articles:

1. G. Sagué, E. Vetsch, W. Alt, D. Meschede and A. Rauschenbeutel, *Cold Atom Physics Using Ultra-Thin Optical Fibers: Light-Induced Dipole Forces and Surface Interactions*, Phys. Rev. Lett. **99**, 163602 (2007).

2. G. Sagué, A. Baade and A. Rauschenbeutel, *Blue-detuned evanescent field surface traps for neutral atoms based on mode interference in ultra-thin optical fibres*, New J. Phys. 10 113008 (2008).

Contents

Introduction

The interaction of light and matter at the fundamental level, where a single photon efficiently interacts with a single atom, has been one of the main research topics in quantum optics over the last decades [1–3]. Since the absorption cross-section of the an atom on resonance is on the order of the wavelength of the absorbed light ($\sim \lambda^2$) such interaction is in general very weak [4]. Many approaches have been conceived to enhance this interaction. One possibility is to use high atomic densities to store single photons in a whole ensemble of atoms as a collective single-photon excitation [5–7]. Another possibility is to modify, tailor or store the light field used for the interaction. In this context, one of the most widely used approaches to tackle the problem is the use of resonant structures [8–10]: One photon trapped in a high finesse resonator, passes through the position of the atom a few million times before leaking out from the cavity, thereby increasing the coupling probability [11]. Moreover, the use of dielectric structures such as microspheres or microtoroids to store the light propagating in whispering gallery modes has undergone high development in recent years [12, 13]. This approach has, in addition, the advantage that such dielectric structures are cheap, robust and scalable [14], which is a necessary condition for building a quantum computer [15].

Nevertheless, the 3-dimensional confinement is not a requirement to increase the interaction between light and matter using tailored light fields. For example, a laser beam which is strongly focused at the position of the atom also leads to an enhanced atomphoton coupling [16]. This method has, however, some limitations due to, e. g., the non-uniformity of the polarisation of the field at the focus [17]. Indeed, the photon that induces an absorption with 100% probability must reproduce the spatial, temporal and polarisation properties of the atomic radiation. This requirement has been assessed in a recent theoretical proposal where a laser beam is focused in such a way that the emission pattern of a classical dipole is reproduced at the focal point of a parabolic mirror [18].

Waveguides and prisms are also suited to tailor light fields and use them to couple atoms. In this case, the interaction takes place in the optical near field close to the surface of the dielectric [19], leading to modified spectral and radiative properties of the atoms [20]. The evanescent field arising from the internal reflection of a laser beam in a prism has been used in several experiments to investigate and cool alkali atoms at a few micrometres above the surface of the dielectric [21–23]. Many other efforts have been focused on the mechanical control of atoms using the strong non-dissipative forces arising

in non-resonant evanescent fields. Evanescent wave mirrors for neutral atoms [24, 25] and atom trapping above dielectric waveguides [26–28] are some examples. The latter has not been yet experimentally demonstrated.

Optical fibres also count among the dielectric structures that enable tailoring of the propagation properties of the light. The light guided in the core of a standard telecommunications optical fibre is isolated from the environment allowing low loss transmission over long distances [29]. This property has not only been used in telecommunications but also in quantum optics experiments to, e. g., demonstrate the quantum interference of two indistinguishable photons [30] or to transmit quantum cryptography keys encoded in the polarisation of the emitted photons [31]. On the other hand, the use of optical fibres to enhance and control the interaction between light and matter is an innovative aspect that has recently attracted much attention [32–35]. In this work I demonstrate that ultra-thin optical fibres are good candidates for this issue.

Standard telecommunication optical fibres can be tapered in our custom-made pulling facility at the University of Mainz down to diameters as small as 100 nm [36]. Such tapered optical fibres (TOF) offer a strong transverse confinement of the guided mode while exhibiting a pronounced evanescent field surrounding the fibre [37]. This allows to efficiently couple atoms to the guided fibre mode at sub-micrometre distances from the fibre surface [35]. I have built an experimental setup that allows to couple laser-cooled caesium atoms to the evanescent field by inserting the waist of a 500-nm diameter TOF into a magneto-optical trap (MOT). A rigorous analysis of the resonant interaction of the atoms with the evanescent field as a function of the probe laser power shows clear evidence of light-induced dipole forces and surface interactions (Chapter 3). The latter includes the van der Waals (v.d.W.) potential and a significant enhancement of the spontaneous emission rate of the atoms near the fibre surface.

Moreover, an ultra-thin optical fibre can be used to probe the fluorescence of laser-cooled atoms in the MOT. The experimental results demonstrate the efficiency of the TOF as a tool to collect and guide the spontaneous emission of the atoms (Chapter 4). The measured spontaneous emission rate into the guided mode at the surface of the fibre is, in addition, in good agreement with the theoretical calculations published in [38].

In the last part of my work I describe a new version of the experiment that enables to couple two additional far-detuned lasers into the fibre following the theoretical proposal from [39] (Chapter 5). When the laser fields have two opposite signs of the detuning with respect to the atomic transition frequency, a two-colour dipole trap for caesium atoms in the evanescent field of an ultra-thin optical fibre can be created. This opens the route towards atom trapping and manipulation using ultra-thin optical fibres. The creation of ensembles of fibre-coupled atoms at a fixed distance from the fibre surface, is a very promising framework for slow light experiments [40], or the realisation of two-photon gates in non-linear media [41].

Chapter 1

Light propagation in step-index optical fibres

Optical fibres are key elements in modern telecommunications since they allow the transmission of information over large distances in channels isolated from the environment. The structure of a circular step-index optical fibre is shown in Fig. 1.1 (a). Only circular step-index optical fibres will be considered in this thesis and will be simply referred to as optical fibres. The cladding is typically made of silica (SiO_2) and the core of silica doped with Germanium ions to produce an increase in the refractive index of about 1%. The refractive index profile of an optical fibre is schematically shown in Fig. 1.1 (b). The
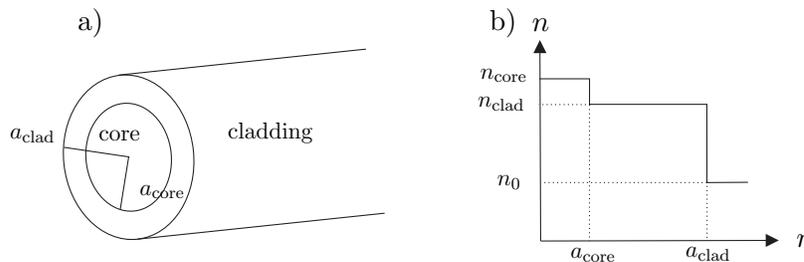
FIGURE 1.1: (a) Geometry of a step-index circular optical fibre. The diagram is not at scale. (b) Schematic refractive index profile of a step-index fibre as a function of the distance from the fibre axis. The core has a larger refractive index than the cladding. n_0 denotes the refractive index of the surrounding medium.

step-wise decrease of the refractive index n at the boundary between the core and the cladding allows radial confinement of the light via total internal reflection [42]. The ratio between the radius of the core and the cladding lies between 1/30 and 1/10 in standard optical fibres. A large cladding radius is necessary because the small refractive index difference at the core-cladding boundary results in a penetration of the field into the cladding in the form of an evanescent wave. The evanescent field decays approximately

exponentially inside the cladding, allowing part of the light to axially propagate outside the core. The presence of light outside the core is one of the theoretical foundations of this work and will be extensively treated in the next Chapters. The typical parameters of a standard fibre with the single-mode cut-off at 760 nm (see Sect. 1.2) are shown in Table 1.1. The parameter Θ in Eq. 1.1 is referred to as the numerical aperture of the

Single mode fibre
$a_{clad} = 62.5 \ \mu\mathrm{m}$
$2 \ \mu\mathrm{m} \leq a_{core} \leq 5 \ \mu\mathrm{m}$
$n_{clad} = 1.452$ (fused quarz)
$0.06 \leq \Theta \leq 0.15$

TABLE 1.1: Typical parameters and dimensions of a standard fibre with single-mode cutoff at 760 nm. Since the refractive index of silica is frequency dependent [43], the value for n_{clad} has been calculated at a wavelength of 852 nm.

fibre and plays a similar role as the numerical aperture of a lens (see Fig. 1.2).

$$\Theta = \sqrt{n_{core}^2 - n_{clad}^2}. \tag{1.1}$$

1.1   Ray propagation in optical fibres

In this section some fundamental properties of light propagation inside optical fibres will be discussed in the frame of geometric optics: The coupling of light into an optical fibre, characterised by its numerical aperture (NA) (Sec. 1.1.1), and the nature of the different modes of propagation in the fibre (Sec. 1.1.2) determined by the exact solutions of the Maxwell equations. Geometric optics provides useful tools for intuitively understanding these basic principles of light propagation in optical fibres. However, due to the wave character of light some of the features from single-mode and ultra-thin optical fibres, cannot be explained using this interpretation [29]. One should thus keep in mind that the results exposed in this section are rather qualitative.

1.1.1   Numerical aperture of a fibre

The numerical aperture of a fibre is defined as the sine of the maximal angle that a incoming ray can have at the fibre input and still be guided. The propagation of a light ray inside an optical fibre by means of total internal reflection is shown in Fig. 1.2. The ray does not escape from the core as long as the incidence angle at the core-cladding interface θ remains smaller than the critical angle θ_c for the total internal reflection condition at the core-cladding boundary given by

$$\theta \leq \theta_c = \arccos\left[\frac{n_{clad}}{n_{core}}\right]. \tag{1.2}$$
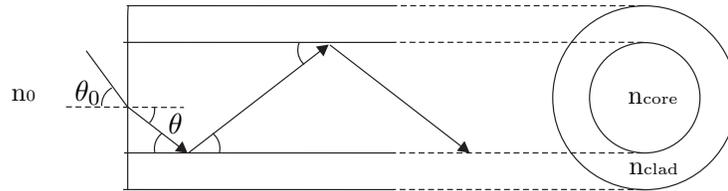
FIGURE 1.2: Schematic of the propagation of a light ray in an optical fibre.

Snell's law determines θ for a given incidence angle θ_0 at the fibre input,

$$n_0 \sin[\theta_0] = n_{core} \sin[\theta]. \tag{1.3}$$

Combining Eqns. (1.2) and (1.3), and assuming $n_0 = 1$ the condition for a ray to be guided when entering the fibre reads

$$\sin[\theta_0] \leq \sqrt{n_{core}^2 - n_{clad}^2}. \tag{1.4}$$

1.1.2   Hybrid and Transverse modes

The exact solutions of the Maxwell equations in the fibre lead to four differentiated set of propagation modes: the hybrid modes HE and EH, having 6 non-vanishing components of the electromagnetic field, and the transverse modes TE (*transversal electric*) and TM (*transversal magnetic*) that have, at least, one vanishing component. Note that, for reasons of symmetry, this is only true for the cylindrical components of the fields. Figure 1.3 shows the propagation of a light ray spiraling in the fibre (*skew ray*). Since
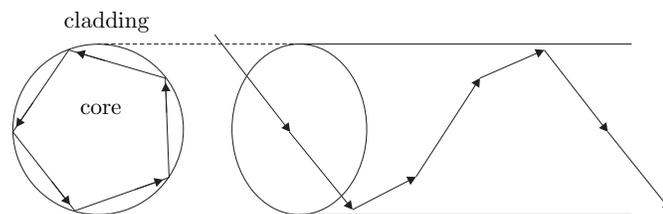
FIGURE 1.3: Schematic of the propagation of a skew ray in an optical fibre. For simplicity it is assumed the ray trajectory has a closed loop around the fibre axis.

the component of the electric field perpendicular to the surface acquires a phase shift equal to π after each reflection while the parallel component remains unchanged all the polarisation components will be mixed during the propagation. Therefore, in ray trajectories that rotate around the fibre axis, no field components will be zero. The *skew rays* thus constitute the hybrid modes HE and EH [29]. The transverse TE and TM modes imply, consequently, non-rotating trajectories, i. e., rays that lie in a plane comprising the fibre axis. Figure 1.4 shows the propagation of such *meridional rays*

a)

TE

b)

TM
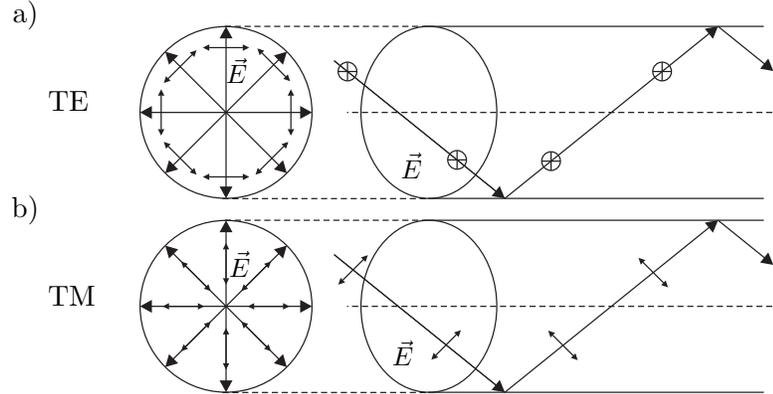
FIGURE 1.4: Propagation of the TE (a) and TM (b) modes in an optical fibre. $\vec{E}$ refers to the electric field polarisation. For simplicity, only the propagation of vertical rays are sketched on the right side.

with their corresponding polarisation of the electric field. Note that the polarisation of both modes will not be mixed after each reflection. When using cylindrical coordinates the TE modes have two vanishing components of the electric field, E_r and E_z. On the other hand, the TM modes have a vanishing azimuthal component of the electric field E_ϕ and non-vanishing E_r and E_z components. This becomes manifest in Fig. 1.4 (b) where the polarisation of the propagating light ray has a fixed value of its projection along the fibre axis. The refractive index difference at the boundary and the orientation of the electric field component transversal to the propagation direction $\vec{E}_\perp = (E_x, E_y)$ influence the z-component of the electric field. When $\vec{E}_\perp$ is perpendicular to the fibre surface a non-vanishing z-component of the electric field arises. Moreover, the Maxwell equations allow approximative solutions of the fields propagating in an optical fibre under the weakly guiding condition

$$\sqrt{n_{core}^2 - n_{clad}^2} \ll 1. \tag{1.5}$$

Under this condition, θ_c, defined in Eq. (1.2), is small since $n_{clad}/n_{core} \approx 1$ and the modes will satisfy:

$$\mid E_z \mid \ll \mid E_{r,\phi} \mid . \tag{1.6}$$

These modes are called LP (*linearly polarised*) modes and their detailed mathematical description can be found in [44].

1.2 Solutions for the fields in an optical fibre: HE, EH, TE and TM modes

The geometry of a vacuum-clad optical fibre that will be considered in the remainder of this work is shown in Fig. 1.5. Because of the symmetry properties of the fibre a
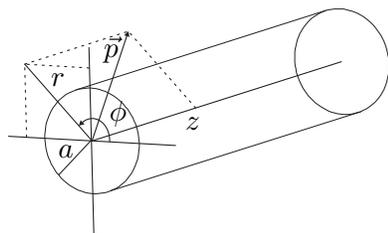
$$n(r) = \left\{ \begin{array}{ll} n_1 & \text{if } r < a \\ n_2 & \text{if } r > a \end{array} \right. \text{ with } n_1 > n_2$$

(1.7)

FIGURE 1.5: Geometry and coordinate system of a step-index optical fibre.

cylindrical coordinate system is chosen. Equation (1.7) gives the radial dependency of the refractive index. The bulk at $r < a$ acts as a waveguide playing the role of the core in a standard optical fibre while the surrounding medium in $r > a$ plays the role of the cladding, producing a step-wise decrease of the refractive index at the boundary $r = a$ that allows the guiding of the fields. Both media are assumed to be non-absorbing and to have a magnetic permeability equal to the vacuum permeability μ_0. The solutions for the fields propagating in such a fibre can be found in Appendix A and will not be explicitly given here.

The condition for the continuity of the fields at the boundaries given by Eqns. (A.28) leads to the following transcendental equation for the propagation constant β:

$$\left(\frac{J_l'(ha)}{haJ_l(ha)} + \frac{K_l'(qa)}{qaK_l(qa)} \right) \left(\frac{n_1^2 J_l'(ha)}{haJ_l(ha)} + \frac{n_2^2 K_l'(qa)}{qaK_l(qa)} \right) = \left(\frac{l\beta}{k_0} \right)^2 \left[\left(\frac{1}{ha} \right)^2 + \left(\frac{1}{qa} \right)^2 \right]^2, \quad (1.8)$$

where $J_l(x)$ is the Bessel function of the first kind and $K_l(x)$ the modified Bessel function of the second kind, $J_l'(hr)$ $(K_l'(qr))$ denotes $dJ_l(hr)/d(hr)$ $(dK_l(qr)/d(qr))$, $\varepsilon_1 = n_1^2 \varepsilon_0$ is the dielectric constant of the fibre, $\varepsilon_2 = n_2^2 \varepsilon_0$ is the dielectric constant of the surrounding medium and $l = 0, 1, 2, ...$ The following quantities have also been introduced:

$$h = \sqrt{n_1^2 k_0^2 - \beta^2},$$
$$q = \sqrt{\beta^2 - n_2^2 k_0^2}.$$

(1.9)

The propagation constant of the fields is defined as such β that the solution of the electric field reads

$$\vec{E} \sim \exp[-i(\beta z - \omega t)].$$

(1.10)

By numerically solving Eq. (1.8) we obtain a discrete set of values for β, each of them corresponding to a different propagation mode in the fibre. This is a widespread result in physics which occurs when confining waves in one or more dimensions. The solutions of a particle confined in a potential well in quantum mechanics or the harmonics in a chord are some examples.

It is convenient to solve Eq. (1.8) by isolating $J_l'(ha)/haJ_l(ha)$ and by making use of

the relations

$$
\begin{aligned}
J_l'(x) &= J_{l-1}(x) - \frac{l}{x}J_l(x), \\
K_l'(x) &= -\frac{1}{2}[K_{l-1}(x) + K_{l+1}(x)],
\end{aligned}
\tag{1.11}
$$

to obtain

$$
\frac{J_{l-1}(ha)}{haJ_l(ha)} = \left(\frac{n_1^2 + n_2^2}{2n_1^2}\right)\frac{K_{l-1}(qa) + K_{l+1}(qa)}{2qaK_l(qa)} + \frac{l}{(ha)^2} \pm R,
\tag{1.12}
$$

with

$$
R = \left[\left(\frac{n_1^2 - n_2^2}{2n_1^2}\right)^2\left(\frac{K_{l-1}(qa) + K_{l+1}(qa)}{2qaK_l(qa)}\right)^2 + \left(\frac{l\beta}{n_1k_0}\right)^2\left(\frac{1}{(qa)^2} + \frac{1}{(ha)^2}\right)^2\right]^{1/2}.
\tag{1.13}
$$

The $\pm$ signs in Eq. (1.12) stem from Eq. (1.8), which is quadratic in $J_l'(ha)/haJ_l(ha)$, leading to two different sets of modes, the HE ($-$) and EH ($+$). This designation is based on the contribution of E_z and H_z to the mode: E_z is larger (smaller) than H_z for the EH (HE) modes [44]. Within each set of modes exist different solutions depending on the value l. Hence, the modes are labelled as EH_{lm} and HE_{lm} where m accounts for the different solutions of Eq. (1.12) for a fixed l. Two special cases are those with $l = 0$: TM, for the solutions EH_{0m}, and TE, for the solutions HE_{0m}. The differentiated naming of these solutions stems from the special propagation properties of the TM and TE modes explained in Sec. 1.1.

Figure 1.6 shows the graphical solution of Eq. (1.12) for the EH_{1m} modes. The left- and right-hand sides of Eq. (1.12) have been plotted as a function of the parameter ha for $l = 1$. The intersections correspond to the propagating modes in the fibre, starting with $m = 1$ at the first crossing. The right-hand side of Eq. (1.12) diverges at $ha = V$, where V is a fundamental parameter for the fibre-field system given by

$$
V = \frac{2\pi a}{\lambda}\sqrt{n_1^2 - n_2^2}.
\tag{1.14}
$$

Note that there is a lower limit in V for the EH_{1m} modes that can propagate in the fibre. Indeed, it can be shown that all EH_{lm} modes have a cut-off value given by the m roots of $J_l(ha) = 0$, e. g., $ha = 3.832$ for EH_{11}, $ha = 7.016$ for EH_{12}, and $ha = 10.173$ for EH_{13}. The EH modes are hybrid, i. e., they have six non-vanishing components of the fields and, as shown in Sec. 1.1, their propagation can be understood in geometric optics as *skew rays* spiraling around the fibre axis.

Figure 1.7 shows the graphical solution of Eq. (1.12) for the HE_{1m} modes. Note that the HE_{11} mode has no cut-off. The HE_{11} can thus always propagate and, therefore, will be referred to as the fundamental mode of the fibre. The HE modes are also hybrid, i. e., they have six non-vanishing components of the fields.

Let us now consider the two special cases where $l = 0$. The graphical solutions of EH_{0m} have been plotted in Fig. 1.8. These are labelled as TM modes (transversal magnetic)

FIGURE 1.6: Solution of the EH modes (+) for $l = 1$ at $V = 11.03$. The left- and right-hand sides of Eq. (1.12) have been labelled A and B, respectively.

because the magnetic field $\vec{H}$ is perpendicular to the fibre axis. Furthermore, $E_\phi = 0$ and $H_r = 0$, leaving H_ϕ, E_r and E_z as the only non-vanishing components. This is in accordance with the geometric optics interpretation of the TM modes given in Sec. 1.1. The cutoff for the TM_{01} lies at $V = 2.405$. This is the lowest cutoff value for any non-fundamental mode to propagate inside fibre and thus sets the single mode condition given by

$$V < 2.405. \tag{1.15}$$

Hence, when this inequality holds only the fundamental mode HE_{11} can propagate. This property has important applications in the telecommunications technology because single-mode propagation allows better control of the group velocity of the signals [42]. The HE_{0m} modes shown in Fig. 1.9 have a similar behavior as the EH_{0m} modes. These are labelled TE (transversal electric) because $E_z = 0$. Furthermore, $E_r = 0$ and $H_\phi = 0$, leaving E_ϕ, H_r and H_z as the only non-vanishing components. The cutoff for TE and TM coincides, TE_{01} and TM_{01} therefore being the first two higher-order modes. Again, the fields in the TE modes are in accordance with its interpretation in geometric optics. The

labelling	sign	l	field components
EH	+	> 0	E_z, E_r, E_ϕ, H_z, H_r, H_ϕ
HE	−	> 0	E_z, E_r, E_ϕ, H_z, H_r, H_ϕ
TM	+	0	E_z, E_r, H_ϕ
TE	−	0	E_ϕ, H_z, H_r

TABLE 1.2: Summary of the different modes hosted in the fibre indicating their l values and field components. The column labelled as "sign" refers to the two possible branches of solutions of Eq. (1.12)

different solutions of Eq. (1.12) have been summarised in Table (1.2). In the following, the EH_{0m} and HE_{0m} modes will be referred to as TM_{0m} and TE_{0m}, respectively.
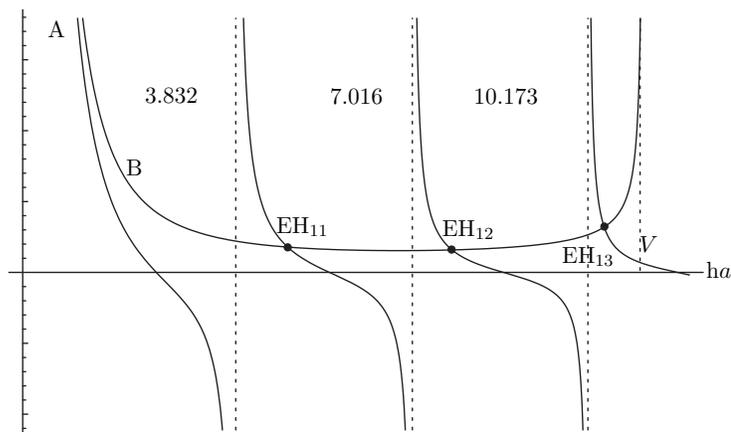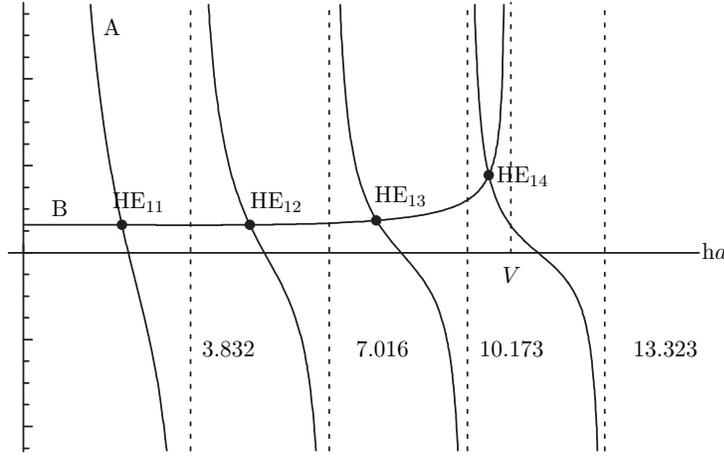
FIGURE 1.7: Solution of the HE modes $(-)$ for $l = 1$ at $V = 11.03$. The left- and right-hand sides of Eq. (1.12) have been labelled A and B, respectively.

Let us now examine the dependence of the propagation constant β as a function of the parameter V shown in Fig. 1.10. Here, the single-mode and multi-mode regimes can be clearly distinguished. The first two excited modes TE_{01} and TM_{01} appear for $V \geq 2.405$. When decreasing (increasing) the V parameter, β/k_0 tends to n_2 (n_1). This illustrates the fact that by decreasing the radius of the fibre or increasing the wavelength of the light, the fields will penetrate more into the surrounding medium. In the inverse situation, the fields will be guided mostly in the bulk.

1.2.1 The fundamental HE$_{11}$ mode: Rotating polarisation

I now present the field equations of the fundamental HE_{11} mode with rotating polarisation. From the solutions of the Maxwell equations given in Appendix A, the equations for the electric field $\vec{E}$ can be obtained.

For $r < a$:

$$E_r(r, \phi, z, t) = -iA\frac{\beta_{11}}{2h_{11}}[(1 - s_{11})J_0(h_{11}r) - (1 + s_{11})J_2(h_{11}r)]\exp[i(\omega t \pm \phi - \beta_{11}z)],$$

$$E_\phi(r, \phi, z, t) = \pm A\frac{\beta_{11}}{2h_{11}}[(1 - s_{11})J_0(h_{11}r) + (1 + s_{11})J_2(h_{11}r)]\exp[i(\omega t \pm \phi - \beta_{11}z)],$$

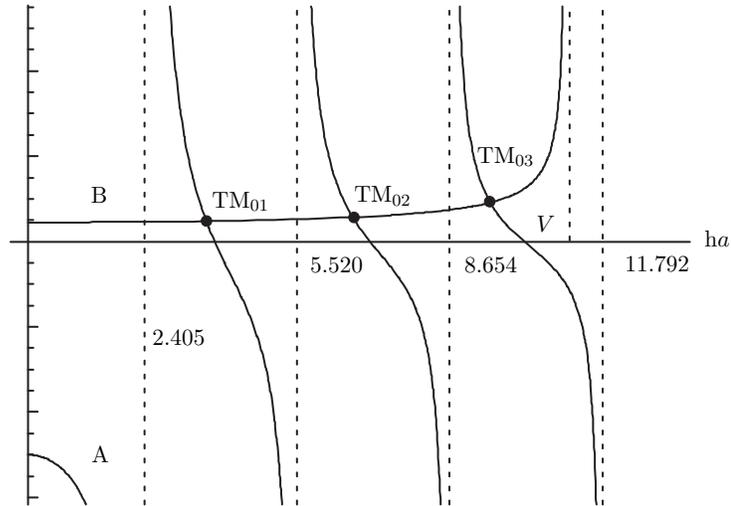$$E_z(r, \phi, z, t) = AJ_1(h_{11}r)\exp[i(\omega t \pm \phi - \beta_{11}z)]. \tag{1.16}$$

FIGURE 1.8: Solution of the TM modes of Eq. (1.12) at $V = 11.03$. The left- and right-hand sides of Eq. (1.12) have been labelled A and B, respectively.
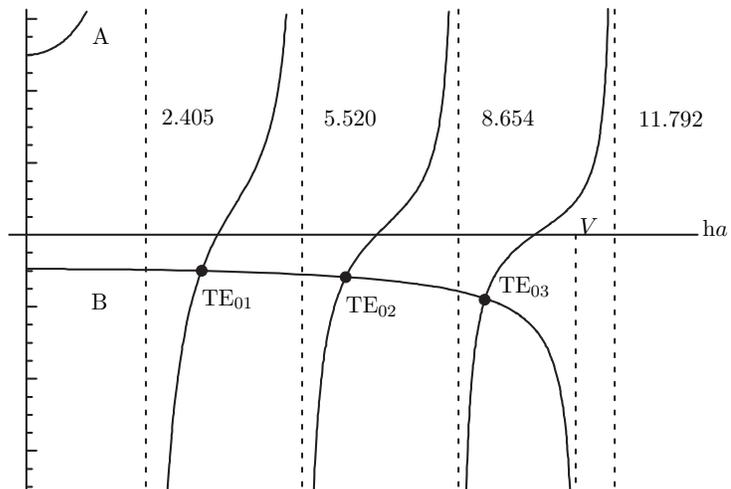
FIGURE 1.9: Solution of the TE modes at $V = 11.03$. The left- and right-hand sides of Eq. (1.12) have been labelled A and B, respectively.
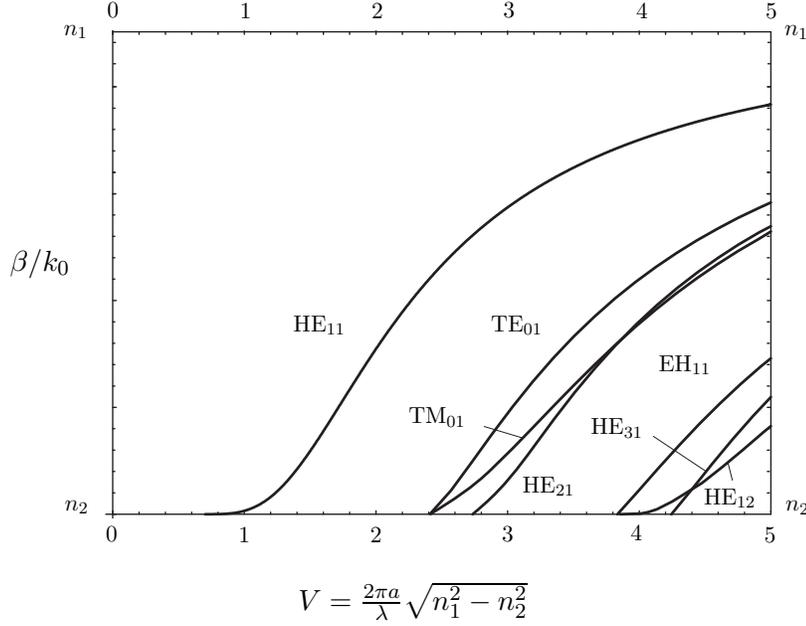
FIGURE 1.10: Normalised propagation constant β/k_0 as a function of V for the first seven modes of the fibre.

For $r > a$:

$$
\begin{aligned}
E_r(r,\phi,z,t) = &- iA\frac{\beta_{11}}{2q_{11}}\frac{J_1(h_{11}a)}{K_1(q_{11}a)}[(1-s_{11})K_0(q_{11}r) + (1+s_{11})K_2(q_{11}r)] \\
&\exp[i(\omega t \pm \phi - \beta_{11}z)],
\end{aligned}
$$

$$
\begin{aligned}
E_\phi(r,\phi,z,t) = &\pm A\frac{\beta_{11}}{2q_{11}}\frac{J_1(h_{11}a)}{K_1(q_{11}a)}[(1-s_{11})K_0(q_{11}r) - (1+s_{11})K_2(q_{11}r)] \\
&\exp[i(\omega t \pm \phi - \beta_{11}z)],
\end{aligned}
$$

$$
E_z(r,\phi,z,t) = A\frac{J_1(h_{11}a)}{K_1(q_{11}a)}K_1(q_{11}r)\exp[i(\omega t \pm \phi - \beta_{11}z)], \tag{1.17}
$$

where,

$$
\begin{aligned}
s_{11} &= \left[\frac{1}{(h_{11}a)^2} + \frac{1}{(q_{11}a)^2}\right]\left[\frac{J_1'(h_{11}a)}{h_{11}aJ_1(h_{11}a)} + \frac{K_1'(q_{11}a)}{q_{11}aK_1(q_{11}a)}\right]^{-1} \\
h_{11} &= \sqrt{k_0^2n_1^2 - \beta_{11}^2} \\
q_{11} &= \sqrt{\beta_{11}^2 - k_0^2n_2^2} \tag{1.18}
\end{aligned}
$$

The $+(-)$ sign in the equations above accounts for clockwise (counterclockwise) rotation of the polarisation around the fibre axis. The normalisation constant A of the fields links the power carried by the mode to the maximal field amplitude and can be determined with use of Eq. (1.23) below.
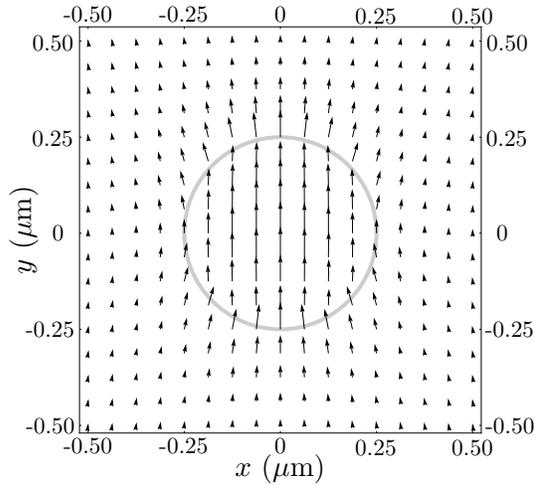
FIGURE 1.11: Field plot of the electric field component perpendicular to the fibre axis $\vec{E}_\perp$ in the HE$_{11}$ mode for rotating polarisation at $t = 0$ and $z = 0$. The following parameters have been assumed: $n_1 = 1.452$, $n_2 = 1$, $a = 250$ nm and $\lambda = 852$ nm.
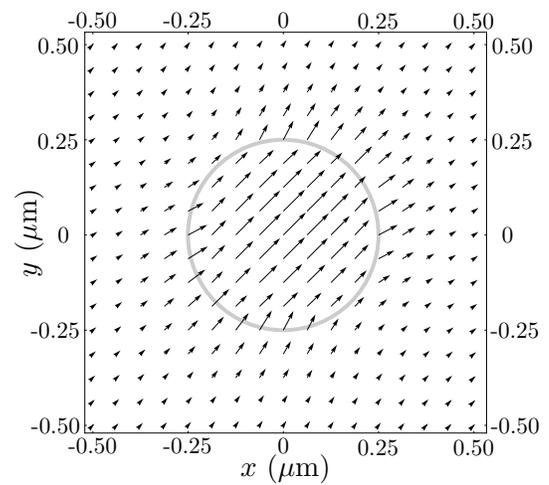
FIGURE 1.12: Field plot of $\vec{E}_\perp$ in the HE$_{11}$ mode for rotating polarisation at $t = \pi/4\omega$ and $z = 0$ for the same parameters as in Fig. 1.11.
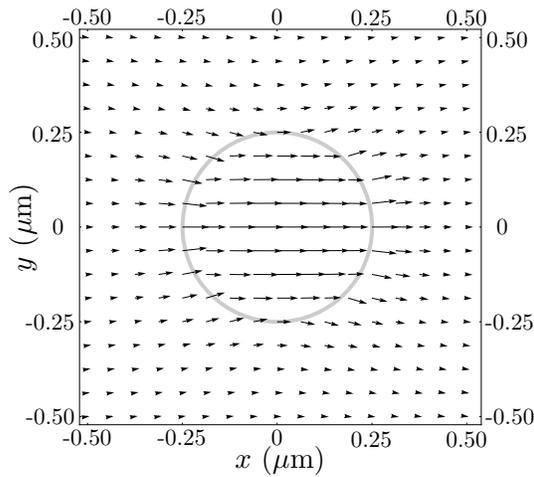
FIGURE 1.13: Field plot of $\vec{E}_\perp$ in the HE$_{11}$ mode for rotating polarisation at $t = \pi/2\omega$ and $z = 0$ for the same parameters as in Fig. 1.11.
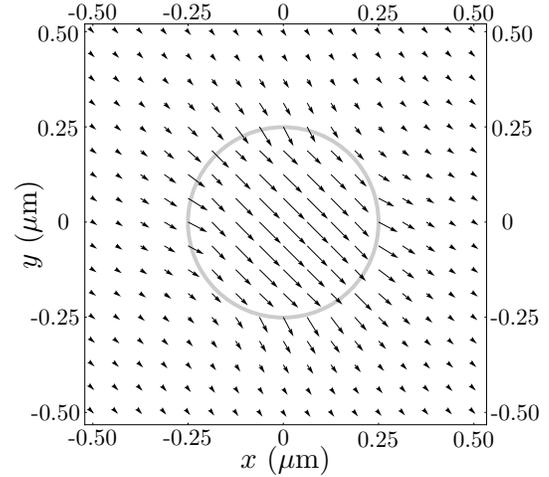
FIGURE 1.14: Field plot of $\vec{E}_\perp$ in the HE$_{11}$ mode for rotating polarisation at $t = 3\pi/4\omega$ and $z = 0$ for the same parameters as in Fig. 1.11.

Figures 1.11, 1.12, 1.13 and 1.14 are vector plots of the electric field component transversal to the fibre axis $\vec{E}_{\perp} = (E_x, E_y)$ at $z = 0$ and $t = 0$, $t = \pi/4\omega$, $t = 2\pi/4\omega$ and $t = 3\pi/4\omega$, respectively. The fibre surface is indicated by a grey circle. The calculations have been performed for a fibre of pure silica ($n_1 = 1.452$) with a radius $a = 250$ nm, surrounded by vacuum ($n_2 = 1$) at a wavelength of $\lambda = 852$ nm. These fibre and wavelength parameters correspond to the experiments presented in Chaps. 3, 4, and 5. As expected, $\vec{E}_{\perp}$ rotates in time with respect to the fibre axis. However, the rotation is not perfectly circular but elliptical and the ellipticity is position dependent. The position of maximal ellipticity is located at the surface of the fibre. This stems from the boundary conditions for the electric field [37], which lead to a discontinuity in the E_r component at the fibre surface. This produces a radial orientation of the ellipse, its long (short) axis being oriented perpendicular (parallel) to the fibre surface, which becomes apparent when comparing the point (0 μm, 0.25 μm) in Figs. 1.11 and 1.13.

The absolute value of the squared electric field averaged over one oscillation period $\left|\vec{E}(r)\right|^2$ in the HE_{11} mode is given by

$$\left.\left|\vec{E}(r)\right|^2\right|_{\mathrm{in}} = \frac{A^2 \beta_{11}^2}{2h_{11}^2}\left[(1 - s_{11})^2 J_0^2(h_{11}r) + (1 + s_{11})^2 J_2^2(h_{11}r) + 2\frac{h_{11}^2}{\beta_{11}^2}J_1^2(h_{11}r)\right], \quad (1.19)$$

$$\left.\left|\vec{E}(r)\right|^2\right|_{\mathrm{out}} = \frac{A^2 \beta_{11}^2}{2q_{11}^2}\frac{J_1^2(h_{11}a)}{K_1^2(q_{11}a)}\left[(1 - s_{11})^2 K_0^2(q_{11}r) + (1 + s_{11})^2 K_2^2(q_{11}r) + 2\frac{q_{11}^2}{\beta_{11}^2}K_1^2(q_{11}r)\right], \quad (1.20)$$

where $|\vec{E}(r)|^2_{\mathrm{in}}$ ($|\vec{E}(r)|^2_{\mathrm{out}}$) denotes the time-averaged squared electric field inside (outside) the fibre. Since the above equations do not depend on ϕ, the distribution of $\left|\vec{E}(r)\right|^2$ is cylindrically symmetric. This stems from the averaging of the squared $\vec{E}$ field over one oscillation period. As shown in Figs. 1.11 – 1.14, the electric field propagating in the fibre is, in general, not cylindrically symmetric because the polarisation of the field brakes the symmetry. However, for rotating polarisation, averaging over one period washes out this symmetry breaking.

Equations (1.19) and (1.20) are useful for estimating the relative strength of the z-component of the electric field $\vec{E}$ yielding $|E_z(r = a)|^2_{\mathrm{in}}/|\vec{E}(r = a)|^2_{\mathrm{in}} = 0.2$ and $|E_z(r = a)|^2_{\mathrm{out}}/|\vec{E}(r = a)|^2_{\mathrm{out}} = 0.1$. This feature does not exist in free propagating beams, where $\vec{E}$ and $\vec{H}$ are perpendicular to the propagation vector $\vec{k}$. Again, the discontinuity at the boundary is produced by the E_r component of the field because, although E_z is continuous at the surface, $\left|\vec{E}(r)\right|^2$ is not.

Figure 1.15 shows the distribution of $\left|\vec{E}(r)\right|^2_{\mathrm{in}}$ (inside) and $\left|\vec{E}(r)\right|^2_{\mathrm{out}}$ (outside) normalised to the value $\left|\vec{E}(r = a)\right|^2_{\mathrm{out}}$ (surface) as a function of x and y. The regions where $r < a$ and $r > a$ can be clearly identified due to the discontinuity at the boundary $r = a$. This strong discontinuity arises from the large refractive index difference between the bulk and the surrounding medium and from the strong radial confinement of the field when $\lambda > a$. The strength of the evanescent field $\left|\vec{E}(r)\right|^2_{\mathrm{out}}$ around the fibre is apparent in Fig. 1.16: $\left|\vec{E}(r = a)\right|^2_{\mathrm{out}}$ is about 58% of $\left|\vec{E}(r = 0)\right|^2_{\mathrm{in}}$ and almost twice as large as
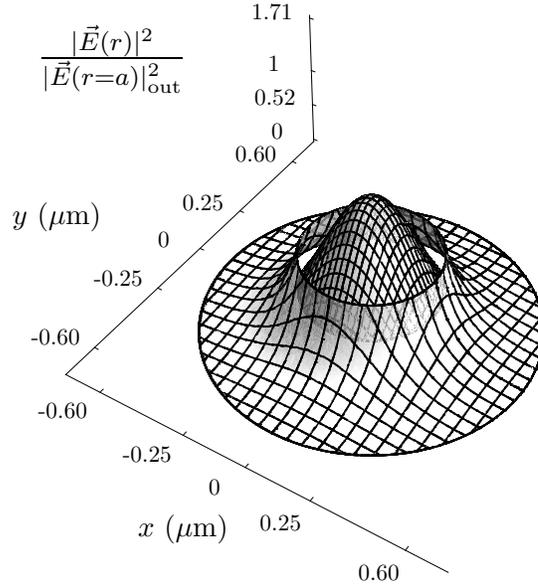
FIGURE 1.15: $|\vec{E}(r)|^2$ normalised to $|\vec{E}(r=a)|^2_{\text{out}}$ plotted as a function of x and y. The ticks in the vertical axis correspond to $|\vec{E}(r=\infty)|^2_{\text{out}} = 0$, $|\vec{E}(r=a)|^2_{\text{in}}/|\vec{E}(r=a)|^2_{\text{out}} = 0.52$, $|\vec{E}(r=a)|^2_{\text{out}}/|\vec{E}(r=a)|^2_{\text{out}} = 1$ and $|\vec{E}(r=0)|^2_{\text{in}}/|\vec{E}(r=a)|^2_{\text{out}} = 1.71$. The same parameters as in Fig. 1.11 have been assumed.

$\left|\vec{E}(r=a)\right|^2_{\text{in}}$. The fibre surface is indicated by the dashed vertical line. The decay length of the evanescent field outside the fibre given by $\Lambda_{11} = 1/q_{11}$ equals 244 nm for the considered parameters. Furthermore, for fixed values of n_1 and n_2, the decay length scales as λ/a. This wavelength dependence of the decay length is the basis of the experiment presented in Chap. 5.

Poynting vector

The Poynting vector quantifies the energy flux of the electromagnetic field. In the case of propagation in optical fibres, the average energy flux transmitted through the fibre is given by the z-component of the cycle-averaged Poynting vector [45]

$$\langle \vec{S} \rangle = \frac{1}{2} \text{Re} \left[\vec{E} \times \vec{H}^* \right]. \tag{1.21}$$

The fraction of power propagating inside and outside the fibre is given by

$$
\begin{aligned}
P_{\text{in}} &= \int_0^{2\pi} d\phi \int_0^a \langle S_z \rangle_{\text{in}} r \, dr, \\
P_{\text{out}} &= \int_0^{2\pi} d\phi \int_a^\infty \langle S_z \rangle_{\text{out}} r \, dr.
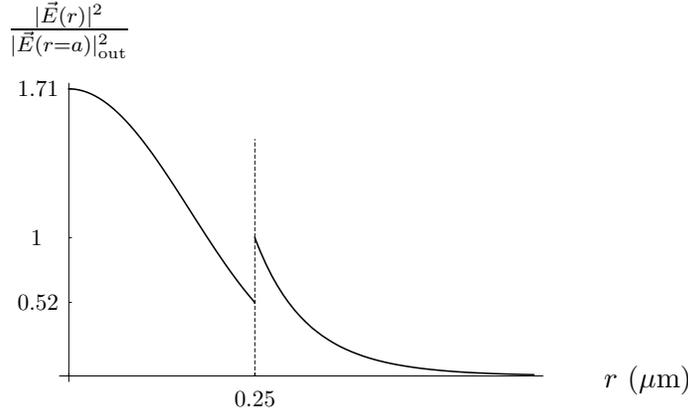\end{aligned}
\tag{1.22}
$$

FIGURE 1.16: $|\vec{E}(r)|^2$ normalised to $|\vec{E}(r = a)|^2_{\text{out}}$ plotted as a function of r. The same parameters as in Fig. 1.11 have been assumed.

The total power is then given by $P = P_{\text{in}} + P_{\text{out}}$. In order to find the Poynting vector of the electromagnetic field in the HE$_{11}$ mode, the equations of the magnetic field $\vec{H}$ are needed. Those can be easily calculated using Eqns. (A.25) and (A.27) and will not be explicitly given here. Using the mentioned relations together with Eqns. (1.16), (1.17), and (1.22) a relation between the total transmitted power P and the normalisation constant A can be obtained:

$$A = \sqrt{\frac{4\mu_0 \omega P}{\pi a^2 \beta_{11}}} \Big(D_{\text{in}} + D_{\text{out}} \Big)^{-1/2}, \tag{1.23}$$

with

$$D_{\text{in}} = \Big[(1 - s_{11})(1 + (1 - s_{11})\frac{\beta_{11}^2}{h_{11}^2})(J_0^2(h_{11}a) + J_1^2(h_{11}a)) +$$

$$+ (1 + s_{11})(1 + (1 + s_{11})\frac{\beta_{11}^2}{h_{11}^2})(J_2^2(h_{11}a) - J_1(h_{11}a)J_3(h_{11}a)) \Big], \tag{1.24}$$

$$D_{\text{out}} = \frac{J_1^2(h_{11}a)}{K_1^2(q_{11}a)} \Big[(1 - s_{11})(1 - (1 - s_{11})\frac{\beta_{11}^2}{q_{11}^2})(K_0^2(q_{11}a) - K_1^2(q_{11}a)) +$$

$$+ (1 + s_{11})(1 - (1 + s_{11})\frac{\beta_{11}^2}{q_{11}^2})(K_2^2(q_{11}a) - K_1(q_{11}a)K_3(q_{11}a)) \Big]. \tag{1.25}$$

Note that the fraction of power propagating outside the fibre is then given by $D_{\text{out}}/(D_{\text{in}}+ D_{\text{out}})$.

Figure 1.17 shows the z-component of the cycle-averaged Poynting vector $\langle S_z \rangle$ versus the radial position r. The surface of the fibre is indicated by the two dashed lines. As expected, the radial distribution of the transmitted power has a gaussian-like shape similar to $|\vec{E}(r)|^2$. The vectors shown at the position of the fibre surface correspond to $\langle S_z \rangle_{\text{out}}$ evaluated at $r = a$.
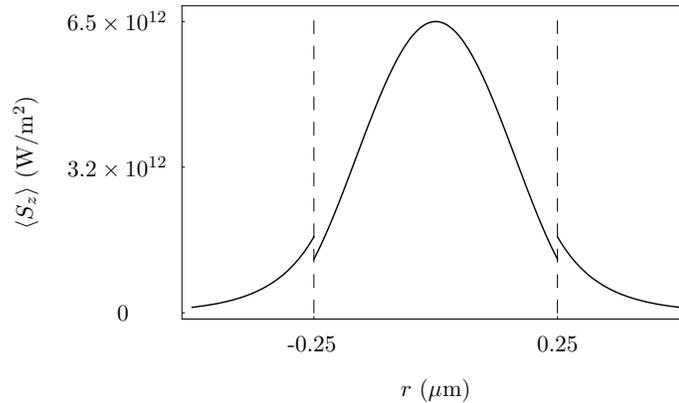
FIGURE 1.17: z-component of the cycle-averaged Poynting vector as a function of the radial position r for a power of $P = 1$ W. The same parameters as in Fig. 1.11 have been assumed.

The two components of the averaged Poynting vector $\langle \vec{S} \rangle$ transversal to the fibre axis, $\langle S_\phi \rangle$ and $\langle S_r \rangle$ account for the fraction of the energy flux of the electromagnetic field that does not propagate. These two magnitudes give some insight into the process of total internal reflection that radially confines the light in such an ultra-thin fibre. Figures 1.18 show the only non-vanishing component of the cycle-averaged Poynting vector transversal to the fibre axis, $\langle S_\phi \rangle$, for σ^+ (left) and σ^- (right) polarisation, respectively, assuming the same parameters as in Fig. 1.11. The non-vanishing azimuthal component of the Poynting vector indicates that the light circulates around the fibre axis during the propagation. This is in accordance with the geometric optics interpretation of the hybrid modes given in Sec. 1.1 where the *skew rays* spiral around the fibre axis. Furthermore, it has been calculated that the HE_{11} mode may have a total orbital angular momentum of $m\hbar$ per photon with $m = 0, 1, 2$, i.e., the total orbital angular momentum is a superposition of the quantum numbers 0, 1 and 2 [46]. Figs. 1.18 also show that the orbital angular momentum is indeed coupled to the polarisation, i.e., to the spin. This gives some insight into the adiabatic compressing of the light field taking place at the tapering transition of the tapered fibres described in Sec. 1.3. When coupling light into an ultra-thin optical fibre, the light field is not only focused, but also the spin and the orbital angular momentum couple to each other, leading to an angular momentum transfer from the spin to the orbital angular momentum.[1]

---

[1]The LP modes describe in good approximation the propagation of light in standard telecommunication optical fibres. These modes have a very small E_z component thereby leading to small S_ϕ. When transferring the light field from a non-tapered standard optical fibre to an ultra-thin optical fibre the above mentioned angular momentum coupling takes place.
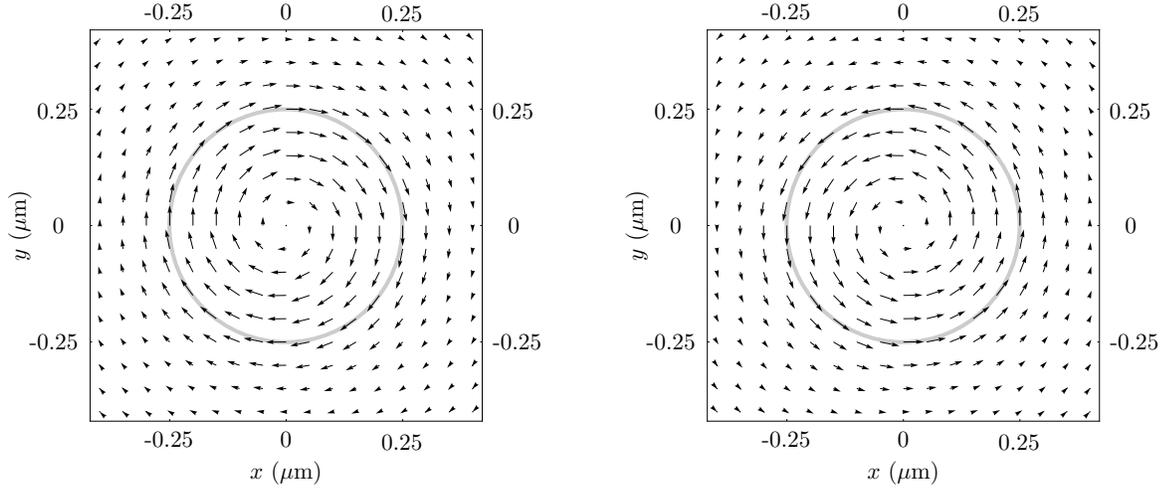
FIGURE 1.18: Vector plot of the only non-vanishing transversal component of the cycle-averaged Poynting vector $\langle S_\phi \rangle$ for σ^+ (left) and σ^- (right). The same parameters as in Fig. 1.11 have been used.

1.2.2   The fundamental HE$_{11}$ mode: Quasi-linear polarisation

I now present the field equations of the fundamental HE$_{11}$ mode with quasi-linear polarisation. From Eqns. (A.24) and (A.26) in Appendix A, the solutions of the linearly polarised fields can be obtained.

For $r < a$:

$$
E_x(r, \phi, z, t) = A_{\text{lin}} \frac{\beta_{11}}{2h_{11}} [(1 - s_{11}) J_0(h_{11}r) \cos(\varphi_0) -
$$
$$
- (1 + s_{11}) J_2(h_{11}r) \cos(2\phi - \varphi_0)] \exp[i(\omega t - \beta_{11}z)],
$$
$$
E_y(r, \phi, z, t) = A_{\text{lin}} \frac{\beta_{11}}{2h_{11}} [(1 - s_{11}) J_0(h_{11}r) \sin(\varphi_0) -
$$
$$
- (1 + s_{11}) J_2(h_{11}r) \sin(2\phi - \varphi_0)] \exp[i(\omega t - \beta_{11}z)],
$$
$$
E_z(r, \phi, z, t) = iA_{\text{lin}} J_1(h_{11}r) \cos(\phi - \varphi_0) \exp[i(\omega t - \beta_{11}z)]. \tag{1.26}
$$

For $r > a$:

$$
E_x(r, \phi, z, t) = A_{\text{lin}} \frac{\beta_{11}}{2q_{11}} \frac{J_1(h_{11}a)}{K_1(q_{11}a)} [(1 - s_{11}) K_0(q_{11}r) \cos(\varphi_0) +
$$
$$
+ (1 + s_{11}) K_2(q_{11}r) \cos(2\phi - \varphi_0)] \exp[i(\omega t - \beta_{11}z)],
$$
$$
E_y(r, \phi, z, t) = A_{\text{lin}} \frac{\beta_{11}}{2q_{11}} \frac{J_1(h_{11}a)}{K_1(q_{11}a)} [(1 - s_{11}) K_0(q_{11}r) \sin(\varphi_0) +
$$
$$
+ (1 + s_{11}) K_2(q_{11}r) \sin(2\phi - \varphi_0)] \exp[i(\omega t - \beta_{11}z)],
$$
$$
E_z(r, \phi, z, t) = iA_{\text{lin}} \frac{J_1(h_{11}a)}{K_1(q_{11}a)} K_1(q_{11}r) \cos(\phi - \varphi_0) \exp[i(\omega t - \beta_{11}z)], \tag{1.27}
$$

where q_{11}, h_{11} and s_{11} have been defined in Sec. 1.2.1. The angle φ_0 accounts for the polarisation direction, $\varphi_0 = 0$ leading to x-polarisation of the transverse $\vec{E}$ field and $\varphi_0 = \pi/2$ to y-polarisation. The normalisation constant A_{lin} is related to the maximum amplitude of the electric field and satisfies the relation $A_{\text{lin}} = \sqrt{2}A$, where A is the global constant of the fields with rotating polarisation given in Sec. 1.2.1. Using Eq. (1.23), the relation between A_{lin} and the total power transmitted through the fibre can be obtained.
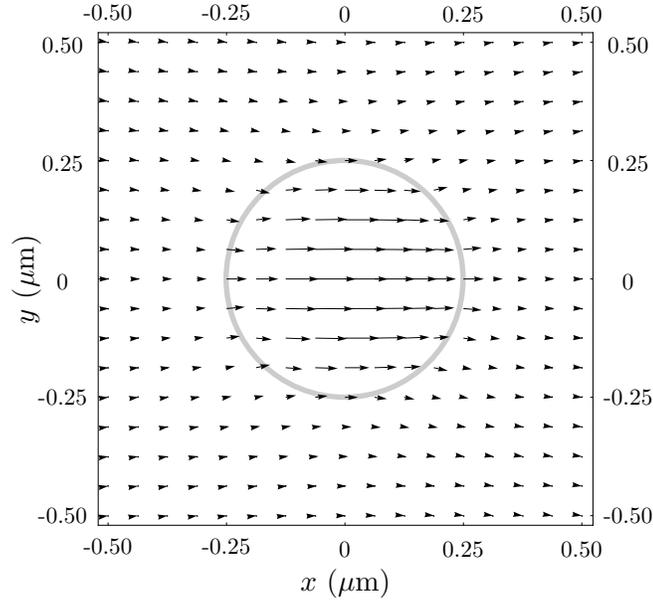
FIGURE 1.19: Field plot of the electric field component perpendicular to the fibre axis $\vec{E}_\perp$ in the HE$_{11}$ mode with x-polarisation ($\varphi_0 = 0$) at $t = 0$ and $z = 0$. The following parameters have been assumed: $n_1 = 1.452$, $n_2 = 1$, $a = 250$ nm and $\lambda = 852$ nm.

Figure 1.19 shows the vector plot of the electric field component transversal to the fibre axis $\vec{E}_\perp$ at $z = 0$ and $t = 0$. The fibre surface is indicated by a grey circle. The calculations have been performed for a fibre of pure silica ($n_1 = 1.452$), with a radius of $a = 250$ nm, surrounded by vacuum ($n_2 = 1$), a field wavelength of $\lambda = 852$ nm and a polarisation direction given by $\varphi_0 = 0$. The polarisation direction of $\vec{E}_\perp$ is not time dependent but it does depend on the position. The largest deviations from a perfect x-polarisation take place in the evanescent field at the surface of the fibre.

The absolute value of the squared electric field averaged over one oscillation period $\left|\vec{E}(r)\right|^2$ in the HE$_{11}$ mode is given by

$$\left|\vec{E}(r,\phi)\right|^2_{\text{in}} = \frac{A_{\text{lin}}^2 \beta_{11}^2}{4 h_{11}^2} \Big[(1 - s_{11})^2 J_0^2(h_{11}r) + (1 + s_{11})^2 J_2^2(h_{11}r) + 2\frac{h_{11}^2}{\beta_{11}^2} J_1^2(h_{11}r) +$$

$$+ 2\Big(\frac{h_{11}^2}{\beta_{11}^2} J_1^2(h_{11}r) - (1 + s_{11})(1 - s_{11}) J_0(h_{11}r) J_2(h_{11}r)\Big) \cos[2(\phi - \varphi_0)]\Big],$$

$$(1.28)$$

$$\left|\vec{E}(r,\phi)\right|^2_{\text{out}} = \frac{A^2_{\text{lin}}\beta^2_{11}}{4q^2_{11}}\frac{J^2_1(h_{11}a)}{K^2_1(q_{11}a)}\Big[(1-s_{11})^2K^2_0(q_{11}r) + (1+s_{11})^2K^2_2(q_{11}r) + 2\frac{q^2_{11}}{\beta^2_{11}}K^2_1(q_{11}r)+$$

$$+ 2\Big(\frac{q^2_{11}}{\beta^2_{11}}K^2_1(q_{11}r) + (1+s_{11})(1-s_{11})K_0(q_{11}r)K_2(q_{11}r)\Big)\cos[2(\phi-\varphi_0)]\Big],$$

$$(1.29)$$

where $|\vec{E}(r)|^2_{\text{in}}$ ($|\vec{E}(r)|^2_{\text{out}}$) denotes the time-averaged squared electric field inside (outside) the fibre. Similarly to the case of rotating polarisation, the equations above can be used to estimate the strength of E_z, leading to $|E_z(r=a,\phi=0)|^2_{\text{in}}/|\vec{E}(r=a,\phi=0)|^2_{\text{in}} = 0.6$ and to $|E_z(r=a,\phi=0)|^2_{\text{out}}/|\vec{E}(r=a,\phi=0)|^2_{\text{out}} = 0.25$ at the fibre surface [37]. Note that E_z vanishes where $\vec{E}_\perp$ is parallel to the fibre surface and reaches its maximum value where $\vec{E}_\perp$ is perpendicular to it. This is in accordance with the ray optics interpretation given in Sec. 1.1.
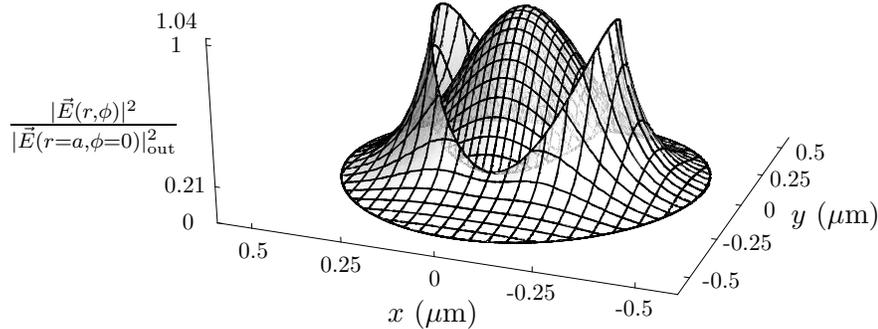
FIGURE 1.20: $|\vec{E}(r,\phi)|^2$ normalised to $|\vec{E}(r=a,\phi=0)|^2_{\text{out}}$ plotted against x and y. The ticks in the vertical axis correspond to $|\vec{E}(r=a,\phi=\pi/2)|^2_{\text{in}}/|\vec{E}(r=a,\phi=0)|^2_{\text{out}} = 0.21$, $|\vec{E}(r=a,\phi=0)|^2_{\text{out}}/|\vec{E}(r=a,\phi=0)|^2_{\text{out}} = 1$ and $|\vec{E}(r=0)|^2_{\text{in}}/|\vec{E}(r=a,\phi=0)|^2_{\text{out}} = 1.04$. The same fibre-field parameters as in Fig. 1.19 have been assumed.

Figure 1.20 shows the distribution of $\left|\vec{E}(r,\phi)\right|^2_{\text{in}}$ (inside) and $\left|\vec{E}(r,\phi)\right|^2_{\text{out}}$ (outside) normalised to the value $\left|\vec{E}(r=a,\phi=0)\right|^2_{\text{out}}$ (surface) as a function of x and y. The regions where $r < a$ and $r > a$ can be clearly identified due to the discontinuity at the boundary $r = a$. The term $\cos[2(\phi-\varphi_0)]$ in Eqns. (1.28) and (1.29) breaks the cylindrical symmetry of the system producing a much larger evanescent field in the regions where the component $\vec{E}_\perp$ is transversal to the fibre surface. This becomes apparent in Fig. 1.21. The evanescent field is maximal at $\phi = 0$ (right) and minimal at $\phi = \pi/2$ (left). The

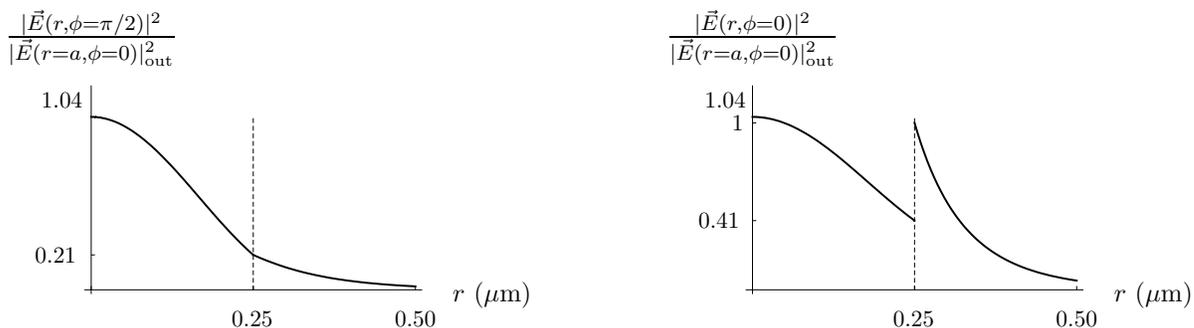fibre surface is indicated by a dashed vertical line.

FIGURE 1.21: $\vec{E}(r,\phi)|^2$ normalised to $|\vec{E}(r=a,\phi=0)|^2_{\text{out}}$ plotted as a function of r at $\phi=\pi/2$ (left) and $\phi=0$ (right) for the same fibre-field parameters as in Fig. 1.19.

The decay length of the evanescent field given by $\Lambda_{11}=1/q_{11}$ is polarisation independent and, hence, takes the same value as for the case of rotating polarisation, i. e., 244 nm for the considered parameters.

1.2.3 Evanescent field strength in the HE$_{11}$ mode: Quasi-linear polarisation

The distribution of the cycle-averaged squared electric field $|\vec{E}|^2$ in the HE$_{11}$ mode with a fibre radius of $a=0.29\lambda$ and quasi-linear polarisation is given by Eqns. (1.28) and (1.29). Under such conditions, the effective mode diameter is of the order of the wavelength λ and a large fraction of the power is guided outside the fibre. In general, for silica fibres surrounded by vacuum or by air, the ratio between the radius and the wavelength necessary in order to have a significant evanescent field is $a/\lambda < 1/2$. A meaningful minimisation of the mean field diameter in such ultra-thin optical fibres can be found in [36]. Here, a similar treatment will be carried out. The wavelength of the light and the refractive indices are fixed at the values $\lambda = 852$ nm, $n_1 = 1.452$ and $n_2 = 1$. The radius of the fibre a is varied to maximise the value of $|\vec{E}|^2_{\text{out}}$ at the fibre surface. The conclusions of this treatment are also valid for circular polarisation.

Figure 1.22 shows the variation of $|\vec{E}(x=a,y=0)|^2_{\text{out}}$ normalised to its optimum value at $a=0.23\lambda$ as a function of a/λ. The calculations have been performed assuming the x-polarised electric field given by Eqns. (1.27). Note that the magnitude $|\vec{E}|^2_{\text{out}}$ is evaluated at $(x,y)=(a,0)$, where the polarisation of the $\vec{E}$ field is perpendicular to the fibre surface and the evanescent field is thus optimal. The maximum of the curve shown in Fig. 1.22 corresponds to a fibre radius of $a=196$ nm. The evolution of $|\vec{E}|^2_{\text{out}}$ at the fibre surface while varying the fibre radius can be understood with help of Figs. 1.23–1.30, where the cycle-averaged squared electric field normalised to its maximum value at the fibre surface $|\vec{E}(x=a,y=0)|^2_{\text{out},a=0.23\lambda}$ is plotted against the x-coordinate normalised to the wavelength λ. The fibre surface is indicated by the two vertical solid lines. For
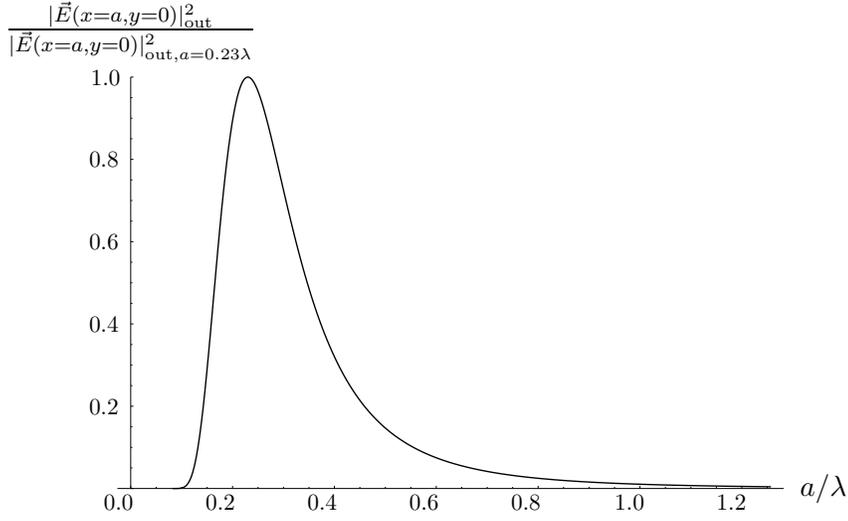
$$\frac{|\vec{E}(x=a,y=0)|^2_{\text{out}}}{|\vec{E}(x=a,y=0)|^2_{\text{out},a=0.23\lambda}}$$

FIGURE 1.22: Distribution of $|\vec{E}(x = a, y = 0)|^2_{\text{out}}$ normalised to its optimum value at a radius $a = 0.23\lambda$ as a function of the ratio a/λ assuming x-polarisation of the transverse field (see Eqns. (1.27)).

large values of the fibre radius a (Fig. 1.23) the field is mostly guided inside the fibre and the evanescent field is small. As the fibre radius is reduced, the evanescent field at the fibre surface $|\vec{E}(x = a, y = 0)|^2_{\text{out}}$ increases reaching its maximum at $a = 0.23\lambda$ (Fig. 1.28). Note that this is the maximum value of $|\vec{E}(x, y)|^2$ for any fibre radius at any point (x, y). If the fibre radius is further reduced, the fibre will not be capable anymore to radially confine the electric field, leading to a drastic increase of the mode diameter that transforms $\vec{E}$ into a plane wave for vanishing radius (Fig. 1.30).

The knowledge of the evanescent field strength at the vicinity of the fibre surface is of great relevance in quantum optics experiments where dipole emitters are coupled to the evanescent field of the fibre. The parameters used above correspond to the experimental work described in this thesis: Caesium atoms interacting with the evanescent field of an ultra-thin optical fibre tuned at the resonant wavelength of the D_2-line at 852 nm. The optimal radius is 196 nm for this wavelength. However, when choosing the appropriate experimental fibre radius certain experimental limitations must be taken into account, e. g., the total transmission through the fibre or its mechanical properties [36].

1.2.4   The TE$_{01}$ mode

I now present the electric field equations of the first higher-order mode, TE$_{01}$.
For $r < a$:

$$\begin{aligned}
E_\phi(r, \phi, z, t) &= \frac{\omega\mu_0}{h_{01}} B J_1(h_{01}r) \exp[i(\omega t - \beta_{01}z)], \\
E_z(r, \phi, z, t) &= E_r(r, \phi, z, t) = 0.
\end{aligned} \qquad (1.30)$$

$$\frac{|\vec{E}(x,y=0)|^2_{\text{out}}}{|\vec{E}(x=a,y=0)|^2_{\text{out},a=0.23\lambda}}$$

FIGURE 1.23: $a/\lambda = 0.48$

FIGURE 1.24: $a/\lambda = 0.43$

FIGURE 1.25: $a/\lambda = 0.38$

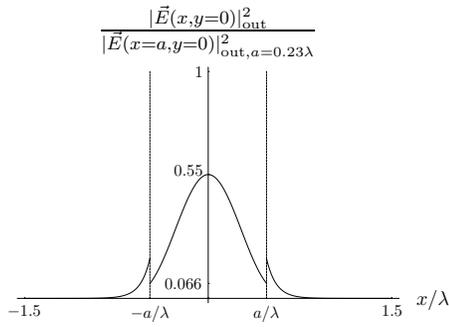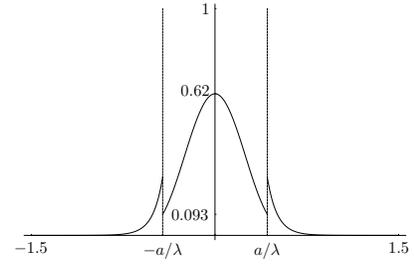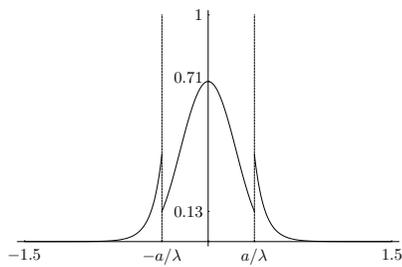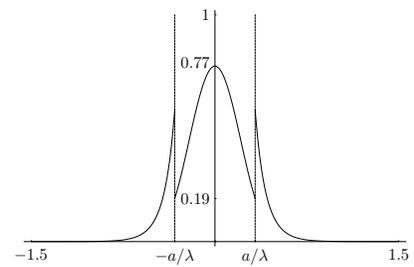FIGURE 1.26: $a/\lambda = 0.33$
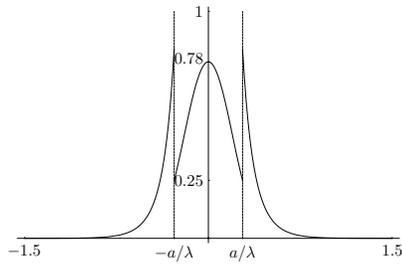
FIGURE 1.27: $a/\lambda = 0.28$
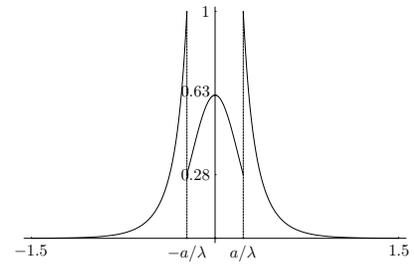
FIGURE 1.28: $a/\lambda = 0.23$
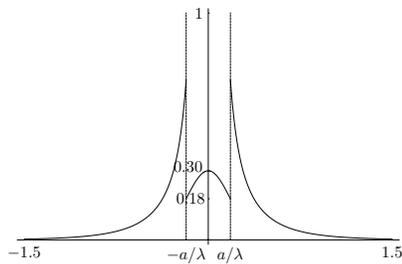
FIGURE 1.29: $a/\lambda = 0.18$
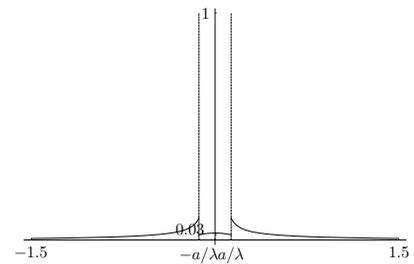
FIGURE 1.30: $a/\lambda = 0.13$

Variation of the magnitude $|\vec{E}(x,y=0)|^2_{\text{out}}$ normalised to its maximum value at $a = 0.23\lambda$ as a function of the x-coordinate for x-polarised light and normalised to the wavelength λ for several fibre radii.

For $r > a$:

$$
\begin{aligned}
E_\phi(r, \phi, z, t) &= -\frac{\omega\mu_0}{q_{01}} \frac{J_0(h_{01}a)}{K_0(q_{01}a)} B K_1(q_{01}r) \exp[i(\omega t - \beta_{01}z)], \\
E_z(r, \phi, z, t) &= E_r(r, \phi, z, t) = 0,
\end{aligned}
\tag{1.31}
$$

where,

$$
\begin{aligned}
h_{01} &= \sqrt{k_0^2 n_1^2 - \beta_{01}^2}, \\
q_{01} &= \sqrt{\beta_{01}^2 - k_0^2 n_2^2}.
\end{aligned}
\tag{1.32}
$$

β_{01} denotes propagation constant of the TE_{01} mode given by Eq. (1.8) and B the normalisation constant of the electric field which can be determined using Eq. (1.35) below.

Figure 1.31 shows the vectorial plot of the only non-vanishing electric field component E_ϕ at $z = 0$ and $t = 0$ as a function of the coordinates x and y. The fibre surface is indicated by a grey circle. The calculations have been performed for a fibre of pure silica ($n_1 = 1.452$), with a radius of $a = 400$ nm, surrounded by vacuum ($n_2 = 1$), and a field wavelength of $\lambda = 852$ nm corresponding to a V parameter of 3.11. Since
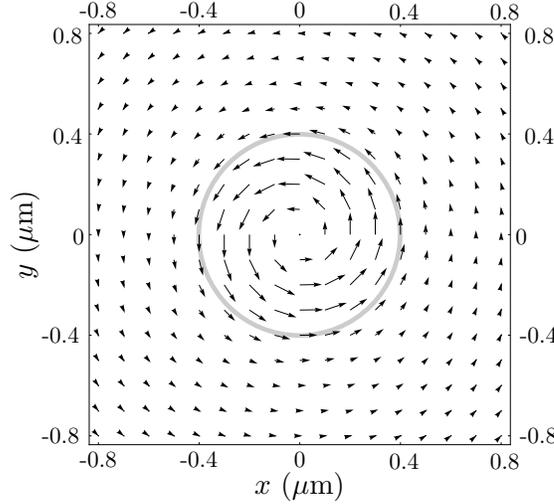
FIGURE 1.31: Field plot of the electric field in the TE_{01} mode at $t = 0$ and $z = 0$ for the following parameters: $n_1 = 1.452$, $n_2 = 1$, $a = 400$ nm and $\lambda = 852$ nm.

the polarisation in the TE_{01} mode is always parallel to the fibre surface, there is no discontinuity of the electric field at the boundary. Furthermore, in accordance with the ray optics picture given in Sec. 1.1, the TE_{01} mode has no z-component of the electric field.

The squared $\vec{E}$ field averaged over one oscillation period inside and outside the fibre is given by

$$
\left.\left|\vec{E}(r)\right|\right.^2_{\text{in}} = \frac{B^2}{2} \left(\frac{\omega\mu_0}{h_{01}}\right)^2 J_1^2(h_{01}r),
\tag{1.33}
$$

$$\left|\vec{E}(r)\right|^2_{\text{out}} = \frac{B^2}{2}\left(\frac{\omega\mu_0}{q_{01}}\right)^2 \frac{J_0^2(h_{01}a)}{K_0^2(q_{01}a)} K_1^2(q_{01}r). \tag{1.34}$$

Figure 1.32 shows the distribution of $\left|\vec{E}(r)\right|^2_{\text{in}}$ (inside) and $\left|\vec{E}(r)\right|^2_{\text{out}}$ (outside) normalised to its value at the surface $\left|\vec{E}(r=a)\right|^2$ as a function of x and y. The boundary at $r=a$ is indicated by a black circle. The maximum and the minimum of $\left|\vec{E}(r)\right|^2$ are located inside the fibre at $r=0.268$ μm and $r=0$, respectively.
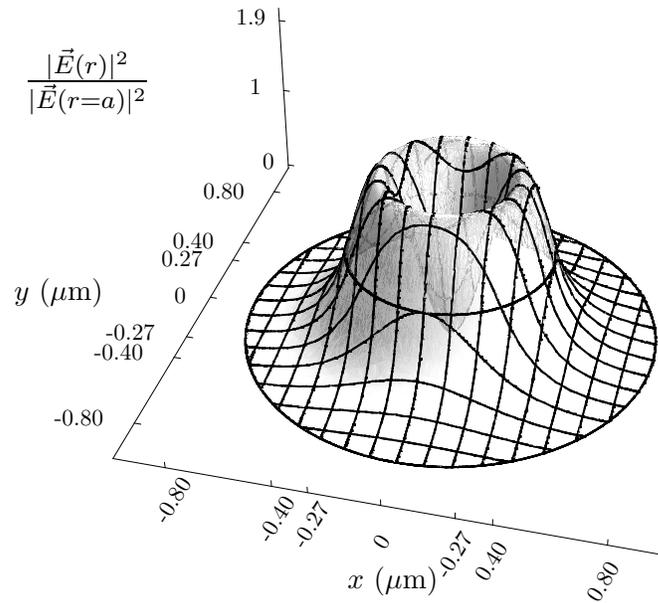
FIGURE 1.32: Variation of $|\vec{E}(r)|^2$ normalised to $|\vec{E}(r=a)|^2$ as a function of x and y. The ticks in the vertical axis correspond to $|\vec{E}(r=0)|^2_{\text{in}} = 0$, $|\vec{E}(r=a)|^2/|\vec{E}(r=a)|^2 = 1$ and $|\vec{E}(r=0.67a)|^2_{\text{in}}/|\vec{E}(r=a)|^2 = 1.9$. The same parameters as in Fig. 1.31 have been assumed.

The value of $\left|\vec{E}(r=0)\right|^2$ can be better appreciated in Fig. 1.33. Here, the variation of $\left|\vec{E}(r)\right|^2$ normalised to its value at the surface $\left|\vec{E}(r=a)\right|^2$ is shown as a function of r. The fibre surface is indicated by a dashed vertical line. $\left|\vec{E}(r=a)\right|^2$ is about 53% of the maximum value $\left|\vec{E}(r=0.67a)\right|^2_{\text{in}}$, and, as mentioned above, $\left|\vec{E}(r=a)\right|^2_{\text{in}} = \left|\vec{E}(r=a)\right|^2_{\text{out}}$. The decay length of the evanescent field given by $\Lambda_{01} = 1/q_{01}$ equals 280 nm for the considered parameters.

Normalisation

Using Eqns. (1.21) and (1.22) the following relation between the normalisation constant B and the total power P can be obtained:

$$\frac{|\vec{E}(r)|^2}{|\vec{E}(r=a)|^2_{\text{out}}}$$
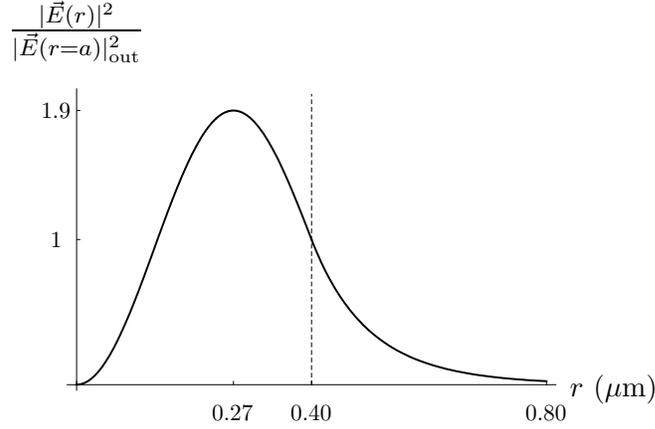
FIGURE 1.33: Variation of $|\vec{E}(r)|^2$ normalised to $|\vec{E}(r=a)|^2$ as a function of r for the same parameters as in Fig. 1.31.

$$B = \sqrt{\frac{2P}{\pi a^2 \beta_{01} \mu_0 \omega}} \Big(D_{01,\text{ in}} + D_{01,\text{ out}}\Big)^{-1/2}, \tag{1.35}$$

$$D_{01,\text{ in}} = \frac{1}{h_{01}^2}(J_1^2(h_{01}a) - J_0(h_{01}a)J_2(h_{01}a)),$$

$$D_{01,\text{ out}} = \frac{1}{q_{01}^2}\frac{J_0^2(h_{01}a)}{K_0^2(q_{01}a)}(K_0(q_{01}a)K_2(q_{01}a) - K_1^2(q_{01}a)).$$

$$\tag{1.36}$$

Note that the fraction of power propagating outside the fibre is then given by $D_{01,\text{ out}}/(D_{01,\text{ in}} + D_{01,\text{ out}})$.

The total power transmitted through the fibre P can be found by integrating the z-component of the cycle-averaged Poynting vector $\langle S_z \rangle$ in the xy-plane. Indeed, in accordance with the ray optics interpretation of the transverse modes given in Sec. 1.1, $\langle S_z \rangle$ is the only non-vanishing component of the cycle-averaged Poynting vector in the TE_{01} mode. The energy flow does not circulate around the fibre axis in those modes because the light rays follow meridional reflection paths inside the fibre during the propagation. Furthermore, since $\vec{E}$ and $\vec{H}$ are transversal, $\langle S_z \rangle \propto |\vec{E}(r)|^2$ like for free propagating beams.

1.3 Tapered optical fibres (TOF's)

The theoretical description of the fields propagating in optical fibres with a radius comparable to the wavelength of the guided light has been given in Sec. 1.2. In order to

reach such small fibre radii, standard optical fibres can be tapered using the procedure explained in Sec. 1.3.1 below.

Figure 1.34 shows the schematic of a tapered optical fibre (TOF) with three separated regions exhibiting different propagation properties.

(1)   (2)   (3)
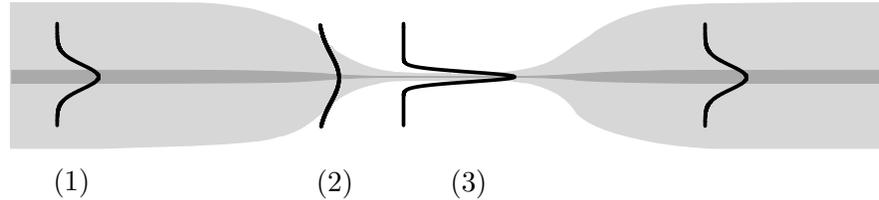
FIGURE 1.34: Schematic of the light propagation in a tapered optical fibre (TOF). The labels (1)-(3) denote the different propagation regions.

- (1) Unmodified single-mode optical fibre: The light is guided inside the core by means of total internal reflection at the boundary with the cladding. The mode diameter amounts to several micrometres. Approximative solutions of the Maxwell equations can be found in this region, leading to the LP modes [44].

- (2) Taper transition: Here, the fibre becomes thinner and so does the core. The light is radially compressed until the core becomes too thin to efficiently guide the field. At this point, the light is guided in three regions, the remaining core, the cladding, and the medium surrounding the cladding. Finally, the fibre radius further reduces down to the value at the waist thereby further compressing the light field. The influence of the core is then negligible and the light is guided at the interface between the cladding and the surrounding medium. Therefore, the cladding now plays the role of the core and the surrounding medium the role of the cladding. Ideally, this compression should be adiabatic, i. e., there should be no coupling between modes of different order and no coupling to radiating modes during the process. As shown in Sec. 1.3.2, when such uncontrolled mode excitations in the taper transition take place, the overall transmission of the fibre decreases. In order to obtain an adiabatic taper transition a well controlled radius profile of the transition is required.

- (3) Fibre waist: Here, the fibre radius remains constant at the sub-wavelength regime. The light propagating in the waist exhibits a strong radial confinement and a large evanescent field.

1.3.1   Flame-pulling of optical fibres

The tapering of optical fibres takes place in a computer controlled fibre pulling rig, which is extensively described in the Ph.D. thesis of F. Warken [36]. The fabrication

(a)

(b)
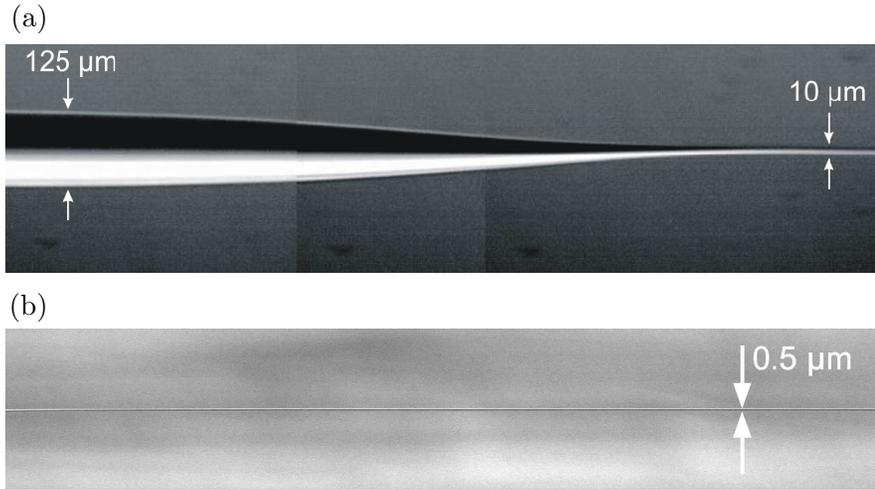
FIGURE 1.35: (a) Concatenation of several optical microscope pictures of a TOF. (b) REM (Reflection Electron Microscope) picture of the waist of a TOF. The diameter of the waist was measured to be 0.5 μm.

procedure of the fibres can be briefly described as follows: The fibre is heated with a hydrogen-oxygen flame and elongated by pulling on both ends. The elongation of the heated part, leads to a reduction of the fibre diameter in this region. At the realised temperature, the fibre becomes soft but does not yet melt [36], permitting a controlled tapering of the fibre. The pulling is carried out using two computer governed translation stages [47] that allow sub-micrometre actuation of the positioning. The profile of the taper transition is an important issue in the quality of a tapered fibre in order to avoid losses and undesired mode-coupling in the transmission of light through the fibre. For that, the translation stages also move the fibre with respect to the flame. Thereby, a broad assortment of profiles can be realised. The taper profile as well as the final diameter of the waist is previously simulated using a computer program. From this simulations, the trajectories to be followed by the translation stages are determined and, in the last stage of the production, executed in synchronisation with the gas flame. This fibre pulling rig produces fibres with diameters ranging from several micrometres to 100 nanometres. As an example, Figs. 1.35 (a) and (b) show the taper transition and the waist of a standard optical fibre with a waist diameter of 500 nm, respectively. For a better visualisation Fig. (a) shows a very steep profile because the slope of an optimal taper transition is otherwise too shallow to be recognisable. Figure 1.35 (b) is a REM picture of the fibre waist with a measured diameter of 0.5 μm.

1.3.2 Measurement of the transmission

The transmission through the fibre can be continuously monitored during the pulling process, thereby giving valuable information not only about the quality of the taper but also about the processes that introduce losses in the overall transmission.

FIGURE 1.36: Transmission through a single-mode optical fibre during the pulling process normalised to the transmission of the unprocessed fibre. The measurements were done using a 852 nm diode laser and a non-polarisation maintaining fibre.

Figure 1.36 shows the monitored transmission through a single-mode fibre during the pulling process normalised to the transmission of the unprocessed fibre. The targeted fibre diameter is 500 nm 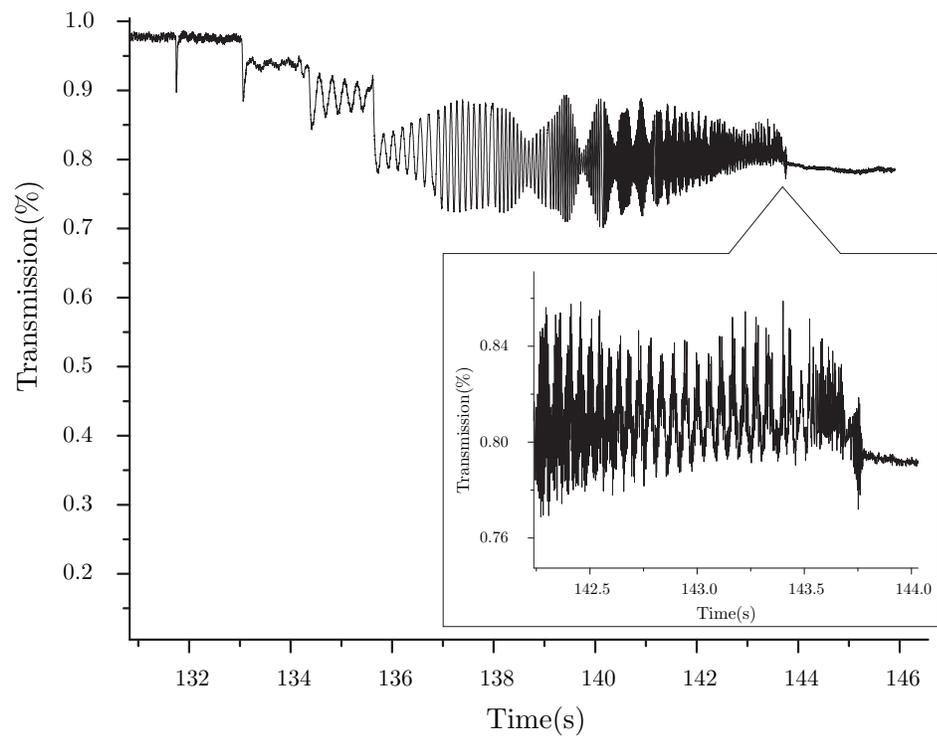at the waist. The overall transmission at the end of the pulling process is 79%, however, fibres of similar diameter with transmission up to 97% have been produced. Although the pulling process required 146 seconds the most significant effects took place during the last 15 seconds. The oscillatory behavior of the transmission can be explained as an interferometric process between different modes guided through the waist [48]: The oscillations of the transmission begin when the core diameter in the waist is too small to guide the light. Therefore, the fields expand and reach the cladding and the surrounding medium. At this fibre diameter the waist does not fulfill the single-mode condition, i.e., few higher-order modes in addition to the fundamental mode can propagate. The amount of power carried by each of them critically depends on the taper transition connecting the unprocessed single-mode region of the fibre to the multi-mode waist. At the end of the waist, the core recovers its original size and the fibre is single-mode again. Here, the power carried by the higher-order modes that propagate in the waist couples back either to the fundamental mode or to free-space modes outside the fibre. This fraction of power that couples into the fundamental mode is determined by the relative phase between the modes in the waist, which varies during the elongation, leading to time-dependent oscillations of the transmission. The oscillations vanish when the fibre waist diameter reaches the single-mode regime. At this point, the losses due to excitation of higher-order modes are fixed and only depend on the taper transition profile. Intuitively, the fibres with the best transmission are those that exhibit minimal oscillations during the pulling process. This is an indication of adiabatic compression of the light field in the taper region that minimises the losses [49].

1.3.3   Measurement of the local diameter and the surface quality of a TOF

Other important factors that also determine the quality of an ultra-thin optical fibre are the diameter of and the surface smoothness at the waist. Figure 1.37 shows a TEM picture of the waist of a TOF. The targeted waist diameter was 500 nm. The measurement yields a diameter of 483 nm with an estimated precision of ± 3 nm, i. e. a 96.6% agreement with the simulations.

A biasing of the simulations with respect to the experimental values for the case of fibre diameters smaller than 1 μm has been observed: The simulated diameters are between 5 and 10% larger than the measured values. This can be explained by the influence of the gas flow coming from the flame that pushes the fibre perpendicularly to the pulling direction, thereby further reducing its diameter.

Figure 1.38 shows a TEM picture of the surface at the waist of a TOF. Despite the focusing not being optimal, the surface rugosity can be estimated to be less than 5 nm. Furthermore, no indications of contamination on the surface can be observed. Since a large fraction of power in such ultra-thin optical fibres propagates in the evanescent
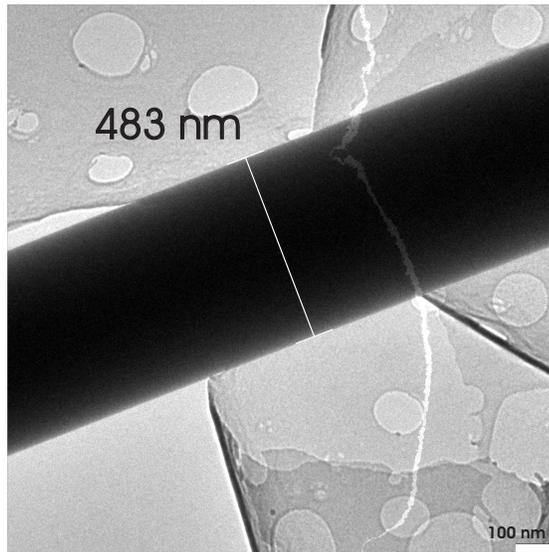
FIGURE 1.37: Transmission electron microscope (TEM) picture of the waist of a TOF with a diameter of 483 ± 3 nm. The patterns appearing in the picture are due to carbon foils placed on top of the fibre to fix it to the substrate.

field, surface contamination by deposition of dust particles, oil or grease in the waist leads to a strong decrease in the transmission.

The TEM pictures shown in Figs. 1.39 (a) and (b) reveal that the fibre was contaminated. The contamination probably took place when the fibre was deposited on a surface that had been in contact with oil. Other contamination mechanisms include diffusion of oil in a vacuum chamber coming from the vacuum pump or dust deposition in a normal atmosphere. In order to avoid them, the fibre pulling process must take place in a dust-free environment [36] and the oil-free vacuum technology is a prerequisite for experiments with tapered optical fibres [35].
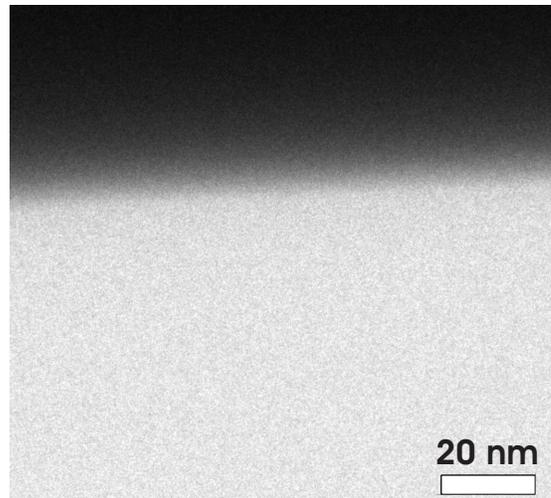
FIGURE 1.38: TEM picture of the surface (dark bulk) at the waist of a TOF.
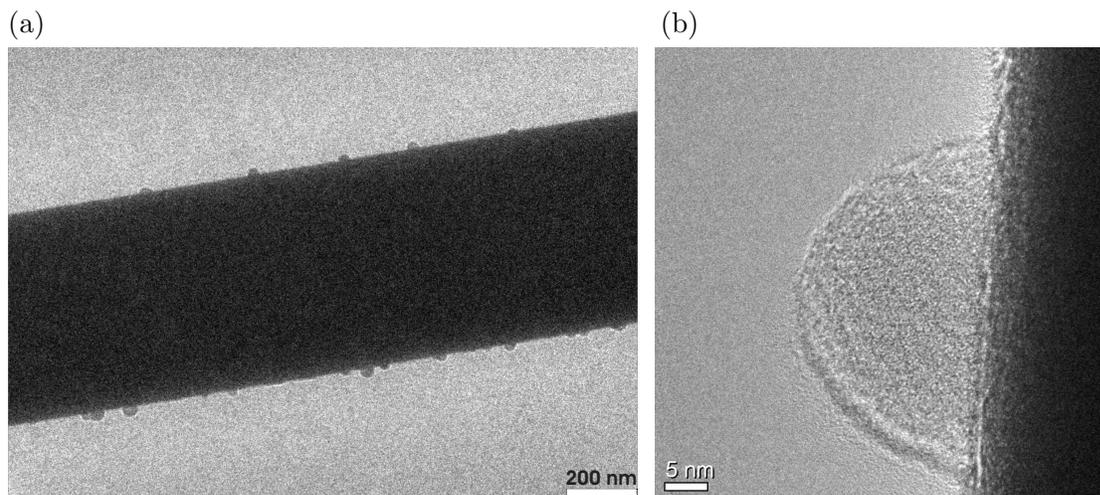
FIGURE 1.39: (a) TEM picture of the waist of a TOF that was contaminated. (b) TEM picture of the contaminated surface of a TOF. The contaminating substance was probably oil.

Chapter 2

Theory of the atom-field interaction

The necessary theoretical basis for the following Chaps. 3 - 5 is given here. In particular, approximations for the near-resonant and the far-detuned regimes of the atom-field interaction are deduced. This Chapter is organised as follows: In Sec. 2.1 the Lorenz's model for the classical atom-field interaction is explained. Section 2.2 is devoted to the near-resonant interaction, where the frequency of the external field is almost equal to the transition frequency of the atom. Finally, Sec. 2.3 is devoted to the case of far-detuned interaction, where the difference between the transition frequency of the atom and the frequency of the external field is comparable to the energy difference between the atomic levels.

2.1   Classical model of the atom-field interaction

I now derive the expressions of the scattering rate and the dipole force of an atom in a monochromatic light-field using the Lorenz model. Let us consider the atom as a single electron with charge -e and mass m_e elastically bound to the core with charge +e and mass $m_{\text{core}} \gg m_e$ by a harmonic potential. In the presence of a time-dependent external electric field $\vec{E}(t) = \vec{E}_0 e^{i\omega t}$ the system can be described by the equation of motion of a driven harmonic oscillator

$$\ddot{\vec{x}}(t) + \Gamma_\omega \dot{\vec{x}}(t) + \omega_0^2 \vec{x}(t) = -\frac{e}{m_e} \vec{E}(t), \tag{2.1}$$

where ω_0 is the resonance angular frequency of the oscillator and $\Gamma_\omega \dot{\vec{x}}(t)$ describes the damping of the electron motion. The dissipation rate due to classical dipole radiation is given by [50]

$$\Gamma_\omega = \frac{e^2 \omega^2}{6\pi\varepsilon_0 m_e c^3}. \tag{2.2}$$

The stationary solution of Eq. (2.1) is then

$$\vec{x}(t) = -\frac{\alpha(\omega)}{e}\vec{E}(t),$$ (2.3)

where

$$\alpha(\omega) = \frac{e^2}{m_e}\frac{1}{\omega_0^2 - \omega^2 - i\Gamma_\omega\omega}$$ (2.4)

is the polarisability of the atom. It is useful to express Eq. (2.3) using the induced dipole moment of the atom $\vec{d}(t) = -e\vec{x}(t) = \alpha(\omega)\vec{E}(t)$. Note that the polarisability $\alpha(\omega)$ has a real and a complex part which describe the in-phase and the quadrature components of the atomic dipole moment $\vec{d}$, respectively. Using the expression $e^2/m_e = 6\pi\varepsilon_0 c^3\Gamma_\omega/\omega^2$ and the damping rate on resonance $\Gamma = \Gamma_{\omega_0}$ the following relations are obtained

$$\text{Re}[\alpha(\omega)] = 6\pi\varepsilon_0 c^3\frac{(\omega_0^2 - \omega^2)\Gamma/\omega_0^2}{(\omega_0^2 - \omega^2)^2 + \Gamma^2(\omega^3/\omega_0^2)^2},$$ (2.5)

$$\text{Im}[\alpha(\omega)] = 6\pi\varepsilon_0 c^3\frac{\Gamma^2\omega^3/\omega_0^4}{(\omega_0^2 - \omega^2)^2 + \Gamma^2(\omega^3/\omega_0^2)^2}.$$ (2.6)
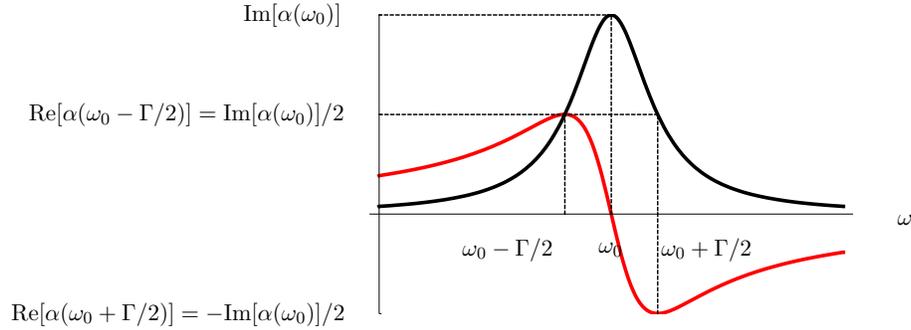
FIGURE 2.1: Real (red) and complex (black) parts of the polarisability $\alpha(\omega)$ in the Lorenz model.

Figure 2.1 shows the real (red) and complex (black) parts of the polarisability α as a function of the frequency of the external field ω. Note that $\text{Im}[\alpha] > \text{Re}[\alpha]$ near the resonance, i. e., for $\omega \sim \omega_0$, but otherwise $\text{Im}[\alpha] < \text{Re}[\alpha]$.

2.1.1   Scattering rate

In analogy to the driven harmonic oscillator, the average power dissipated by the atom is given by

$$P = \left\langle \text{Re}[\dot{\vec{d}}(t) \cdot \vec{E}(t)] \right\rangle = \frac{\omega|E_0|^2}{2}\text{Im}[\alpha(\omega)].$$ (2.7)

Thus, the quadrature part of the polarisability describes the absorptive interaction of the atom with the field, i. e., the atom dissipates energy from the external field by absorbing and subsequently radiating it. In the classical picture, this is a continuous process whereas in a quantum mechanical description the radiation is quantised. Hence, the discretised scattering rate of an atom can be defined as

$$\Gamma_s = \frac{|E_0|^2}{2\hbar} \text{Im}[\alpha(\omega)]. \tag{2.8}$$

2.1.2   Dipole force

The cycle-averaged interaction energy between the atom and the field is given by

$$U = -\frac{1}{2} \left\langle \text{Re}[\vec{d}(t) \cdot \vec{E}(t)] \right\rangle = -\frac{1}{4} \text{Re}[\alpha(\omega)]|E_0|^2. \tag{2.9}$$

The factor $1/2$ accounts for the fact that the dipole moment of the atom is induced by the external field. When the electric field has a spatial dependence, e. g., $E_0(r)$, a dipole force $\vec{F} = -\vec{\nabla}U(r)$ arises as a result of the spatial variation of U. Hence, the dipole force can be expressed as

$$\vec{F} = \frac{1}{4} \text{Re}[\alpha(\omega)]\vec{\nabla}(|E_0(r)|^2). \tag{2.10}$$

Note that the dipole force points to the region with the largest value of $|E_0(r)|^2$ when $\text{Re}[\alpha(\omega)] > 0$, i. e., $\omega < \omega_0$, and to the region with the lowest value of $|E_0(r)|^2$ when $\omega > \omega_0$. The Lorenz model of the atom describes in good approximation the scattering rate and the dipole potential for a two-level atom in the ground state. However, the model is not accurate when $\omega \simeq \omega_0$ because a non-vanishing population of the excited state modifies the polarisability of the atom. Moreover, the model also fails in the limit of large $|\omega - \omega_0|$ because in this case the multi-level structure of the atom must be taken into account. In the following sections valid approximations for each of this limiting cases will be given.

2.2   Near-resonant atom-field interaction: Saturation and power broadening

This section is devoted to the description of the scattering rate and the dipole potential of a two-level atom in the presence of a near-resonant electromagnetic field. The quantum state of the atom is described as $|\psi\rangle = c_g \, |g\rangle + c_e \, |e\rangle$, where $|g\rangle$ and $|e\rangle$ refer to the ground and the excited state, respectively. The population in the excited state $|e\rangle$ in the steady-state regime of the atom-field interaction is given by [4]

$$|c_e|^2 = \frac{|\Omega|^2/2\gamma^2}{1 + |\Omega|^2/\gamma^2 + (2\delta/\gamma)^2}, \tag{2.11}$$

where $\Omega = \langle g|\vec{E}\cdot\vec{d}\,|e\rangle/\hbar$ denotes the Rabi frequency, $\delta = \omega - \omega_0$ the detuning of the angular frequency of the laser, and γ the spontaneous emission rate of the atom. It is convenient to write these expressions as a function of the free-space saturation intensity of the atom I_s, which is widely used as a characteristic value for a given transition:

$$\frac{|\Omega|^2}{\gamma^2} = \frac{|\vec{E}|^2}{\gamma^2\hbar}|\langle g\mid \vec{d}\mid e\rangle|^2 = I/I_s, \tag{2.12}$$

where I denotes the free-space intensity of the field

$$I = \varepsilon_0 c \left\langle \text{Re}[\vec{E}(t)^2]\right\rangle, \tag{2.13}$$

and

$$I_s = \gamma\frac{\pi\hbar\omega}{3\lambda^3}. \tag{2.14}$$

In the case of an atom coupled to the evanescent field of an ultra-thin optical fibre Eq. (2.14) is an approximation applicable provided that $|\vec{E}_z|^2$ is small compared to $|\vec{E}|^2$.

2.2.1 Scattering rate

Since in the steady-state regime the excitation rate must be equal to the decay rate, the scattering rate of the atom is given by

$$\Gamma_s = \gamma|c_e|^2 = \gamma\frac{I/2I_s}{1 + I/I_s + (2\delta/\gamma)^2}. \tag{2.15}$$
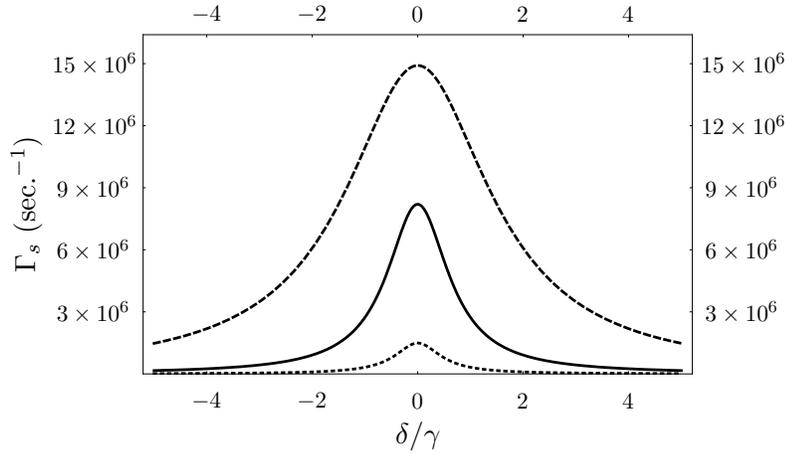

FIGURE 2.2: Scattering rate Γ_s for the $6^2S_{1/2}$, $F = 4 \rightarrow 6^2P_{3/2}$, $F' = 5$ transition of a caesium atom interacting with an electromagnetic field with intensity $I = 0.1I_s$ (dotted), I_s (solid) and $10I_s$ (dashed) as a function of the ratio δ/γ. $\gamma/2\pi = 5.2$ MHz for this transition.

Figure 2.2 shows the scattering rate for the D_2-line of a single caesium atom as a function of the ratio δ/γ for three different intensities of the laser field $I = 0.1I_s$ (dotted), I_s (solid) and $10I_s$ (dashed). Note that despite the intensities grow in factors of 10, the maximal scattering rate does not. Indeed, the value of the scattering rate saturates for $I > I_s$ leading to a smaller percentual increase in each step. This feature is called *saturation*. As a result, Γ_s approaches $\gamma/2$ in the limit of large intensities. Moreover, Γ_s is independent of δ in the regime where $I/I_s \gg (2\delta/\gamma)^2$. Hence, the scattering profile becomes broader when increasing the intensity I, this is the so-called *power broadening*. The power-broadened linewidth is then given by

$$\gamma' = \gamma\sqrt{1 + I/I_s}. \tag{2.16}$$

Note that for I/I_s exceeding 10^3, the two-level atom assumption is not valid anymore for the D_2-line in caesium because the neighbouring hyperfine levels have a separation of about 200 MHz, i. e., such a strong field can excite more than one transition.

2.2.2 Dipole force

The large population of the excited state reached in the saturation regime modifies the dipole potential given by Eq. (2.9). This stems from the different polarisabilities of the ground state $|g\rangle$ and the excited state $|e\rangle$, which cannot be explained using the Lorenz model. In the near-resonant case, the two polarisabilities are equal and opposite in sign [51]:

$$\alpha_g(\omega) = -\alpha_e(\omega). \tag{2.17}$$

The polarisability of a two-level atom is assumed to be of the form

$$\alpha(\omega, I) = \alpha_g(\omega)|c_g|^2 + \alpha_e(\omega)|c_e|^2. \tag{2.18}$$

The population of the states satisfies the relation $|c_g|^2 + |c_e|^2 = 1$. It is thus possible to use Eqns. (2.11), (2.12), (2.17) and (2.18) to obtain

$$\alpha(\omega, I) = \alpha_g(\omega)\left(1 - \frac{I/I_s}{1 + I/I_s + (2\delta/\gamma)^2}\right). \tag{2.19}$$

Since the polarisability of the ground state $\alpha_g(\omega)$ is well described by the Lorenz model, the results from Sec. 2.1 can be used to further simplify Eq. (2.19): Equations (2.5) and (2.6) are approximated for the case of $\omega \simeq \omega_0$ and substituted in Eq. (2.19) identifying $\Gamma = \gamma$. This yields

$$\mathrm{Re}[\alpha(\omega, I)] = -\frac{6\pi\varepsilon_0 c^3}{\omega_0^3}\frac{2\delta/\gamma}{1 + I/I_s + (2\delta/\gamma)^2}, \tag{2.20}$$

$$\mathrm{Im}[\alpha(\omega, I)] = \frac{6\pi\varepsilon_0 c^3}{\omega_0^3}\frac{1}{1 + I/I_s + (2\delta/\gamma)^2}. \tag{2.21}$$

Note that multiplying Eq. (2.21) by $I/2\hbar$ and making use of Eqns. (2.12)–(2.14) the scattering rate of the atom given by (2.15) is recovered. The dipole force exerted on the atom is then given by

$$\vec{F} = \frac{1}{2}\text{Re}[\alpha(\omega, I)]\vec{\nabla}\left\langle \text{Re}[\vec{E}(r,t)^2] \right\rangle, \tag{2.22}$$

which can be conveniently expressed as

$$\vec{F} = -\frac{\hbar}{2}\frac{\delta}{1 + I/I_s + (2\delta/\gamma)^2}\vec{\nabla}(I/I_s). \tag{2.23}$$

2.3   Far detuned atom-field interaction

For large values of the detuning of the laser frequency with respect to the atomic excitation frequency the multilevel structure of the atom must be taken into account. Therefore, the two-level atom approximation is not valid anymore.

2.3.1   Semiclassical approach

In this section a semiclassical approximation for the atom-field interaction including the multilevel structure of the atom is given. Let us consider a multilevel atom with a number j of dipole-allowed transitions from the ground state to excited states. Each transition can be approximated as an independent harmonic oscillator with solution

$$\vec{d_j}(t) = \alpha_j(\omega)\vec{E}(t). \tag{2.24}$$

Hence, the general solution will be a linear combination of the individual solutions weighted by the oscillator strength of each transition f_j yielding

$$\alpha(\omega) = \sum_j f_j\alpha_j(\omega). \tag{2.25}$$

The oscillator strength f_j is related to the decay rate of each transition [52] through

$$f_j = \Gamma_j\frac{2\pi\varepsilon_0 m_e c^3}{e^2\omega_j^2}\frac{2J'+1}{2J+1}. \tag{2.26}$$

ω_j denotes the angular frequency of the j-transition, $\omega_j = (E_{e,j} - E_g)/\hbar$. The factor $2J'+1/2J+1$ in the above equation is the ratio between the degeneracies of the excited and ground states, e. g., for a fine-structure transistion $J = 1/2 \rightarrow J' = 3/2$ the factor will be 4/2. Finally, the real and complex parts of the polarisability become

$$\text{Re}[\alpha(\omega)] = 2\pi\varepsilon_0 c^3 \sum_j \frac{2J'+1}{2J+1} \frac{(\omega_j^2 - \omega^2)\Gamma_j/\omega_j^2}{(\omega_j^2 - \omega^2)^2 + \Gamma_j^2(\omega^3/\omega_j^2)^2}, \tag{2.27}$$

$$\text{Im}[\alpha(\omega)] = 2\pi\varepsilon_0 c^3 \sum_j \frac{2J'+1}{2J+1} \frac{\Gamma_j^2\omega^3/\omega_j^4}{(\omega_j^2 - \omega^2)^2 + \Gamma_j^2(\omega^3/\omega_j^2)^2}. \tag{2.28}$$

With use of Eqns. (2.27) and (2.28), together with Eqns. (2.8) and (2.10) the dipole potential and the scattering rate of the atom can be calculated.

2.3.2 Light shifts in multilevel atoms

A perturbative description of the interaction of a classical field $\vec{E}(t) = \vec{E}_0 e^{i\omega t}$ with a multi-level atom yields the energy shift $\Delta\mathcal{E}_l$ of the atomic level $|l\rangle$ with an energy of $\mathcal{E}_l$ and quantum numbers n, J, F, m_F [53]:[1]

$$\Delta\mathcal{E}_l(n, J, F, m_F, \mu) = -\frac{3e^2 I}{4m_e c \varepsilon_0}(2J+1)(2F+1)$$
$$\sum_{n',J',F',m'_F}(2F'+1)\frac{f_j}{\omega_j\Delta'_j}\begin{pmatrix} F & 1 & F' \\ -m_F & -\mu & m'_F \end{pmatrix}^2 \begin{Bmatrix} J & F & I \\ F' & J' & 1 \end{Bmatrix}^2.$$

$$(2.29)$$

The parameter μ accounts for the polarisation of the electric field, $\mu = \pm 1$ for $\sigma^\pm$ and $\mu = 0$ for π-polarisation, f_j is the oscillator strength of the transition j: $nJ \rightarrow n'J'$ given by Eq. (2.26), and Δ'_j is the effective detuning of the angular frequency defined as

$$\frac{1}{\Delta'_j} = \frac{1}{\omega_j - \omega} + \frac{1}{\omega_j + \omega}. \tag{2.30}$$

The terms $\left(...\right)$ and $\left\{...\right\}$ are Wigner's $3J$- and $6J$-symbols, respectively, which are a generalisation of the Clebsch-Gordan coefficients [54].[2]

Figure 2.3 shows the frequency shifts $\Delta\mathcal{E}/h$ of the $6P_{3/2}, F = 5$ (top) and $6S_{1/2}, F = 4$ (bottom) levels of the Cs atom induced by a light field with intensity $I = 0.3$ MW/cm^2 at a wavelength of 780 nm (dashed) and 1064 nm (solid) for π-polarisation. The shifts show the dependency on the hyperfine quantum number m_F described in Eq. (2.29). However, for an external light field with π-polarisation there is no favoured direction of rotation and the m_F dependency turns into an $|m_F|$ dependency.

In a quantum-mechanical description the dipole potential manifests on the energy shifts of the internal states of the atom as $U_l(\vec{r}) = \mathcal{E}_l + \Delta\mathcal{E}_l(\vec{r})$. In a spatially dependent electric field the atom will, therefore, experience a force in the direction of the negative gradient of the energy given by

$$\vec{F}_l = -\vec{\nabla}(\Delta\mathcal{E}_l(\vec{r})). \tag{2.31}$$

---

[1]Note that the convention used in [53] differs from the one used here: $|\langle nJ||d||n'J'\rangle|^2$ corresponds to $(2J+1)|\langle nJ||d||n'J'\rangle|^2$ in this work. This stems from the different conventions for the normalisation of the matrix elements $\langle nJ||d||n'J'\rangle$. In this work the convention used in [52] is followed.

[2]Many computer programs have a library with such functions that allows rapid implementation of Eq. (2.29), see for example Mathematica 4.2 and higher.
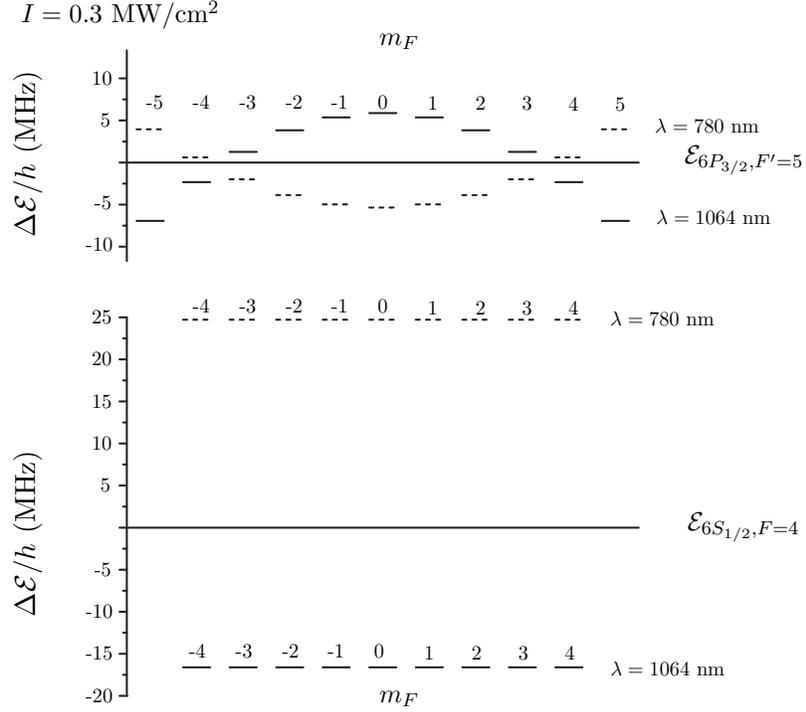
FIGURE 2.3: Frequency shifts $\Delta\mathcal{E}/h$ of the $6P_{3/2}, F' = 5$ (top) and $6S_{1/2}, F = 4$ (bottom) levels of the Cs atom in interaction with an external field of intensity $I = 0.3$ MW/cm^2 at a wavelength of 780 nm (dashed) and 1064 nm (solid) with π-polarisation. The x-axis represents the energy levels of the unperturbed states, $\mathcal{E}_{6P_{3/2}, F'=5}$ (top) and $\mathcal{E}_{6S_{1/2}, F=4}$ (bottom).

For the case of an atom interacting with more than one light field simultaneously, the total energy shift is the sum of the individual shifts $\Delta\mathcal{E}_{l,\Omega}$ due to each of the fields, $\vec{E}_\Omega$ [55]. The force is therefore expressed as

$$\vec{F}_l = -\sum_\Omega \vec{\nabla}(\Delta\mathcal{E}_{l,\Omega}(\vec{r})). \tag{2.32}$$

Chapter 3

Evanescent field spectroscopy on cold caesium atoms

3.1 Introduction

Ultra-thin optical fibres offer a strong transverse confinement of the fundamental fibre mode while exhibiting a pronounced evanescent field surrounding the fibre [37]. This combination allows to efficiently couple particles on or near the fibre surface to the guided fibre mode, making tapered optical fibres (TOFs) a powerful tool for their detection, investigation, and manipulation: The absorbance of organic dye molecules, deposited on a subwavelength-diameter TOF, has been spectroscopically characterised via the fibre transmission with unprecedented sensitivity [33]. The fluorescence from a very small number of resonantly irradiated atoms around a 400-nm diameter TOF, coupled into the guided fibre mode, has been detected and spectrally analysed [34, 38]. Moreover, it has also been proposed to trap atoms around ultra-thin fibres using the optical dipole force exerted by the evanescent field [26, 39]. In this chapter, the transmission of a resonant probe laser launched through a TOF is spectroscopically investigated. Thereby, clear evidence of the mechanical effects of dipole forces on the atoms is found, leading to a modification of the atomic density in the vicinity of the fibre. A rigorous analysis furthermore shows that a detailed description of the absorption signal must take the interaction of the atoms with the dielectric fibre into consideration (Sec. 3.7.2). In particular, this includes the mechanical and spectral effects of the van der Waals (vdW) interaction [56] and a significant enhancement of the spontaneous emission rate of the atoms due to a modification of the vacuum modes by the fibre [57]. An enhanced spontaneous emission of atoms *in vacuo* coupled to a continuous set of evanescent modes has previously been observed in evanescent wave spectroscopy near a plane dielectric surface [23]. Here, the atoms are interacting with a cylindrical ultrathin dielectric fibre which, in difference to the plane geometry above, also sustains a strongly confined mode. This single mode significantly contributes to the enhancement of the spontaneous

emission, an effect which so far has only been observed before in experiments including a resonant structure [58].

3.2   Experimental setup

The experimental setup used to perform the experiments described in this Chapter was located in two different sites. From September 2004 to February 2007 the experiment was located in the Institut für Angewandte Physik (IAP) at the University of Bonn. From March 2007 until present the experiment is located in the Institut für Physik at the University of Mainz. When moving from Bonn to Mainz the experimental setup underwent several modifications and a number of elements of the original setup were substituted. Since the majority of the experiments have been performed using the original setup, I will focus the description on it. To account for the new elements, a list of substitutions and their description will be given at the end of each section. Finally, a schematic of the new setup is shown in Chap. 5. Moreover, when experiments have been performed with the new setup this will be mentioned in their presentation. If nothing is mentioned the original setup was used. The reader should bear in mind that the new and the original setups are equivalent regarding the experiments presented in this Chapter.

Figure 3.1 shows a schematic of the original experimental setup. A list of the labelled elements can be found in Table 3.1 together with the section were their description can be found. Some optical (4, 5, 6, 7, 9, 10, 18) and mechanical (20) elements will not be described in this work but can be, e. g., found in [59]. As shown in the schematic, the vacuum chamber (11) was mounted on a second optical table separated from the lasers (1–3) and spectroscopy setups (21, 22). The laser light was then guided to the second table with polarisation maintaining optical fibres (31). There are two characteristics of the setup that are not reflected in Fig. 3.1: Firstly, the turbo and pre-vacuum pumps are connected to the vacuum chamber via flexible bellows (23). Indeed, the pre-vacuum pump is located in a different room than the rest of the experiment. Secondly, there is a second imaging system located above the vacuum chamber (see Fig. 3.2). The description of this system is given in Sec. 3.3.3.

The mode filter (16) consists of a 2-mm un-jacketed section of the fibre embedded in index-matching gel. This ensures that the light propagating outside the core in the so-called cladding modes will be out-coupled before reaching the APD (15). Figure 3.2 shows a schematic of the vacuum chamber and the geometry of the magnetic coils. The labelling of Fig. 3.1 and Table 3.1 has been followed. The vertical imaging system (32) and the optical table supporting the vacuum apparatus can be appreciated. The ion getter pump shown in the figure was not used for the experiments: The influence of charged particles on the fibre is unknown. Hence, to avoid the presence of charged particles in the vacuum chamber that could damage the fibre the ion getter pump was switched off.

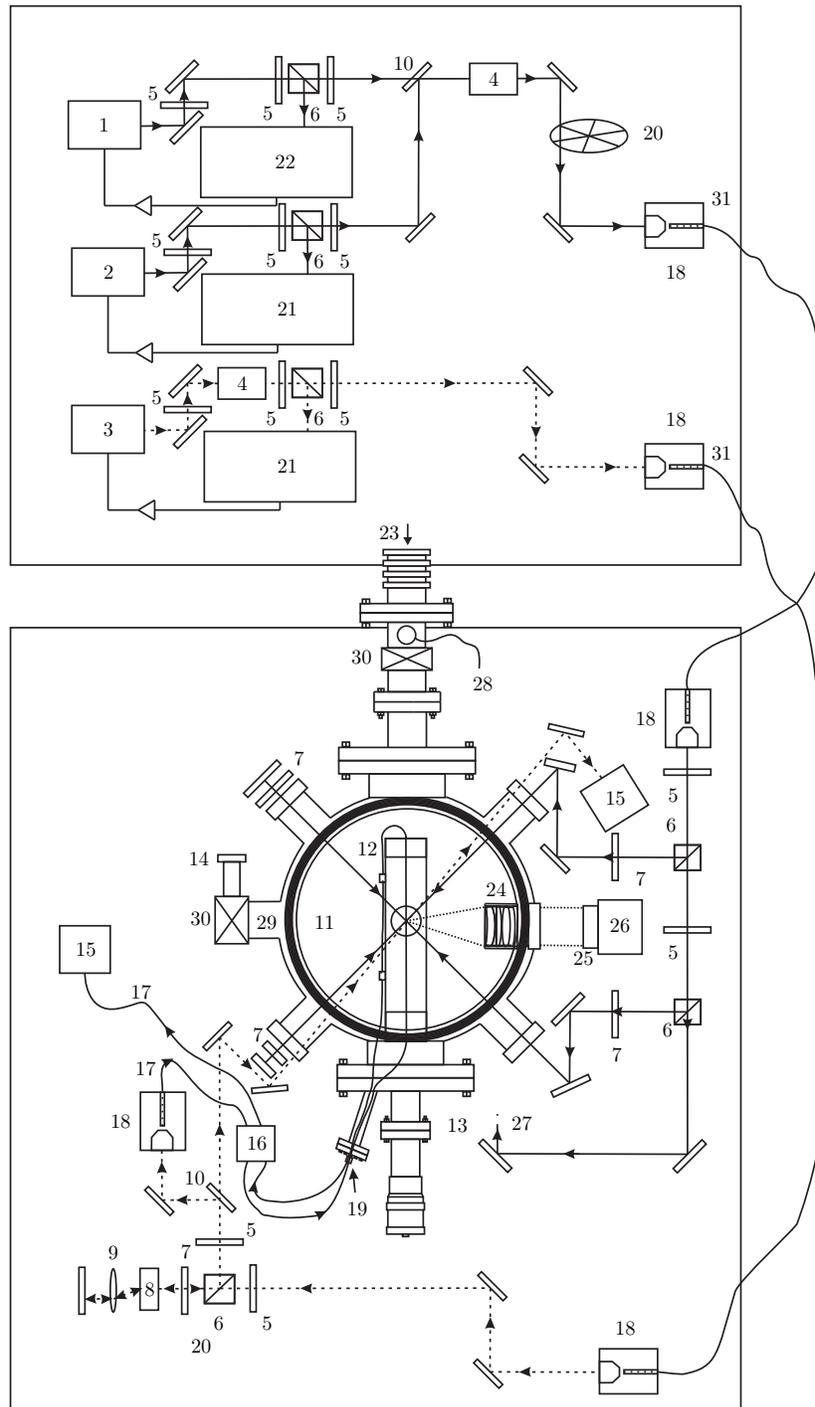FIGURE 3.1: Schematic of the original experimental setup located in the IAP at the University of Bonn. The mirrors have not been labelled. The solid arrows indicate the path of the beams used for the magneto-optical trap. The dashed arrows indicate the path of the probe beam.
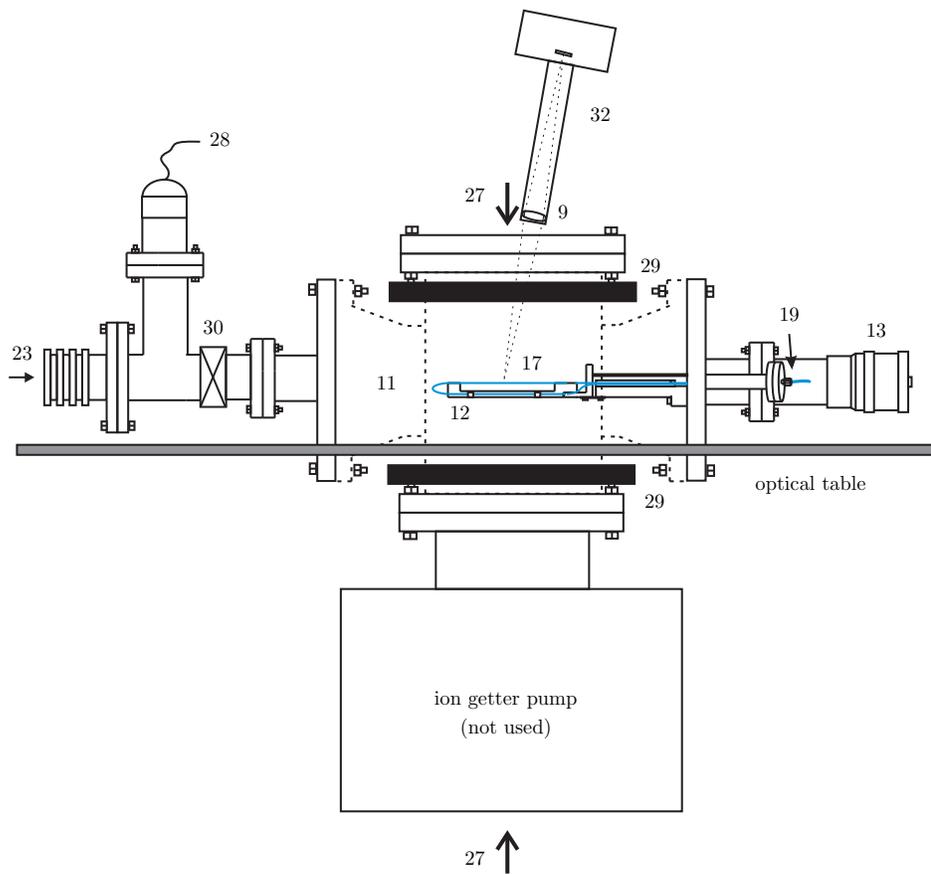
FIGURE 3.2: Schematic of the vacuum apparatus located in the IAP at the University of Bonn. The ion getter pump was attached to the chamber but not used.

Number	Description	Section
1	cooling laser	3.3.1
2	repump laser	3.3.1
3	probe laser	3.4
4	Faraday isolator	–
5	$\lambda/2$ plate	–
6	polarising beam splitter	–
7	$\lambda/4$ plate	–
8	acousto-optical modulator (AOM)	3.4
9	convex lens	–
10	glass substrate	–
11	vacuum chamber	3.3.1
12	fibre mount	3.3.2
13	fibre positioner	3.3.2
14	Cs reservoir	3.3.1
15	avalanche photodiode (APD)	3.4
16	mode filter	–
17	TOF	1.3
18	fibre coupler	–
19	vacuum feed-through for fibres	3.3.2
20	chopper wheel	–
21	polarisation spectroscopy setup	3.3.1
22	saturation spectroscopy setup	3.3.1
23	turbo and pre-vacuum pumps	3.3.1
24	microscope objective	3.3.3
25	camera objective	3.3.3
26	CCD-camera	3.3.3
27	vertical MOT beam	3.3.1
28	pressure gauge	3.3.1
29	magnetic coils	3.3.1
30	valve	–
31	polarisation-maintaining optical fibre	–
32	vertical imaging system	3.3.3

TABLE 3.1: List of elements labelled in Figs. 3.1 and 3.2.

3.3 A caesium magneto-optical trap around an ultra-thin optical fibre

Probing and investigating cold caesium atoms using the evanescent field around an ultra-thin optical fibre requires a sufficiently high atomic density at the vicinity of the fibre. A simple way to tackle the problem is to insert the waist of a TOF into a magneto-optical trap (MOT). Using this method, it has been shown that caesium atoms can be cooled and trapped around an ultra-thin optical fibre with a diameter smaller than 1 μm.[1] One could expect that the presence of the fibre affects the density of the cloud of atoms

---

[1] fibres with larger diameter in such a system have not been investigated

trapped in the MOT. Indeed, a rigorous investigation of the atomic density distribution inside the MOT using Monte-Carlo simulations reveals a significant influence of the fibre on the density of the cloud at distances closer than 1 μm from the surface (see Sec. 3.7.3). Nevertheless, the measured peak densities of the atom cloud do not differ from the typical peak density of an unmodified MOT of about 10^{10} atoms/cm^3 [60] (see Sec. 3.8).

3.3.1 Magneto-optical trap for caesium atoms

During the last two decades the magneto-optical trap (MOT) has become one of the most widely used tools to cool and trap neutral atoms [61–63]. The first experimental realisation of three dimensional laser cooling of atoms was reported by S. Chu in 1985 [64]. By adding a magnetic field gradient in combination with the right polarisation and frequency of the cooling beams an additional position-dependent force acting on the atoms was obtained. Thereby, laser cooling and trapping of sodium atoms in a MOT could be demonstrated few years later [65]. The principle of operation of a magneto-optical trap relies on two forces: A velocity-dependent force that cools the atoms and a position-dependent force that traps them.
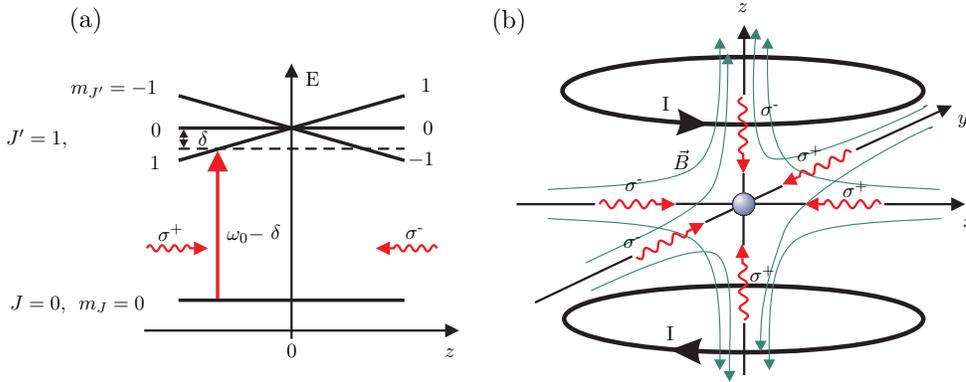

FIGURE 3.3: (a) One-dimensional scheme of the operating principle of a magneto-optical trap. The atomic ground and excited states are chosen to be $J = 0$ and $J' = 1$, respectively. A magnetic field $B_z = b \times z$ produces an energy shift of the corresponding Zeeman sub-levels. ω_0 denotes the resonance frequency of the transition $J \to J'$ at $B_z = 0$ and δ the detuning of the angular frequency of the laser beams with respect to ω_0. The laser beams are indicated by the red curly arrows. (b) Three-dimensional scheme of a MOT. The quadrupole magnetic field is created using two coils in anti-helmholtz configuration indicated by the two circulating arrows denoted by I. The green lines indicate the direction of the magnetic field. The centre of the trap is located at the crossing of the beams.

Velocity-dependent force: Three mutually orthogonal pairs of counter-propagating laser beams that cross at the centre of the trap are used. The frequency of the laser

beams is red-detuned by about the natural linewidth $\gamma/2\pi$ of the considered transition[2]. Due to the Doppler shift of the laser frequency in the reference frame of a moving atom, the absorption of a photon is more likely if the momenta of the atom and the photon have opposite sign. Therefore, an atom will more likely absorb photons from the beam propagating opposite to its direction of motion. Since the atom spontaneously emits the photons in a random direction, the net average momentum change after several absorption-emission cycles is opposite to its direction of motion. This leads to a three-dimensional velocity-dependent force (friction) at the intersection of the beams that cools the atoms. On the other hand, an atom continuously illuminated by a near resonant field will also undergo heating, even at rest. This stems from the randomness of the spontaneous emission which acts as a fluctuating force exerted on the atom. The competition between the cooling and the heating processes leads to a stationary state where the momentum of the atoms is described by a Maxwell-Boltzmann distribution with a characteristic temperature $T_D = \hbar\gamma/2k_B$ [4], where k_B is the Boltzmann constant. In absence of other processes that lead to further cooling of the atomic cloud (e. g., polarisation gradient cooling [66]) T_D determines the temperature of the atoms in a MOT.

Position-dependent force: In order to obtain a restoring force that traps the atoms a quadrupole magnetic field $\vec{B}(x, y, z)$ that vanishes at the centre of the trap and increases linearly in all directions is used. The magnetic field shifts the Zeeman sub-levels of the atoms by $\Delta E(x, y, z) = \mu_B m_{J'} B(x, y, z)$, where μ_B denotes Bohr's magneton and $m_{J'}$ is the considered Zeeman sub-level of the atom. Hence, the atomic energy levels are shifted by an amount proportional to the distance of the atom from the trap centre. Figure 3.3 (a) shows the energy level diagram of an atom inside the trap assuming a one-dimensional linear magnetic field $B_z = b \times z$. The ground state has been chosen to be $J = 0$ and the excited state $J' = 1$, where J denotes the total angular momentum of the atom. The atoms are illuminated with two laser beams, one with polarisation σ^+ propagating in the $+z$-direction and another with polarisation σ^- propagating in the $-z$-direction. When the frequency of the laser beams is tuned below the resonance frequency of the $J \rightarrow J'$ transition one atom located at $z < 0$ will absorb more σ^+ than σ^- photons and will experience a net force towards $z = 0$. Analogously, one atom located at $z > 0$ will absorb more σ^- than σ^+ photons and will also experience a net force towards $z = 0$.

The generalisation to three-dimensions is then straightforward. Figure 3.3 (b) shows a three-dimensional scheme of a MOT with three pairs of counter-propagating laser beams indicated by the curly arrows. The inhomogeneous magnetic field is generated by two coils in anti-Helmoltz configuration [67] with the point of zero magnetic field located at the intersection of the beams. In summary, the combination of the inhomogeneous magnetic field and the red-detuned counter-propagating laser beams with the appropriate choice of the polarisation and the detuning produces both a friction and a restoring

---

[2]The following notation is used in this work: δ denotes the detuning of the angular frequency of the laser ω with respect to the angular frequency of the atomic transition ω_0. γ denotes the spontaneous emission rate of the atoms and consequently $\gamma/2\pi$ denotes the natural linewidth of the atomic transition.

force that simultaneously traps and cools the atoms. The density and the size of the cloud of atoms trapped in the MOT depends on the chosen parameters for the lasers and the magnetic field gradient. With the parameters used in our setup the atom cloud has a typical diameter of 1 mm (see Sec. 3.3.3) and a typical peak atomic density of 10^{10} atoms/cm^3 (see Sec. 3.8).

Laser system

The simplified picture assuming a $J = 0 \rightarrow J' = 1$ excitation transition as shown in Fig. 3.3 (a) has to be extended to be applicable to a Cs atom which has a $J = 1/2$ ground state, a $J = 3/2$ excited state and a nuclear spin of $I = 7/2$. Figure 3.4 shows the hyperfine level scheme of the D$_2$-line of the caesium atom. The cooling transition is chosen to be the $F = 4 \rightarrow F' = 5$ which is the strongest hyperfine transition of the D$_2$-line [52]. Since the atoms in the $F' = 5$ state can only decay to the $F = 4$ state, the cooling cycle is closed. However, due to the relatively small hyperfine splitting of the excited $6^2P_{3/2}$ state there is a non-vanishing probability for the atoms to be excited to the $F' = 4$ state. The atoms can then decay to the $F = 3$ state which is no longer coupled to the cooling laser. In order to pump the atoms back to the $F = 4$ state the repump transition $F = 3 \rightarrow F' = 4$ is required.

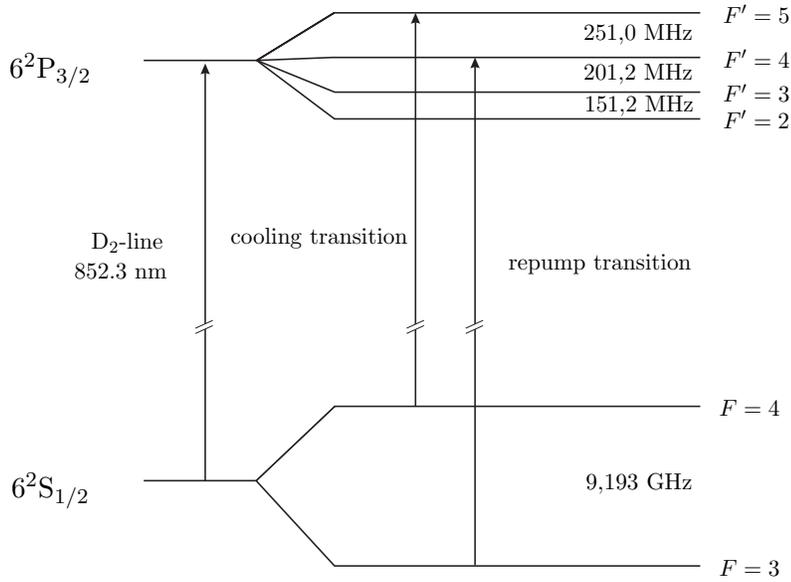FIGURE 3.4: Hyperfine level scheme of the D$_2$-line of the caesium atom. The arrows indicate the cooling and repump transitions.

In our experiment, the cooling transition is excited using a diode laser in Littrow configuration ((1) in Fig. 3.1) [68] which is actively frequency stabilised using a saturation spectroscopy setup ((22) in Fig. 3.1) [69]. The resulting reference signal allows to lock

the laser at a few γ detuned from the resonance, which suffices for the optimal realisation of a MOT. The linewidth of the $F = 4 \rightarrow F' = 5$ transition is $\gamma/2\pi = 5.22$ MHz leading to a Doppler temperature $T_D = 125$ μK for Cs. For an optimal operation of the MOT the power of the cooling laser in each of the six beams must be equal. The typical power of the cooling laser at which our MOT was operated is 5 mW per beam with a $1/\sqrt{e}$-diameter of 8 mm.

The repump transition is excited using a diode laser in Littrow configuration ((2) in Fig. 3.1) which is actively frequency stabilised using a polarisation spectroscopy setup ((21) in Fig. 3.1) [69] with a power of 50 μW in each of the six beams. The cooling and repump lasers are first coupled to the same single mode optical fibre and afterwards separated in six beams following the configuration shown in Figs. 3.1 and 3.3 (b).

In the new setup the cooling transition is excited with a tapered amplifier laser system (Sacher, SYS-420-0850-0500) with a maximum output power of 500 mW ((1) in Fig. 5.9). The repump transition is excited with a diode laser in Littrow configuration (Sacher, TEC100) with a maximum output power of 50 mW ((2) in Fig. 5.9). The guiding of the lasers from the optical table to the chamber is realised by means of a fibre cluster (Schäfter+Kirchhoff) with the integrated optics necessary for the adjustment of the power and polarisation of the six MOT beams ((41) in Fig. 5.9). The laser beams are outcoupled from the cluster using 6 fibre collimators (60SMS-1-4-A11-02) that provide a beam diameter of about 10 mm.

Magnetic coils

The quadrupole magnetic field is created by two coils in anti-helmholtz configuration along the z-axis ((29) in Figs. 3.1 and 3.2). The coils have a radius of 10 cm and carry a current ranging from 5 to 8 A providing a magnetic field gradient between 5 and 9 Gauss/cm. The magnetic field gradient can be turned off within 1 ms ($1/e$-decay time) using a field-effect transistor (FET) controlled by a TTL signal. The $1/e$-decay time was measured by placing a pickup coil near the vacuum chamber during the switching and monitoring the induced current in the oscilloscope.

Vacuum system

The experiment takes place in ultra-high vacuum (UHV) environment inside a stainless-steel vacuum chamber of approximately 7000 cm^3 ((11) in Figs. 3.1 and 3.2). A turbo-molecular pump with an evacuation power of 270 l/s is connected to the chamber with a bellow ((23) in Figs. 3.1 and 3.2). The pre-vacuum pump is connected to the turbo-molecular pump with another bellow. Both pumps in continuous operation provide a base pressure of 4×10^{-9} mbar without baking the chamber. The pressure in the vacuum apparatus is measured with a gauge at the connection between the chamber and the bellow ((28) in Fig. 3.2). For this reason, it is possible that the real pressure in

the chamber is slightly higher. Nevertheless, the pressure increases by about a factor of 10 when operating the MOT due to the background of Cs gas.

The chamber has a total of ten flanges for the access of the following elements: Six glass view-ports anti-reflection coated at 852 nm, one home-built microscope objective for the observation of the magneto-optical trap and the waist of the TOF ((24) in Fig. 3.1), the bellow connecting the turbo-molecular pump (23), the Cs reservoir (14), and the UHV-compatible fibre positioner (13) (see Sec. 3.3.2).

In the new setup a turbo-molecular pump with magnetic bearings (Pfeiffer, TMU-200-MP-DN-100-CF-F) with an evacuation power of 180 l/s and a oil-free pre-vacuum pump (Leybold, Scroll SC15D) are used ((23) and (22) in Fig. 5.9, respectively). The turbo-molecular pump is flanged to the chamber with a vibration-damper ((40) in Fig. 5.9) (Pfeiffer, PM006488-X) providing a base pressure of the vacuum apparatus of 1×10^{-9} mbar. The vibration damper is necessary due to the high-frequency rotation of the turbo-pump (800 Hz) which transmits vibrations to the chamber and to the optical table. Moreover, the pre-vacuum pump transmits mid- and low-frequency vibrations to the turbo-pump. Therefore, the chamber is mounted on the optical table with use of high-charge vibration damping mounts (Talleres Egaña SL., ESA50).

Sources of caesium atoms

A background gas of Cs atoms in the chamber is obtained using a Cs reservoir consisting of a cylindric enclosure flanged to the vacuum chamber with an elbow valve to ensure sealing ((30) in Fig. 3.1). Originally, the Cs was contained in a glass ampule within the reservoir. Once the reservoir is flanged and the chamber is evacuated the ampule is broken. When opening the valve, the Cs background pressure necessary to normally operate a MOT is obtained in less than a minute.

In the new setup the Cs reservoir has been substituted by Cs dispensers (SAES Getters) that provide a more accurate control of the amount of background gas in the chamber ((14) in Fig. 5.9). The dispensers consist of several layers of Cs in the form of a stable salt deposited on a metal wire. When applying a current to the wire ranging from 2 to 4 A the salt is heated and Cs vapor is released at a temperature of about 800 K. Since the effect of such a hot alkali atomic vapour on an ultra-thin optical fibre is unknown, the dispensers are placed in such a way that the released atomic vapour first thermalises upon collisions against the walls of the vacuum chamber. The current is applied using wires inserted in the chamber with a UHV-compatible electrical feed-through ((42) in Fig. 5.9).

3.3.2 Tools for embedding and manipulating an ultra-thin optical fibre in UHV

The properties of an ultra-thin optical fibre in vacuum do not differ from the properties of the same fibre in air except for the fact that the fibre cannot dissipate heat into the surrounding air. Due to the small thermal conductivity of silica, the black-body radiation is thus the only cooling mechanism of the fibre in such an environment. This is sometimes not sufficient to prevent the fibre waist to reach the melting temperature when a powerful laser is transmitted through it. The diverse mechanisms that trigger the fusing of the fibre are still unclear and will not be described in this work. This section is devoted to describe the elements used to insert and control the position of an ultra-thin optical fibre in UHV environment.

UHV-compatible fibre holder and positioning system

The tapered fibre is transferred from the pulling facility to the vacuum chamber using a custom-made aluminum fibre mount. Hence, the mount is designed to fit both in the pulling rig [36] and in the geometry of the MOT. Figure 3.5 shows a schematic of the transfer of the tapered fibre from the pulling rig onto the fibre mount. The fibre is
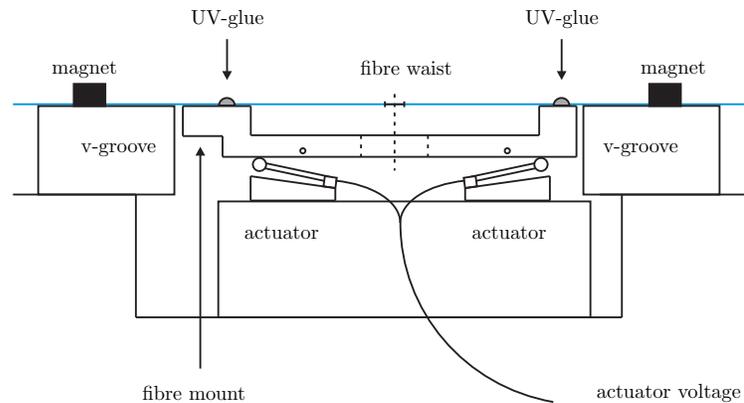

FIGURE 3.5: Schematic of the transfer of the tapered optical fibre from the pulling rig onto the fibre mount. The fibre is fixed to the mount using UV-glue.

mounted on the pulling stages using two v-grooves and is fixed with two magnets. Once the tapering process is completed the mount is placed underneath the fibre and moved upwards using two piezzo-actuators. The fibre waist is aligned to the centre of the hole of the mount with an estimated precision of ± 1 mm. This is necessary for the subsequent alinement of the fibre waist with the MOT inside the vacuum chamber (see Sec. 3.3.3). At the contact points between the fibre and the mount, two drops of UV-glue are applied to fixate it. Note that the contact positions must be located at the untapered region of the fibre to avoid losses. The magnets can be then carefully detached and the fibre

mount assembled with the body of a UHV-compatible fibre holder as shown in Figs. 3.6 (a), (b), and (c).

The vertical and side views of the UHV-compatible fibre holder used to mount the fibre in the vacuum are shown in Figs. 3.6 (a) and (b). The body of the holder is a stainless steel reducing adapter (DN 100 to DN 35) with a length of 7 mm (1). A UHV-compatible mechanical feed-through (4) is attached to the DN 35 flange. The holder is flanged to the chamber (2) with use of the DN 100 flange. To introduce the fibre inside the vacuum, a fibre feed-through is used (5). Its description can be found in the next section. The inset in (a) shows the aluminum mount where the fibre is fixated. As shown in Fig. 3.6 (c), the mount is attached to the holder using a junction consisting of a bronze plate (9) and a spring (7). The mechanical arm of the feed-through (8) presses the mount and the spring applies a restoring force allowing vertical displacement of the fibre of several centimetres inside the chamber. This is described by the red arrows in Figs. 3.6 (b) and (c).

The process of inserting the tapered fibre in the vacuum takes place at two locations: In the pulling facility where the fibre is transferred onto the mount and assembled to the fibre holder and on the optical table where the holder is flanged to the chamber. The pulling facility is equipped with a laminar flow box to minimise the risk of contamination of the fibre by dust [36]. In the new setup a second laminar flow box is located above the optical table and the vacuum chamber (see Fig. 5.10), whereas in the original setup this was not the case.

UHV feed-through for optical fibres

In the first stages of the experiment the optical fibre was coupled into the vacuum system by means of a stain-less steel con-flat flange with two holes. The fibre was threaded through the wholes and glued in such a way that the holes were obturated and thereby the chamber was sealed. However, this method is tedious. In the present an alternative approach based on a teflon ferrule as a feed-through for coupling optical fibres into UHV is used. This was first proposed by E. R. I. Abraham and E. Cornell in 1998 [70].

Figure 3.7 shows a sketch of the functioning of such feed-through. We use a standard stain-less Swagelok connector (SS-400-1-2RS) welded to a con-flat flange. The Swagelok metal ferrule is substituted by a custom-made ferrule of teflon with two axial holes to couple the optical fibre into the vacuum system. The optical fibre is threaded through the Swagelok nut, then through the ferrule and finally through the male connector welded to the flange. To seal the vacuum chamber the ferrule is inserted in the male connector and then fixed with the nut. When tightening the nut, the vacuum system is sealed. The nut is tightened one and a half full turns after finger-tight. The teflon inserts are permanently deformed via the tightening but the fibre does not brake inside the ferrule because the jacket protects it. Using this method the fibres can be easily
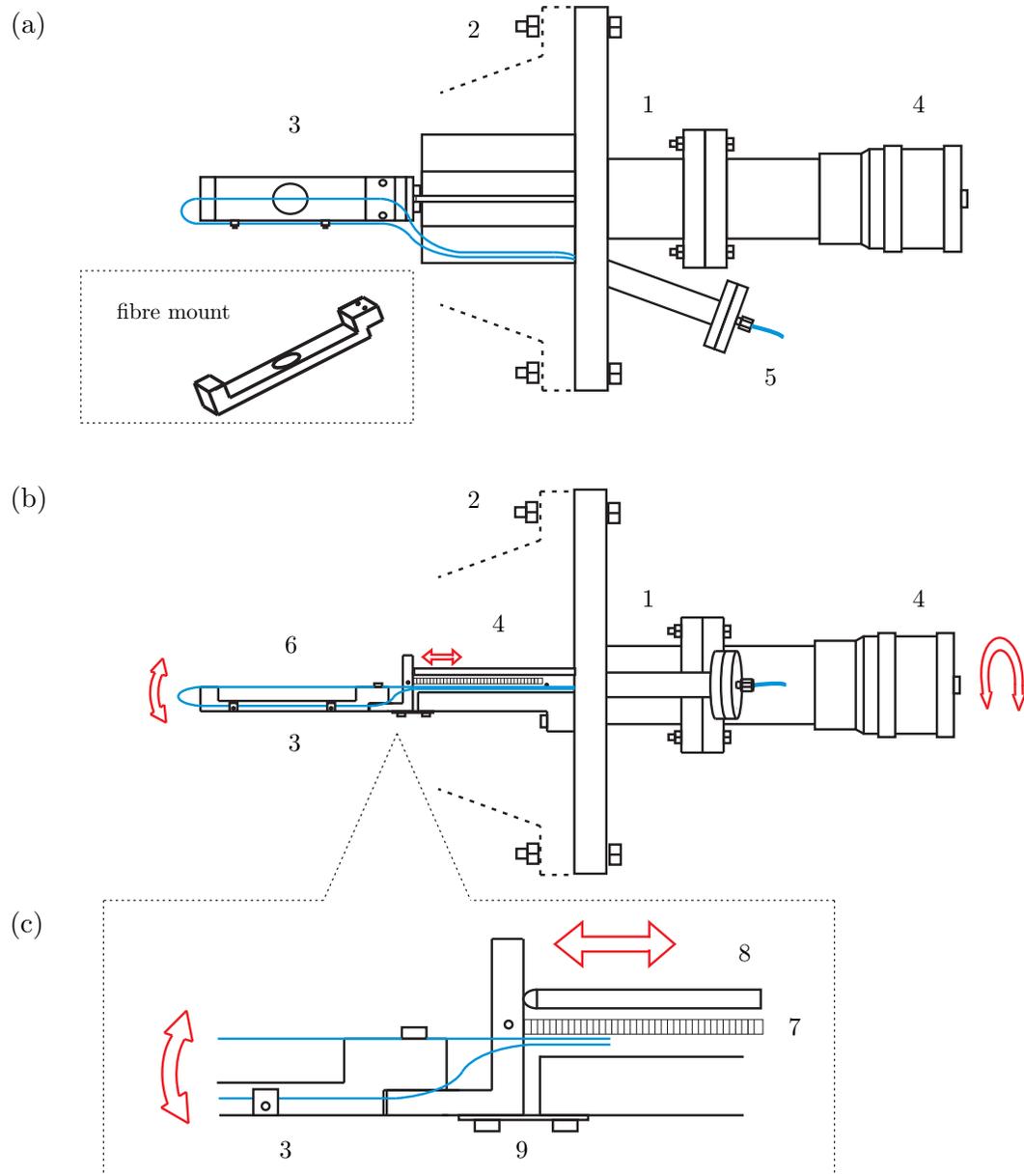
(a)

fibre mount

(b)

(c)

FIGURE 3.6: Vertical (a) and side (b) views of the fibre holder. (c) shows the junction between the fibre mount and the holder allowing vertical displacement of the fibre inside the chamber. The following elements are indicated: (1) reducing adapter, (2) vacuum chamber, (3) fibre mount (inset in (a)), (4) UHV-compatible mechanical feed-through (the red arrows indicate its functioning), (5) fibre feed-through, (6) TOF, (7) spring, (8) mechanical arm, (9) bronze plate.
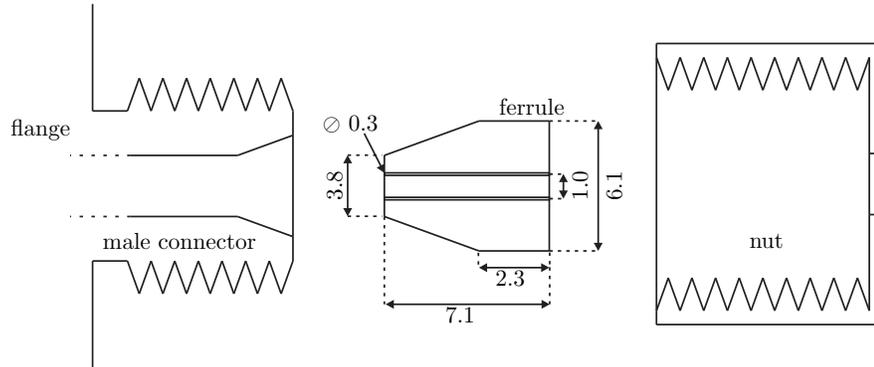
FIGURE 3.7: Section of the fibre feed-through system. All units are in millimetres.

removed and replaced. Moreover, no change in the evacuation speed with respect to the normally sealed chamber without the feed-through has been observed. The sealing has been leak-tested applying ethanol and acetone to the teflon junction and no subsequent increase of the pressure in the chamber has been observed. A Helium leak-test has also been performed. The ferrule is, indeed, not less sealant than the rest of the elements attached to the chamber. Moreover, the laser transmission through a fibre coupled into and out from the vacuum chamber using the teflon feed-through has been measured after tightening the nut for the optimal sealing with no noticeable change.
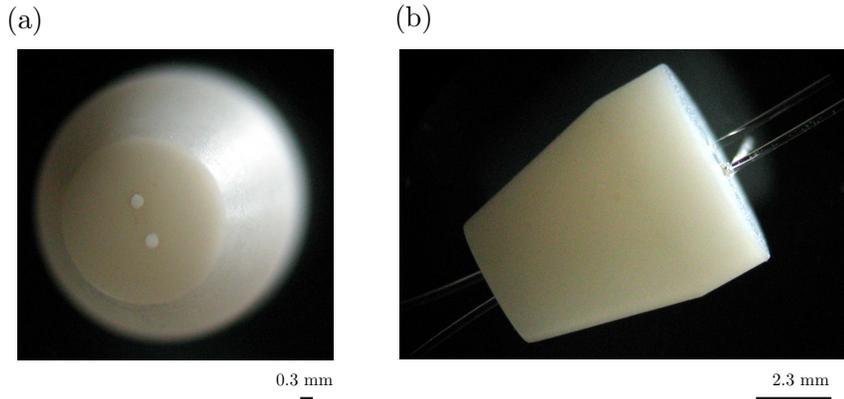

FIGURE 3.8: Front (a) and side (b) microscope images of a teflon ferrule machined in the workshop of the IAP at the University of Bonn. In the side view two fibres threaded through the holes are visible.

Figure 3.8 shows two microscope images of the teflon ferrule machined by the workshop of the Institut für Angewandte Physik (IAP) at the University of Bonn. The 0.3 mm diameter off-axis holes have been chosen to thread a standard single mode fibre with a diameter of 0.25 mm including the jacket.

3.3.3   Positioning of the fibre and the MOT

The optical system used for observing and positioning the fibre and the MOT is schematically shown in Fig. 3.9. We use two independent imaging systems with a relative angle close to 90° to simultaneously obtain a vertical and a lateral view of the fibre waist and the atomic cloud trapped in the MOT. The vertical image is obtained with a convex lens in $2f - 2f$ configuration outside the vacuum chamber that projects the image 1:1 onto the chip of a CCD-camera. The precision on the positioning of the MOT is limited by the spherical aberration of the system [42]. In our case this is calculated to be less than 0.2 mm. Since the image is formed due scattering of the MOT beams, the chromatic aberrations play no role in the imaging. The lateral imaging system ((24) in Fig. 3.1) uses an anti-reflection coated lens system with NA = 0.29 and a working distance of 36.5 mm [71]. The lens system is installed inside the vacuum chamber and the image is captured by the CCD-camera through a view-port. An iterative alinement process using both optical systems is followed: We displace the fibre towards the MOT using the positioner described in Fig. 3.6 (c) until they overlap in the lateral image. Then, using the vertical image we displace the atomic cloud towards the fibre until they overlap. By subsequently repeating this process a simultaneous overlapping in both images is achieved. The displacement of the atomic cloud is realised by means of a bias magnetic field. A strong permanent magnet placed at a few ten centimetres from the centre of the trap suffices to displace the MOT over a range of 4 mm. The iterated displacements of the MOT can produce a decrease in the density of the atomic cloud which can be corrected by re-adjusting the molasses.
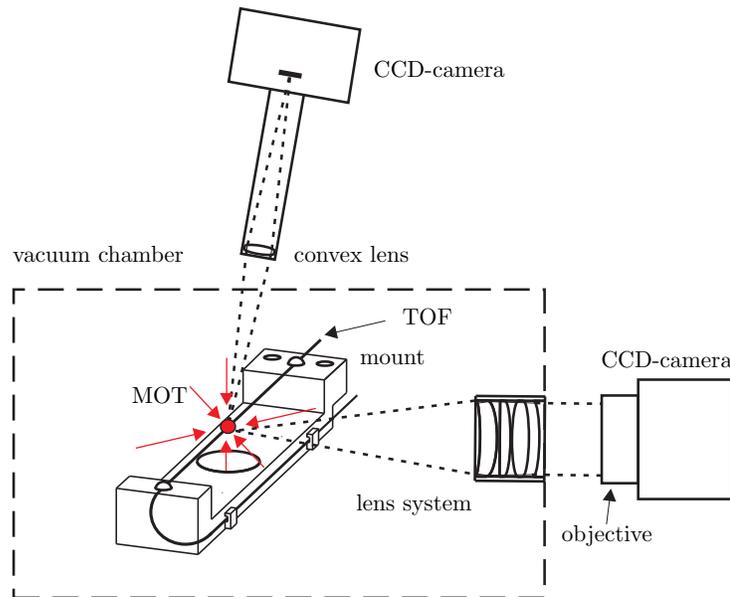

FIGURE 3.9: Optical system used for overlapping the fibre waist and the MOT.

Figure 3.10 shows a picture of the atomic cloud trapped in the MOT in overlap with
the waist of a TOF. The image was captured using the vertical imaging system shown
in Fig. 3.9 and was confirmed by the lateral imaging system to ensure 3D overlap of
the waist with the MOT. The fibre waist is visible due to the scattering of light from
the laser beams and is designed to have a diameter of 500 nm. This is smaller than the
diffraction limit of the optical system and, therefore, the dimensions of the fibre cannot
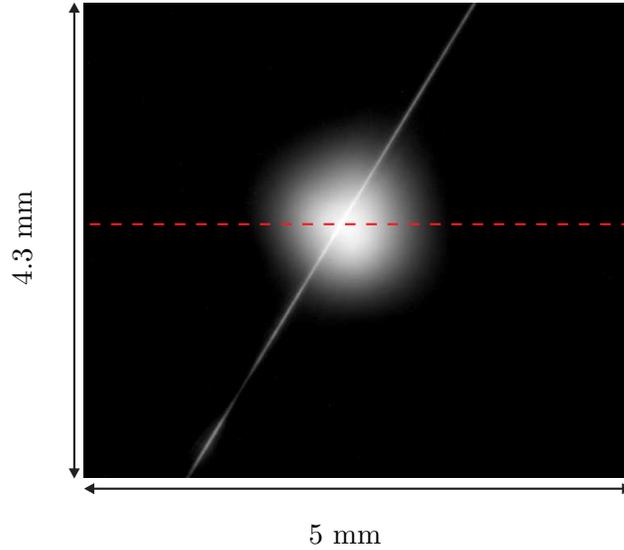be resolved.

4.3 mm

5 mm

FIGURE 3.10: Image of the Cs cloud trapped in a MOT in spatial overlap with the
500-nm diameter waist of a tapered optical fibre. The fluorescence of the atom cloud
during the normal operation of the MOT is detected with a CCD-camera. This picture
was taken using the new setup (see Figs. 5.9 and 5.10). The red dashed line indicates
the position of the axis considered in Fig. 3.11 to fit the profile of the cloud trapped in
the MOT.

Figure 3.11 shows a one-dimensional plot of the fluorescence of the cold atom cloud in
the MOT (black) as a function of the position along the axis denoted by the red dashed
line in Fig. 3.10. The size of the cloud can be determined by fitting the experimental
values to a one-dimensional Gaussian distribution (red) given by

$$G(x) = G_0 + \frac{A}{\sigma\sqrt{2\pi}} \exp\left[-\frac{x^2}{2\sigma^2}\right], \tag{3.1}$$

with $G_0 = -25 \pm 1$, $A = (4.1 \pm 0.1) \times 10^5$, and $\sigma = 0.59 \pm 0.01$. The non-vanishing
value of G_0 stems from the JPEG compression format used to save the picture. This is
a lossy compression format that retrieves the data that is not noticeable for the human
eye. The signal arising from the light scattered by the fibre has been indicated by an
arrow. The position of the fibre is 80 μm displaced from the centre of the cloud. The
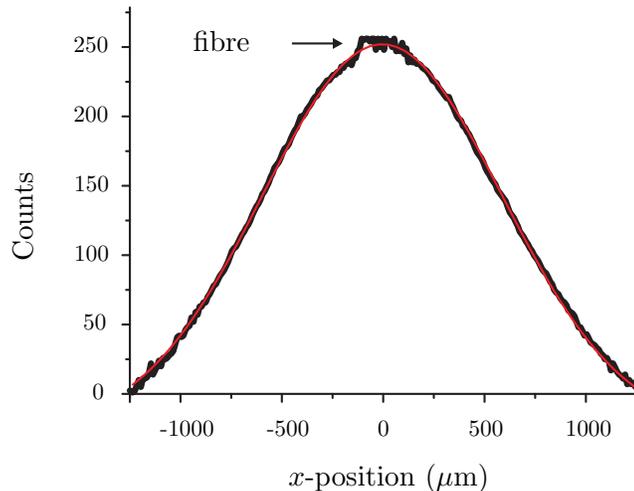
FIGURE 3.11: One-dimensional plot of the fluorescence of the cold atom cloud during the normal operation of the MOT as a function of the position along the x-axis (black) denoted by the red dashed line in Fig. 3.10. The red curve is a Gaussian fit of the experimental values. The point $x = 0$ has been set to coincide with the centre of the gaussian fit. The arrow denotes the position of the fibre.

cloud of cold atoms in the MOT of the original setup was measured to have about the same size.

3.4   Tools for atom detection

Probe laser

The atoms are probed with a diode laser in Littrow configuration ((3) in Fig. 3.1) which is frequency scanned by ± 24 MHz with respect to the $6^2 S_{1/2}$, $F = 4 \to 6^2 P_{3/2}$, $F' = 5$ transition using an AOM ((8) in Fig. 3.1) (Crystal Technologies, 3110-120): The laser is frequency stabilised using a polarisation spectroscopy setup ((21) in Fig. 3.1) to the crossover signal of the $F = 4 \to F' = 3$ and the $F = 4 \to F' = 5$ transition. Thus, the laser frequency is locked about 225 MHz below the transition to be probed. An acousto-optical modulator (AOM) in double pass configuration allows to shift upwards the frequency of the probe laser by the same amount. The AOM is operated using a voltage controlled oscillator (VCO). Using an RF-spectrum analyser the frequency output of the VCO can be monitored during the measurements. Moreover, the voltage dependence of the frequency output of the VCO was measured to be almost linear in the range of interest. The emission linewidth of the laser was experimentally determined to be 1 MHz with an integration time of 10 ms through a frequency beating measurement with another laser with a well known linewidth. This allows to resolve

the $\gamma/2\pi$ =5.22 MHz natural absorption linewidth of the Cs D$_2$-line in Doppler-free spectroscopy.[3] The polarisation of the laser at the fibre input is linear. However, since the TOF is not polarisation-maintaining, the polarisation at the fibre waist is unknown. Therefore, an incoherent, equally weighted mixture of linearly and circularly polarised light is assumed, leading to a saturation intensity for the Cs D$_2$-line in free-space of 18 W/m^2.

In the new setup a laser diode in Littman configuration [72] (Sacher, SYS-500-850-20) with a maximal output power of 20 mW is used ((3) in Fig. 5.9). The laser has a specified emission linewidth narrower than 1 MHz with an integration time of 10 ms.

Avalanche photodiode (APD)

An FC connectorised APD (PerkinElmer, C30902E) is used to detect the transmission through the TOF. The APD signal is then recorded with a digital storage oscilloscope and averaged over 4096 traces. The APD uses an amplification circuit, which allows to detect powers of few pW in a single shot [71]. Averaging the signal over several thousand traces further allows measurements down to few fW. This large amplification limits the maximal power that can be detected to several hundred nW and the bandwidth of detection to 5 kHz, i. e., signals varying at larger frequencies cannot be efficiently detected. Therefore, an additional switching circuit was built to decrease the magnification by a factor of 100, 10 or 1.

The FC connectorised APD can also be used to detect a free-propagating beam. A convex lens focusing the beam into the light-pipe attached to the chip suffices for this purpouse. This is, e. g., the case for the new setup (Fig. 5.9). Moreover, depending on the use the convex lens is sometimes not necessary. This is the case for the beam used in the free-beam spectroscopy presented in Sec. 3.6.4.

3.5   Experimental sequence

Figure 3.12 conceptually describes the experimental scenario. A cloud of laser-cooled Cs atoms in a MOT is spatially overlapped with the waist of a TOF in UHV environment using the methods described in Sec. 3.3. The evanescent field spectroscopy is performed with the probe laser launched through the fibre and the transmission is measured with the APD described above. The TOF used for this experiment (Newport F-SF) was designed to have a waist diameter of 500 nm and yielded a transmission of 93% after the tapering. As explained in Sec. 1.3.2, the transmission is calculated by considering the power transmitted through the fibre before and after the tapering. During the evacuation of the chamber the transmission dropped to 40% possibly due to contamination with oil

---

[3]The convolution of two gaussian distributions leads to another gaussian distribution with a linewidth $\sigma = \sqrt{\sigma_1^2 + \sigma_2^2}$.

from the pre-vacuum pump.[4] After a few days in UHV environment the transmission increased and stabilised at 80%. The TOF fulfills the single mode condition at 852 nm wavelength given by Eq. (1.15), and the laser is therefore guided in the fundamental HE_{11} mode (see Sec. 1.2.1).
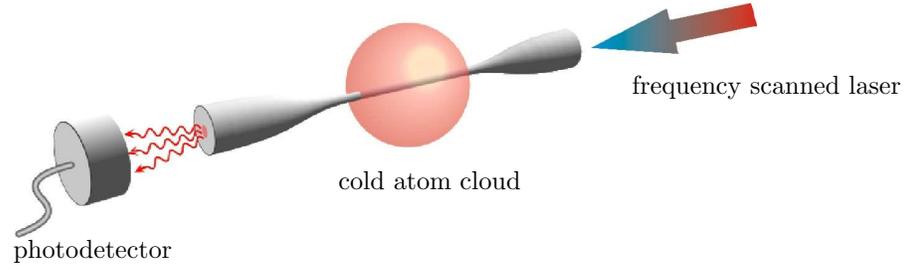

FIGURE 3.12: Conceptual description of the experimental scenario. A cloud of laser cooled atoms is spatially overlapped with a 500-nm diameter waist of a TOF. The transmission of a frequency scanned laser through the fibre is measured using a photodetector.

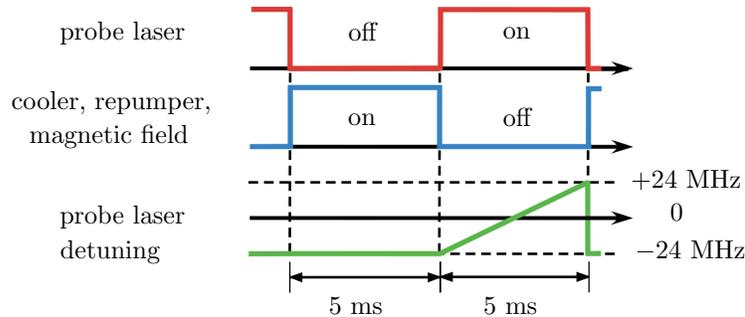### 3.5.1   Timing sequence of the experiment

FIGURE 3.13: Timing sequence of the experiment.

The timing of the experimental sequence is shown in Fig. 3.13: During the first 5 ms the atoms are captured and cooled in the MOT while the probe laser is off. In the following 5 ms the cooling and repump lasers and the magnetic field are switched off and the probe laser is on. Thus, the atoms are not influenced by the MOT lasers or the magnetic field. The cooling and repump lasers are shuttered using a chopper wheel that delivers a trigger signal for the rest of the elements involved in the sequence. The probe laser is switched and scanned using an AOM as described in Sec. 3.4. The duration of the two stages of the sequence does not need to be equal or fixed at 5 ms. The lower limit of the

---

[4]For this reason the pre-vacuum pump was substituted by the oil-free pump in the new setup.

probe laser pulse duration is given by the bandwidth of the APD in combination with the amplitude of the frequency scan: The time modulation of the absorption of the cold atom cloud should be slower than the rise time of the APD (5 kHz → 0.2 ms). Hence, the scan of the linewidth of the absorption of the atoms $\gamma/2\pi =$ 5.22 MHz should not be performed in less than 0.2 ms. If the amplitude of the scan is set to 50 MHz, the time needed is at least 2 ms. On the other hand, the upper limit of the probe pulse duration is given by the characteristic time-of-flight of the atoms released from the MOT, which has been measured to be approximately 8 ms (see Sec. 3.6.3). The cooling time can be as long as desired but not shorter than the time needed to re-capture the atoms that have been previously released. For a free-fall time of 5 ms, the re-capture time is shorter than the rise time of the APD. The magnetic field gradient is switched off using a field-effect transistor (FET) synchronised to the trigger signal of the chopper wheel. The $1/e$-decay time of the magnetic field gradient after the switching off the current applied on the magnetic coils has been measured to be 1 ms (see Sec. 3.3). The switching is required since the presence of the magnetic field gradient used for the normal operation of the MOT would lead to a broadening of the measured absorbance profiles of the cold atom cloud of about 1 MHz (see Sec. 3.6.4).

3.6 Experimental results

Figure 3.14 shows the measured APD signal in AC mode as a function of time using the experimental sequence shown in Fig. 3.13. The reference signal in absence of the cold atom cloud (black dashed) is obtained by running the molasses normally but without magnetic field. The central part of the measured signal from $t = 0$ to $t = 4.5$ ms corresponds to the transmission of the frequency scanned probe laser through the fibre. The shape of the laser pulse is determined by the efficiency of the AOM. The increased background signal measured at $t < 0$ and at $t > 5$ ms results from the coupling of the MOT beams to the guided fibre mode HE_{11}. This stems from the scattering of the beams at the surface of the fibre. The reference at zero power is measured by introducing a small time delay of about 0.5 ms between the two periods of the sequence where both the MOT lasers and the probe laser are switched off. The red solid curve shows the APD signal when cold atoms are trapped and cooled in the MOT and subsequently released. The transmission decreases by 23% when the frequency of the probe laser matches the resonance frequency of the atoms. Note that the measured signal at $t < 0$ and at $t > 5$ ms is larger when the atoms are present. This effect is due to the fluorescence of the atoms coupled to the guided fibre mode at the waist (see Chap. 4).

3.6.1 Data analysis

The measurement shown in Fig. 3.14 allows to extract information about the interaction of the atoms with the evanescent field propagating in the HE_{11} mode at the waist of the fibre. The atomic absorption leads to an attenuation of the transmission of the probe
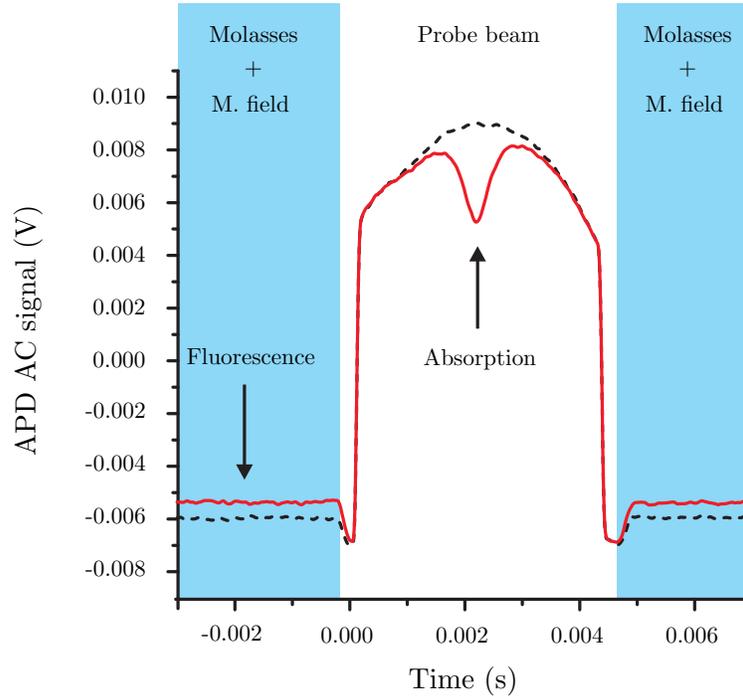
FIGURE 3.14: Measured APD signal in AC mode as a function of time: In the presence of the laser cooled atoms (red solid) and in their absence (black dashed). The used experimental sequence is shown in Fig. 3.13. The peak probe laser power was set to 11 pW.

laser through the fibre according to Beer's law. The transmitted power P is, therefore, given by

$$P = P_0 e^{-A(\delta)}, \tag{3.2}$$

where P_0 is the power transmitted through the fibre in absence of the atom cloud and δ is defined as

$$\delta = (\omega - \omega_0), \tag{3.3}$$

where ω is the angular frequency of the probe laser and ω_0 is the angular frequency of the atomic transition. The absorbance $A(\delta)$ is calculated as

$$A(\delta) = -\ln[P/P_0]. \tag{3.4}$$

$A(\delta)$ can thus be directly extracted from the data in Fig. 3.14 once the time axis has been converted to a frequency axis according to the calibration described in Sec. 3.4.
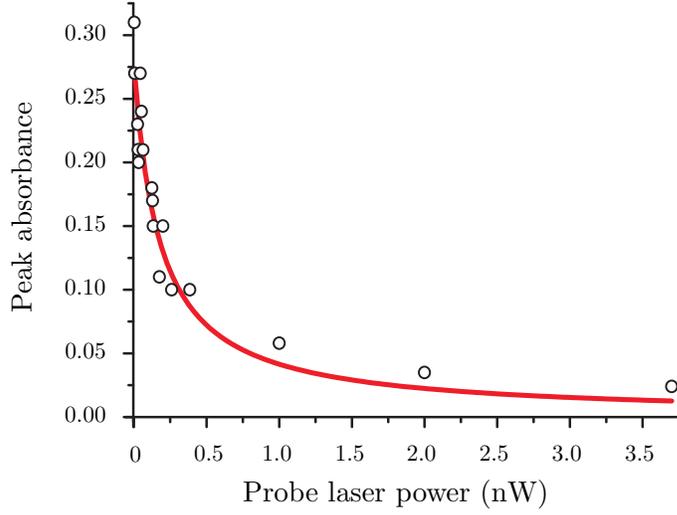
FIGURE 3.15: Peak absorbance of the atom cloud (circles) and fitted theoretical function (red solid) as a function of the probe laser power.

3.6.2   Absorbance on resonance as a function of the probe power

The peak absorbance of the cold atom cloud varies as a function of the power of the probe laser due to the saturation of the probed atoms (see Sec. 2.2). Using Eq. (3.4) the power dependency of the absorbance on resonance $A(\delta = 0)$ can be approximated as

$$A(\delta = 0) = -\ln\left[1 - \frac{A_0}{1 + s_P P_0}\right] \simeq \frac{A_0}{1 + s_P P_0}, \tag{3.5}$$

where A_0 is the absorbance on resonance for vanishing powers and P_0 is the power of the probe laser. The quantity $s_P P_0$ is the mean saturation parameter of the atoms in the cloud: Since the atoms are at different distances from the fibre surface, the saturation parameter of each individual atom is different. The approximation in Eq. (3.5) is justified by the experimental values shown in Fig. 3.15, where A_0 has a value of 0.31. Here, the peak absorbance of the atom cloud (circles) obtained in a set of measurements like the one shown in Fig. 3.14 is plotted as a function of the probe laser power. By fitting the experimental values with the theoretical curve (red solid) given by Eq. (3.5) the following values of the parameters A_0 and s_P are obtained:

$$A_0 \;=\; 0.28 \pm 0.01, \tag{3.6}$$
$$s_P \;=\; (0.006 \pm 0.001) \ \mathrm{pW}^{-1}. \tag{3.7}$$

Using the fitted value of s_P, we can estimate that for a probe laser of 170 pW the mean saturation parameter is equal to 1.

3.6.3 Time-of-flight measurements of the cold atom cloud using a TOF

By releasing the atoms from the MOT and by measuring the absorption of the probe laser after a variable time of flight, the temperature of the atoms can be estimated. Using the experimental sequence shown in Fig. 3.13 a delay between the cooling and probing cycles is introduced where all lasers and the magnetic field are switched off. Figure 3.16 shows the peak absorption of the atom cloud as a function of the delay
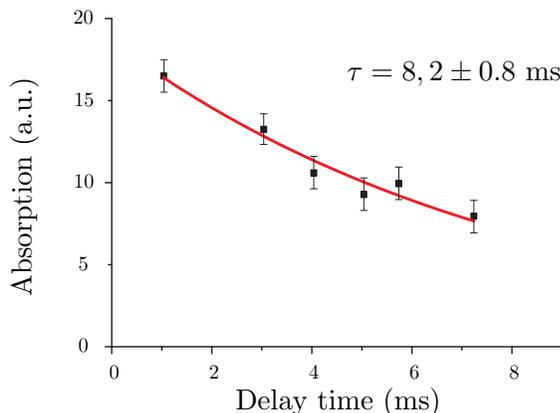

FIGURE 3.16: Transmission of the probe beam through the tapered optical fibre on resonance (squares) and fitted exponential decay (red solid) as a function of the delay time between the cooling and probing cycles. This measurement was performed with the new setup (Fig. 5.9).

between the cooling and probing cycles. The $1/e$-decay time of the density of the atom cloud at the position of the fibre is found to be 8.2 ± 0.8 ms. We can estimate that the density variation of the cold atom cloud during the probing time of 5 ms is about 40% of its peak value. Comparing the experimental results with the theory of a ballistically expanding atom cloud in the presence of gravity, the temperature of the atoms in the MOT can be determined. Following the notation introduced in Fig. 1.5, the z-axis is set parallel to the fibre axis. Since the waist of the TOF is longer than the extension of the size of the cloud along the fibre axis a 2D-distribution in the xy-plane can be used to describe the density of the cloud. The distribution of the density of a cloud of atoms with temperature T during the fall is given by [73]

$$\rho(x, y, t) = \frac{1}{2\pi\sigma^2(t)} \exp\left[-\frac{(y^2(t) + x^2)}{2\sigma^2(t)} \right], \tag{3.8}$$

where

$$y(t) = y + \frac{1}{2}gt^2 \tag{3.9}$$

determines the time evolution due to gravity and

$$\sigma(t) = \sqrt{\sigma_0^2 + (k_B T/m_{Cs})t^2} \tag{3.10}$$
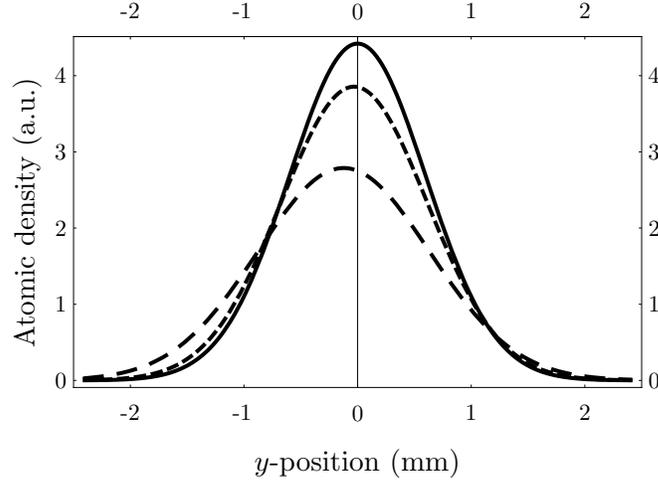
FIGURE 3.17: Calculated density distribution of the atom cloud with a temperature of 135 μK as a function of the position on the y-axis at $x = 0$ at three different times: $t = 0$ (solid), $t = 2.5$ ms (short-dashed), and $t = 5$ ms (long-dashed).

determines the expansion of the cloud due to its temperature T. I determine the temperature of the atom cloud by searching T such that

$$\rho(x = 0, y = 0, t = \tau, T) = \frac{1}{e}\rho(x = 0, y = 0, t = 0, T) \qquad (3.11)$$

is fulfilled where τ is the $1/e$-decay time of the absorption measured in Fig. 3.16. This yields a temperature of $T = 135$ μK. Note that this must be taken as an estimation since Eq. (3.8) is not an exponential of the form $\rho(t) = A\exp[-t/\tau]$ at $x = y = 0$. Figure 3.17 shows the time evolution of the 2D-distribution of the density of the atom cloud given by Eq. (3.8) with $T = 135$ μK as a function of the position on the y-axis at $x = 0$. The solid curve is the density distribution at $t = 0$. The short-dashed curve is the density distribution at $t = 2.5$ ms, the typical time value when the probe laser is tuned to the resonance of the atom cloud according to the timing of the experiment shown in Fig. 3.13. Finally, the long-dashed curve is the density distribution at the end of the probe cycle, typically at $t = 5$ ms.

3.6.4   Frequency-dependent absorbance of the cold atom cloud

The absorbance of the cold atom cloud $A(\delta)$ as a function of the detuning of the probe laser is shown in Fig. 3.18 (black). The zero point of the detuning has been fitted and is set to coincide with the peak value of the profile. The peak absorbance is found to be $A(\delta = 0) = 0.27$ which corresponds to an absorbed power of 2.6 pW for an incident power of 11 pW. The linewidth $W/2\pi$ of the absorbance profile is defined as the full
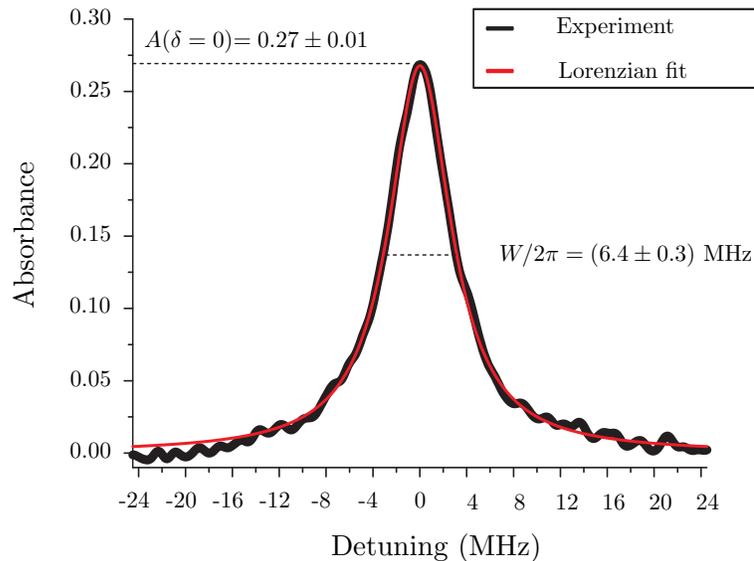
FIGURE 3.18: Absorbance of the cold atom cloud in the evanescent field around the fibre (black) as a function of the detuning of the probe laser with a power of 11 pW. The Lorentzian curve (red) given by Eq. (3.13) has been fitted to the experimental values using the method of the least-squares.

width at half maximum (FWHM)

$$A(\delta = W/2) = \frac{1}{2}A(\delta = 0), \tag{3.12}$$

which can be determined by fitting the measured absorbance profiles with the Lorentzian function

$$\mathrm{L}(\delta) = \frac{2C}{\pi} \frac{1/W}{1 + (2\delta/W)^2} \tag{3.13}$$

using the method of the least-squares with W and C as fitting parameters (red).

The agreement between the experimental and the fitted curves is very good except in the regime of $-24 < \delta/2\pi < -16$ MHz. This deviation stems from a slight asymmetry of the experimental curve, which could not be systematically reproduced. As a check, the laser was scanned from negative to positive detunings and viceversa and no correlations between the asymmetry and the direction of scan were observed.

Estimation of the error in the measurement of the linewidths

Systematic errors in the measurement of the widths can arise from the following sources:

- Laser linewidth: The measured absorbance profile is a convolution of the "real" absorbance profile with width W_0, and the laser line with width W_L. Hence, the

measured width W is given by $W \simeq \sqrt{W_0^2 + W_L^2}$. The experimentally measured linewidth of the laser $W_L/2\pi = 1$ MHz, leads a maximal overestimation of a 2% when approaching the natural linewidth of the Cs D_2-line $W_0/2\pi = 5.22$ MHz.

- Time of flight through the evanescent field: The interaction time of the atoms with the evanescent field depends on their mean velocity inside the MOT, $v_D \simeq 10$ cm/s, and on the decay length of the evanescent field in the HE_{11} mode given by Λ_{11} (see Sec. 1.2.1). The interaction time is thus on the order of 1 μs, leading to a frequency broadening of 1 MHz that produces a maximal overestimation of the linewidth W of 2%.

- Magnetic field gradient: The repetition of the same measurement with and without switching off the magnetic field gradient during the probe cycle, leads to a broadening of 1 MHz in the latter case. Hence, the magnetic field gradient needs to be switched off during the spectroscopy. Since it has a decay time of 1 ms after switching off, the broadening of the curves due to the residual magnetic field gradient can thus be neglected.

- Numerical fit: The error in the fitting performed applying Eq. (3.13) using the method of least squares is < 1%. However, modifications on the measured linewidth on the order of ±2% have been observed by repeatedly fitting the same curve while varying the fitting range in a few percent.

- Variations in the peak atomic density due to free expansion of the cold atom cloud: As shown in Fig. 3.16, the density decreases by 40% of its maximal value during the probing time, however, the time delay between the two points defining the width is of 2 ms. This leads to a decrease in the density of 20%, which produces an underestimation of the linewidth given by

$$\frac{\Delta W}{W} \simeq \frac{0.2}{W} \left| \frac{A(\delta)}{(dA/d\delta)} \right|_{\delta=W/2} = 0.04. \tag{3.14}$$

To estimate the statistical error, the measurements have been repeated under the same conditions several times, leading to a statistical deviation of $\Delta W/W = \pm 5\%$.

Free-beam spectroscopy of the cold atom cloud

To investigate if the experimental setup allows to resolve the natural linewidth of the Cs D_2-line, free beam spectroscopy on the cold atom cloud has been performed (see Fig. 3.1). For this purpose a Gaussian beam previously mode-filtered using a single-mode standard optical fibre is used. The beam has a peak intensity of $I = 2.9$ μW/m^2 and approximately the same cross-section as the atom cloud. The chosen value of the intensity $I \sim 10^{-7} I_s$ excludes any power broadening of the absorbance line of the atoms. Figure 3.19 shows the absorbance profile of the cold atom cloud (black) measured using
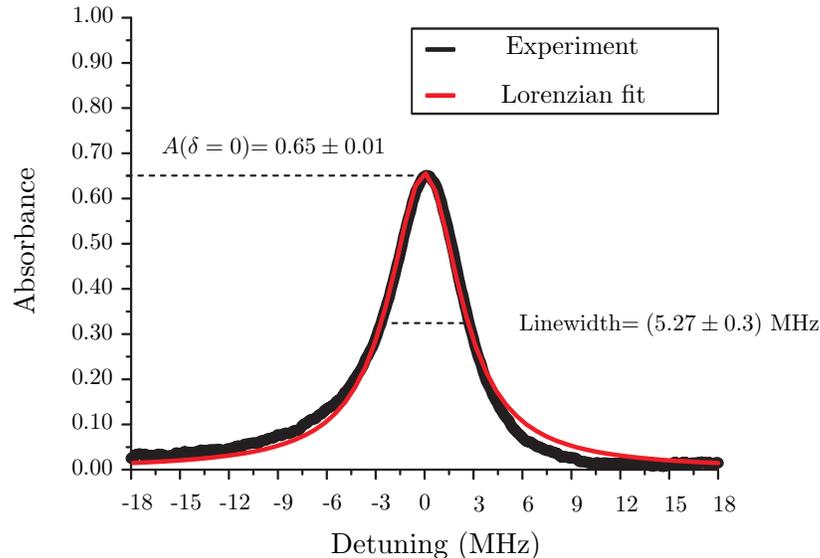
FIGURE 3.19: Absorbance profile of the cold atom cloud (black) as a function of the detuning of the probe laser. The spectroscopy was performed with a Gaussian beam of intensity $I = 2.9 \ \mu\text{W/m}^2$. The Lorentzian curve (red) given by Eq. (3.13) is a least square fit to the experimental values.

free-beam spectroscopy in a similar experimental sequence as in Fig. 3.13. The width of the curve has been calculated by fitting Eq. (3.13) (red) to the experimental values, leading to a measured linewidth of $W/2\pi = (5.27 \pm 0.3)$ MHz, which confirms that our detection setup can resolve the natural linewidth of the Cs atoms.

3.6.5 Linewidths vs incident power: Light-induced dipole forces and atom-surface interactions

According to Eq. (2.16) the linewidth of the absorbance profiles is a measure of the degree of saturation of the probed atoms. However, when the atoms interact with the evanescent field around an ultra-thin optical fibre the linewidth of the profiles is further modified by a number of additional effects that can be conveniently classified in two classes: Light-induced dipole forces and surface interactions.

The light-induced dipole forces arising from the interaction of a near-resonant light field with a neutral atom have been explained in Sec. 2.2. The frequency of the light field is scanned during the spectroscopy. Hence, in addition to the resonant absorption of the probe beam by the atoms the field also interacts with the atoms dispersively resulting in a dipole force that mechanically influences them. Moreover, the dipole force is proportional to the intensity gradient of the light field, which is very strong in the evanescent field due to the exponential decay of the intensity outside the fibre. This will

be shown in Sec. 3.7.3.

The surface interactions will be explained in Sec. 3.7.2. One atom located at the vicinity of the surface of a metal or dielectric will undergo a modification of the radiative properties and a shift of the atomic energy levels [20]. This can be intuitively understood as dipole-dipole interaction between the electric dipole of the atom and its image induced on the surface of a reflector.
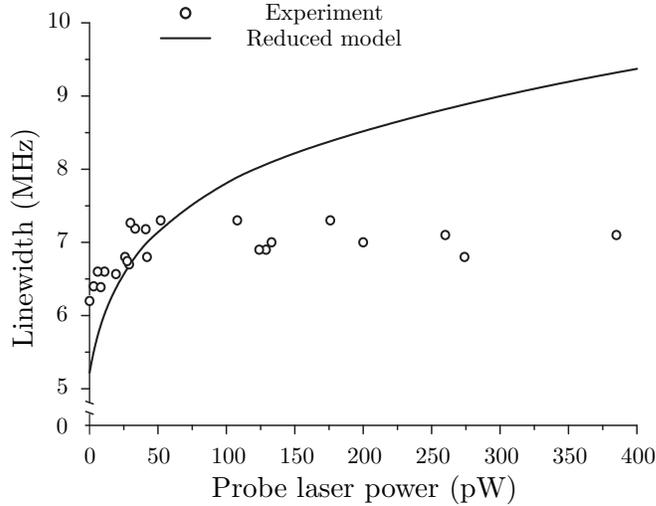

FIGURE 3.20: Linewidth of the measured absorbance profiles (circles) versus the probe laser power. The solid line is a theoretical model not taking into account light-induced dipole forces and surface interactions.

Figure 3.20 shows the linewidths of the absorbance profiles plotted as a function of the probe laser power (circles). The experimental values are obtained by repeating the measurement shown in Fig. 3.18 for different probe laser powers. For comparison, a theoretical model (solid) that calculates the laser linewidth in absence of light-induced dipole forces and surface interactions is shown. In the following, this will be referred to as the reduced model to distinguish it from the full model that will be presented in Sec. 3.7.

The disagreement between the experimental values and the reduced model points out the regimes where each of the above mentioned effects dominates: For probe laser powers larger than 50 pW the measured linewidths are considerably narrower than the predictions of the reduced model. The experimental values show significantly less power broadening. I will show in Sec. 3.8 that this narrowing can be explained by the effect of the light-induced dipole forces on the density of the atomic cloud. On the other hand, the linewidths measured for probe laser powers smaller than 50 pW are broader than the predictions of the reduced model. This can be better appreciated in Fig. 3.21 where the widths in the regime of low powers of the probe laser are shown. While the reduced model approaches the natural linewidth of the D$_2$-line of Cs of $\gamma/2\pi = 5.22$ MHz for
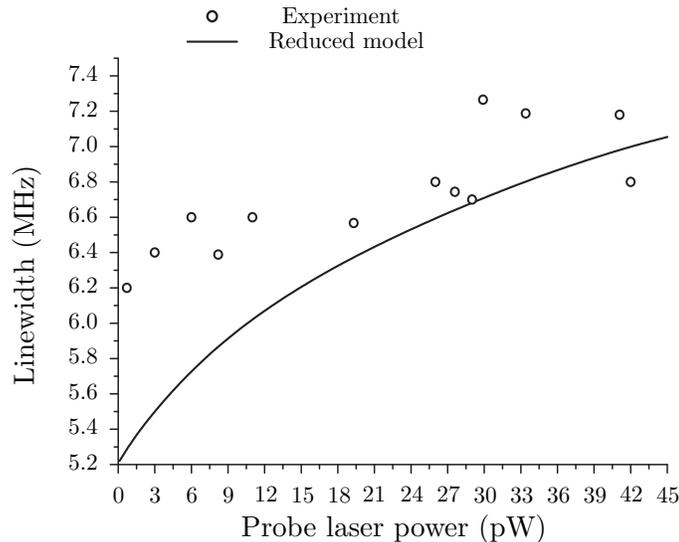
FIGURE 3.21: Linewidth of the measured absorbance profiles (circles) against the probe laser power for low laser powers. The solid line indicates the reduced model not taking into account light-induced dipole forces and surface interactions.

vanishing powers, the experimental values approach a linewidth of 6.2 MHz, i. e., about 20% broader. As we will see in Sec. 3.8, this can be explained by means of atom-surface interactions that modify the spectral properties of the atoms near the fibre.

3.7 Model for near-resonant interaction of cold atoms with the evanescent field of a TOF

3.7.1 Reduced model

In the following, I will first introduce the reduced model that was used to generate the theoretical curves in Figs. 3.20 and 3.21.

The variation of the intensity I of a laser beam passing through an absorbing medium along the z-axis is given by [4]

$$dI = I\sigma_s\rho dz, \tag{3.15}$$

where ρ is the density of scatterers in the medium and σ_s the individual scattering cross section. For the case of a cloud of atoms, Eq. (3.15) reads

$$dI = \hbar\omega\frac{\gamma}{2}\frac{I/I_s}{1 + I/I_s + (2\delta/\gamma)^2}\rho dz. \tag{3.16}$$

I_s is the free-space saturation intensity of the atoms defined in Eq. (2.14), δ the angular frequency detuning defined in Eq. (3.3), ω the angular frequency of the laser, and γ the

spontaneous emission rate of the atoms. This equation can be approximated for the case of low optical densities as

$$dI(r,z) = \hbar\omega\frac{\gamma}{2}\frac{I_{P_0}(r)/I_s}{1 + I_{P_0}(r)/I_s + (2\delta/\gamma)^2}\rho dz, \tag{3.17}$$

where the magnitude $I_{P_0}(r)$ is the unmodified intensity of the laser beam and r denotes the radial position. The low optical density approximation assumes that the power incident in one atom is not influenced by the rest of the atoms in the cloud. This results in a linear dependence of the transmitted power on the extension of the cloud along the direction of propagation of the field. If the low optical density approximation was not used, this dependence would be exponential. This is justified because the maximal experimentally measured absorbance is $A(\delta = 0) \simeq 0.3$ for $P_0 \leq 3$ pW, leading to a maximal deviation of a 14% between Eqns. (3.17) and (3.16). Using Eq. (2.15), the line shape of the absorbance profiles can be expressed as

$$A(\delta, P_0) = \frac{\hbar\omega}{P_0}\int \rho(r,z)\Gamma_s(I_{P_0})dV, \tag{3.18}$$

where $\Gamma_s(I_{P_0})$ is the scattering rate of one atom and $\rho(r,z)$ is the atom density inside the MOT given by

$$\rho(r,z) = \left\{\frac{n_0}{\sigma^3(2\pi)^{3/2}}e^{-(r^2+z^2)/2\sigma^2}\right\}g(r). \tag{3.19}$$

The term in curly brackets corresponds to a Gaussian density distribution of an unperturbed atomic cloud with an experimentally measured $1/\sqrt{e}$-radius of $\sigma = 0.6$ mm and a total atom number n_0. Note that the latter is not relevant to simulate the linewidths which are independent of n_0. The factor $g(r)$ accounts for the perturbation of the density introduced by the fibre at distances close to the surface.

Figure. 3.22 shows a schematic of the influence of the fibre in the density of the atom cloud at distances close to the surface. The black arrows denote classical atomic trajectories that cross a point at a radial position r. The density of atoms at this point is thus proportional to the number of atomic trajectories that cross it. The red arrows show one example of atomic trajectory that collides with the fibre. Upon collision with the fibre surface, the atoms are either adsorbed [74] or rapidly expelled with a kinetic energy of $E_k/k_B = 300$ K and do not contribute to the absorbance. The quantity $g = \alpha/2\pi$ therefore determines the amount of shadowing produced by the fibre. Hence, the density of the atom cloud at a distance r from a cylinder with radius a is modified by a factor $g(r)$. Due to the geometry of the system, $g(r)$ can be approximated as

$$g(r) = 1 - \frac{1}{\pi}\arcsin(a/r), \tag{3.20}$$

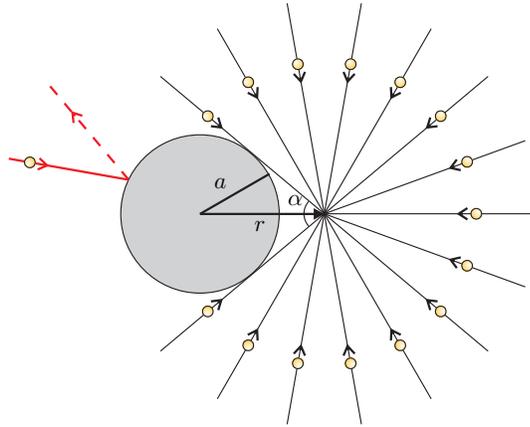which, leads to $g(r = a) = 1/2$ at the fibre surface.

FIGURE 3.22: Schematic of the influence of a fibre with radius a on the density of the cold atom cloud near the surface. The black arrows denote the classical atomic trajectories that contribute to the density at the radial position r. The red arrow shows one example of the trajectory of an atom colliding with the fibre surface. The atom is subsequently expelled with a kinetic energy of $E_k/k_B = 300$ K (dashed line).

3.7.2 Surface interactions between a neutral atom and a dielectric fibre

A simple physical picture of the interaction of atoms with a dielectric body relies on the dipole-dipole interaction between the electric dipole moment of the atom $\vec{d}$ and the image dipole induced on the bulk material. Although for a neutral atom the permanent electric dipole is zero, $\langle \vec{d}(t) \rangle = 0$, its quantum fluctuations are non-zero ($\sim \langle \vec{d^2} \rangle \neq 0$). This leads to correlated fluctuations of the image dipole that interact with the original dipole. As a result, an attractive potential with a position dependence proportional to $(r-a)^{-3}$ arises in the near-field approximation (i. e., instantaneous image): The van der Waals potential. In the far-field regime an additional factor $(r-a)^{-1}$ appears, leading to the Casimir-Polder potential. This classical picture is valid for an atom in the ground state, but fails to describe the behaviour of an excited atom. In this case the radiative properties associated to the spontaneous emission of the atom must be considered. Firstly, the dipole fluctuations of an atom in an excited state are larger than those in the ground state. This can be intuitively understood assuming one electron orbiting around the atom. The bigger the radius of the orbit is, the larger $\langle \vec{d^2} \rangle$ will be. This leads to a red-shift of the atomic transition frequency because the excited level of the atom experiences a larger van der Waals potential than the ground state. Another effect arising from the presence of the dielectric body is a modified lifetime of the excited state of the atom, i. e., a modified spontaneous emission rate. Each of the modes of the electro-magnetic field in which the radiation can be emitted (e. g., the guided mode of an ultra-thin optical fibre) contributes to the spontaneous emission. Hence, a full description of the radiation requires a weighted integration over all the possible modes available for the atomic emission with their correspondent coupling strength. Since the

fibre modifies the density of modes, the atomic spontaneous emission rate is, thereby, modified.

Van der Waals interaction

The classical van der Waals potential of an atom near the surface of a dielectric cylinder of infinite length is given by [56]

$$V_{\text{vdW}}(r) = \frac{\hbar}{2\pi^3 \varepsilon_0} \sum_{l=-\infty}^{\infty} \int_0^{\infty} \left(k^2 K_l'^2(kr) + (k^2 + l^2/r^2) K_l^2(kr) \right) \times \qquad (3.21)$$

$$\times \left(\int_0^{\infty} \alpha(i\xi) G_l(i\xi) d\xi \right) dk, \qquad (3.22)$$

where

$$G_l(\omega) = \frac{(\varepsilon(\omega) - \varepsilon_0) I_l(ka) I_l'(ka)}{\varepsilon_0 I_l(ka) K_l'(ka) - \varepsilon(\omega) I_l'(ka) K_l(ka)}. \qquad (3.23)$$

ε_0 is the dielectric constant in vacuum, k the wave-number in vacuum, $I_l(x)$ the modified Bessel function of first kind, $K_l(x)$ the modified Bessel function of second kind and $I_l'(x)$ $(K_l'(x))$ denotes $dI_l(x)/dx$ $(dK_l(x)/dx)$. The frequency-dependent dielectric function of silica $\varepsilon(\omega)$ is given by [43]

$$n^2(\omega) = \frac{\varepsilon(\omega)}{\varepsilon_0} = 1 + \frac{0.6961663 \, \lambda^2}{\lambda^2 - 0.0684043^2} + \frac{0.4079426 \, \lambda^2}{\lambda^2 - 0.1162414^2} + \frac{0.8974794 \, \lambda^2}{\lambda^2 - 9.896161^2}, \qquad (3.24)$$

where λ is in units of micrometers. The multilevel structure of the atom is taken into account by using $\alpha(\omega) \simeq \text{Re}[\alpha(\omega)]$ given by Eq. (2.27). Note that this approximation neglects the resonant frequencies of the silica. This is justified because they are substantially different and weaker than those of the atom. When calculating $\text{Re}[\alpha(\omega)]$ for the excited state, the downward transition back to the ground state must also be included. Note that this calculation does not take into account the hyperfine structure of the atom and, therefore, it is only valid for quantum states with low orbital angular momentum like S and P. For the case of silica, the frequency dependence of $\varepsilon(\omega)$ can be neglected because its variation over the range defined by the strongest transitions of Cs (visible to infrared) is smaller than 3%. The validity of the approximations can be checked by calculating the well-known coefficient of the v.d.W. potential of a ground-state Cs atom near an infinite planar silica surface $C_3 = 5.6 \times 10^{-49}$ J m^3 given by [39]

$$C_3 = \frac{\hbar}{16\pi^2 \varepsilon_0} \int_0^{\infty} \alpha(i\xi) \frac{\varepsilon(i\xi) - \varepsilon_0}{\varepsilon_0 + \varepsilon(i\xi)} d\xi. \qquad (3.25)$$

Using an average value of $\varepsilon/\varepsilon_0 = (1.43)^2$, a deviation of less than 1% is obtained for the C_3 coefficient. Moreover, the used approximations lead to a ratio between the two

integrated polarisabilities of the ground and excited states of 1.94, in accordance with
the experimental value of [75]

$$\frac{C_3(6^2P_{3/2})}{C_3(6^2S_{1/2})} \simeq 2. \tag{3.26}$$
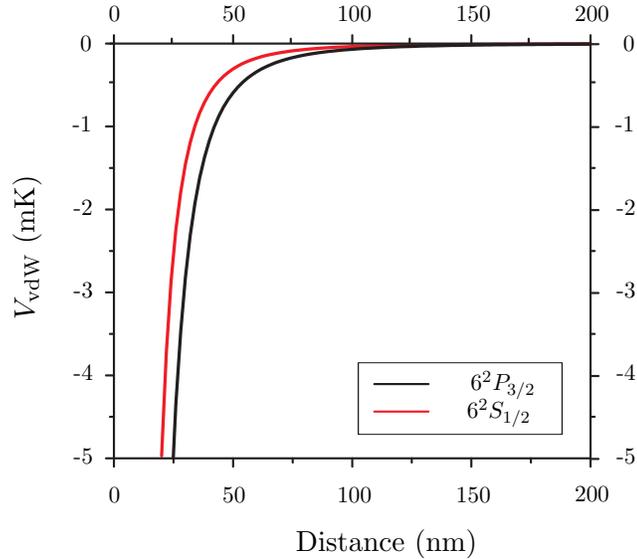

FIGURE 3.23: Van der Waals potential between a dielectric fibre and a Cs atom in the
$6^2S_{1/2}$ (red) and $6^2P_{3/2}$ (black) states as a function of the distance to the fibre surface.
The calculations have been performed for a cylindrical fibre with radius $a = 250$ nm
and a frequency-independent refractive index of $n = 1.43$.

Figure 3.23 shows the variation of the Van der Waals potential between a dielectric
cylinder of infinite length and a Cs atom in the $6^2S_{1/2}$ (red) and $6^2P_{3/2}$ (black) states
versus the distance to the fibre surface. Due to the larger polarisability of the excited
state, the energy shift of the $6^2P_{3/2}$ state is larger than the one of the $6^2S_{1/2}$ state. As
a result, the transition frequency between these two states is shifted by

$$\frac{\Delta\mathcal{E}}{h} = \frac{1}{h}\left(V_{6^2P_{3/2}} - V_{6^2S_{1/2}}\right). \tag{3.27}$$

The frequency shift $\Delta\mathcal{E}/h$ of the $6^2S_{1/2} \rightarrow 6^2P_{3/2}$ transition is plotted versus the atom-
surface distance in Fig. 3.24. Note that in the experiment the probe laser was scanned
from -24 to +24 MHz, which implies that atoms closer than 30 nm to the fibre surface
will not contribute to the observed spectrum (see Sec. 3.5.1).

• **Infinite planar surface approximation:**

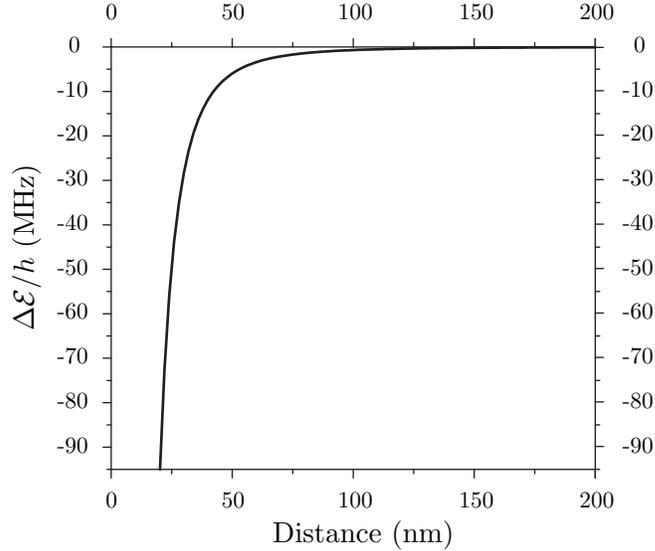This useful analytical solution of the v.d.W. potential is obtained when approximating

FIGURE 3.24: Frequency shift of the $6^2S_{1/2} \to 6^2P_{3/2}$ transition versus the distance from the fibre surface. The calculations have been performed for a cylindrical fibre with radius $a = 250$ nm and a frequency-independent refractive index of $n = 1.43$.

the cylinder as an infinite planar surface. The potential is then given by

$$V_{\text{planar}} = -\frac{C_3}{d^3}, \tag{3.28}$$

where d denotes the distance between the atom an the surface and the coefficient C_3 is given by Eq. (3.25). The C_3 coefficients for several dielectric bulk materials and different transitions of the Cs atom have been measured in a number of experiments [76, 77]. Figure 3.25 shows the ratio between the v.d.W. potential induced by a silica fibre and by an infinite planar silica surface plotted against the distance from the surface. The calculations have been performed for a Cs atom in the ground state and two different values of the fibre radius: 250 nm (solid), and 400 nm (dashed). As expected, the ratio $V_{\text{fibre}}/V_{\text{planar}}$ approaches one at vanishing distances. Indeed, for distances smaller than 100 nm $V_{\text{fibre}}/V_{\text{planar}} > 0.9$. Hence, this approximation describes the potential induced by a fibre of 250 nm radius with an accuracy better than a 10% in the region where the v.d.W. shift is not negligible compared to the accuracy of the experimental measurements. As described in Sec. 3.6.4 the estimated accuracy of the measurements of the linewidth is $\pm 5\%$, i. e., about ± 0.3 MHz.

Casimir potential

The Casimir potential can be viewed as a retarded van der Waals potential due to the finite velocity of the virtual photons that transmit the interaction [27]. While the v.d.W.
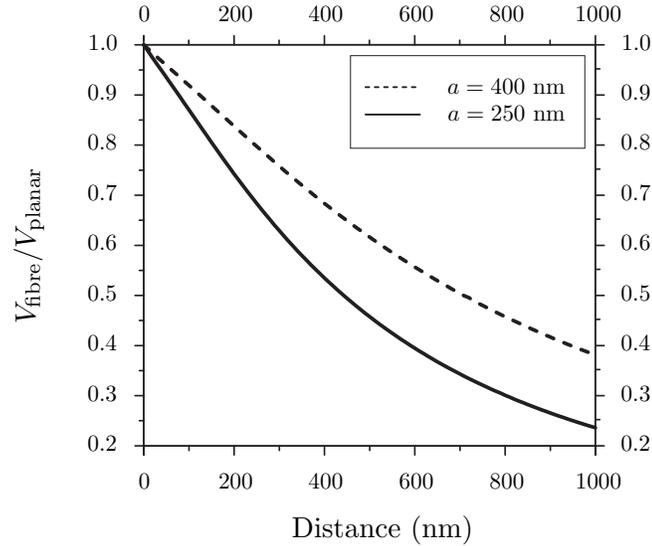
FIGURE 3.25: Ratio between the v.d.W. potential of a Cs atom near a dielectric fibre and the potential near an infinite planar silica surface versus the atom-surface distance. Solid: For a fibre radius of 250 nm. Dashed: For a fibre radius of 400 nm. The calculations have been performed for an atom in the $6^2S_{1/2}$ state.

potential (d^{-3}) is valid at distances d smaller than $\lambda/10$, the Casimir potential (d^{-4}) is valid asymptotically for large distances [20]. There is a smooth crossover between the two approximations at $d \simeq \lambda/10$ from the surface, which for Cs takes place at about 100 nm from the surface. The Casimir potential for a ground-state Cs atom near an infinite dielectric surface can be approximated as [78]

$$V_{\text{Cas}} = -\frac{3}{8\pi} \frac{\hbar c \alpha(0)}{4\pi\varepsilon_0 d^4} \frac{n^2 - 1}{n^2 + (30/23)n + 7/23}, \tag{3.29}$$

where $\alpha(0) = 399.9$ a.u. is the static polarisability of Cs [76]. Assuming a refractive index of $n = 1.43$ a Casimir interaction coefficient of $C_4 = 5.78 \times 10^{-56}$ J·m^4 is obtained, where $V_{\text{Cas}} = -C_4/d^4$.

Figure 3.26 shows a comparison between the variation of the Casimir (dashed) and v.d.W. (solid) potentials of a ground-state Cs atom near a planar infinite silica surface. The crossover between the two potentials takes place at a distance of $d \sim 100$ nm from the surface. At smaller (larger) distances, the v.d.W. (Casimir) approximation should be used, however, the deviations arising from the use of the v.d.W. potential at distances larger than 100 nm from the surface are rather small.

The Casimir potential of an atom in the excited state presents an oscillatory behaviour that can be approximated as $\cos[k \cdot d]$, where k is the wave-number associated to the considered radiative process [79]. In the simulations presented in Sec. 3.7.4 the v.d.W. shift of the $6^2S_{1/2} \to 6^2P_{3/2}$ transition frequency given by Eq. (3.27) was used for the
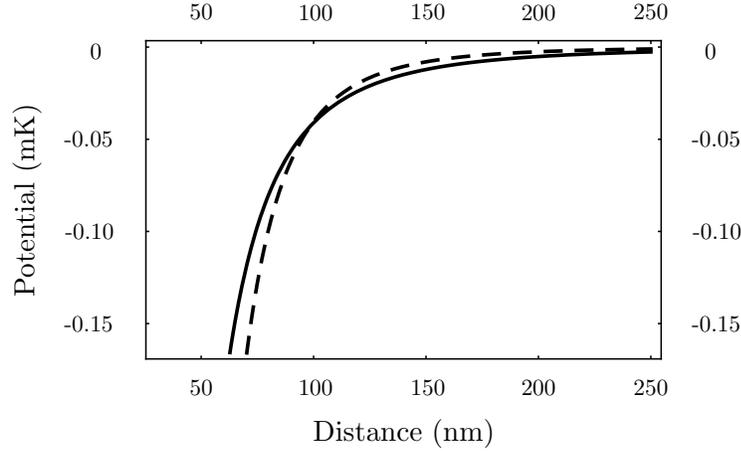
FIGURE 3.26: Variation of the Casimir (dashed) and van der Waals (solid) potentials of a ground-state Cs atom as a function of the distance from an infinite planar silica surface.

whole range of distances from the surface and this oscillatory behaviour was thus not taken into account. This is justified because the deviations produced by this approximation in the simulations are negligible compared to the accuracy of the experimental measurements.

In the case of the surface traps presented in Chap. 5, the use of the v.d.W. potential for the whole range of distances is always a conservative estimation of the surface potential. Therefore, only the non-retarded van der Waals interaction will be considered in this work.

Modifications of the spontaneous emission rate

The full quantum mechanical calculation of the modified spontaneous emission rate of Cs atoms near the surface of an ultra-thin optical fibre is laborious and can be found in [38]. In this section, an approximative solution of the problem based on classical calculations, which do not include the magnetic structure of the atom is presented. The spontaneous emission rate of an atom near an ultra-thin optical fibre has two contributions: The emission into radiating modes, i. e., modes propagating in free-space, and the emission into guided modes (the HE_{11} in the case of a single mode fibre). A third contribution due to non-radiative decay is neglected because silica has a negligible absorption at 852 nm. Hence, the total spontaneous emission rate is given by

$$\gamma_{\text{total}}(r) = \gamma_{\text{rad}}(r) + \gamma_{\text{guided}}(r). \tag{3.30}$$

Using a quasistatic approximation ($ka \ll 1$), the contribution to $\gamma_{\text{rad}}(r)$ from the three

possible orientations of the dipole moment is given by [57]

$$\gamma_{\text{rad}}^{(r)}(r) \simeq \gamma_0 \left| 1 + \frac{n^2 - 1}{n^2 + 1} \frac{a^2}{r^2} \right|^2, \tag{3.31}$$

$$\gamma_{\text{rad}}^{(\phi)}(r) \simeq \gamma_0 \left| 1 - \frac{n^2 - 1}{n^2 + 1} \frac{a^2}{r^2} \right|^2, \tag{3.32}$$

$$\gamma_{\text{rad}}^{(z)}(r) \simeq \gamma_0, \tag{3.33}$$

where γ_0 is the spontaneous emission rate of the atom in free space. If the dipole moment has no preferred orientation, γ_{rad} is an equally weighted average of the three possible orientations. Note that the longitudinal component $\gamma_{\text{rad}}^{(z)}$ stays unmodified by the presence of the fibre. This is only the case in the quasistatic approximation where electrostatic reflection coefficients hold [80].

It has been shown that $\gamma_{\text{guided}}^{j}(r)$ with $j = \{r, \phi, z\}$ has the same radial dependency as the corresponding component of the evanescent field intensity around the fibre $|E_j(r)|^2$ [38]. Therefore, the total emission rate into guided modes can be approximated as

$$\gamma_{\text{guided}}(r) \simeq \gamma_a \gamma_0 \frac{|\vec{E}(r)|^2}{|\vec{E}(a)|^2}, \tag{3.34}$$

where the product $\gamma_a \gamma_0$ gives the decay rate into guided modes at the surface of the optical fibre. Approximative expressions of γ_a for $ka \ll 1$ can be found in [57]:

$$\gamma_a^{(r)} \simeq \left[\frac{48n^4}{(n^2 - 1)^2(ka)^6} \exp \left(-\frac{2}{(ka)^2} \frac{n^2 + 1}{n^2 - 1} + \frac{n^2 + 1}{4} - 2\theta \right) \right], \tag{3.35}$$

$$\gamma_a^{(\phi)} \simeq \left[\frac{48}{(n^2 - 1)^2(ka)^6} \exp \left(-\frac{2}{(ka)^2} \frac{n^2 + 1}{n^2 - 1} + \frac{n^2 + 1}{4} - 2\theta \right) \right], \tag{3.36}$$

$$\gamma_a^{(z)} \simeq \left[\frac{12}{(ka)^6} \exp \left(-\frac{2}{(ka)^2} \frac{n^2 + 1}{n^2 - 1} + \frac{n^2 + 1}{4} - 2\theta \right) \right], \tag{3.37}$$

where $\theta \simeq 0.577$ is the Euler's constant. The equations above are only valid for single mode fibres since only the contribution of the fundamental mode is taken into account. This classical quasistatic approximation leads to a 30% smaller value of γ_{rad} than the full quantum-mechanical calculation. The value of γ_{guided} is, on the other hand, only 7% smaller [38].

Figure 3.27 shows the ratios of the spontaneous emission rates $\gamma_{\text{total}}(r)/\gamma_0$ (solid), $\gamma_{\text{guided}}(r)/\gamma_0$ (dash-dot), and $\gamma_{\text{rad}}(r)/\gamma_0$ (dashed) as a function of the distance from the fibre surface. The largest contribution leading to an increase of the spontaneous emission rate corresponds to the emission into the HE_{11} mode.

While all the above calculations have been performed classically one should bear in mind that a full quantum mechanical description we are dealing with cavity quantum electrodynamics (CQED) effects. In this picture, the modified spontaneous emission stems from the modification of the vacuum modes, in particular due to the presence of the strongly confined guided HE_{11} mode.
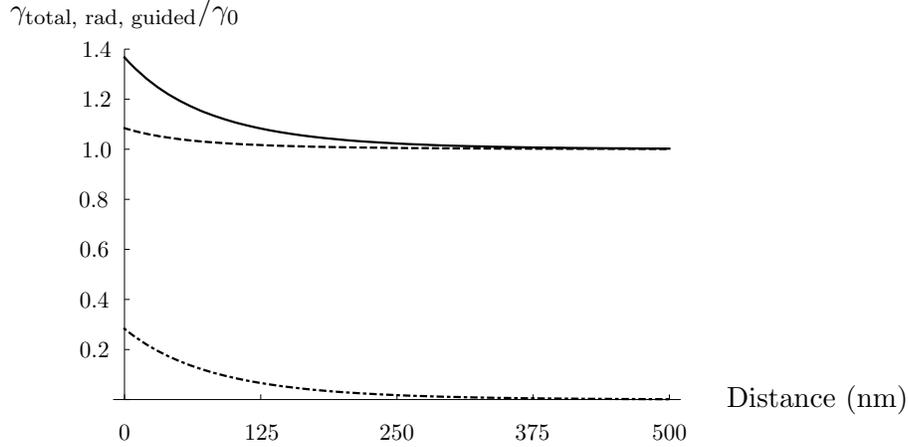
FIGURE 3.27:   Ratios of the spontaneous emission rates $\gamma_{\text{total}}(r)/\gamma_0$ (solid), $\gamma_{\text{guided}}(r)/\gamma_0$ (dash-dotted), and $\gamma_{\text{rad}}(r)/\gamma_0$ (dashed) as a function of the distance from the fibre surface. The calculations have been performed for a fibre of radius 250 nm with a refractive index $n = 1.45$.

3.7.3   Monte-Carlo simulations of the relative density of the atom cloud

Since the van der Waals interaction influences the atoms close to the fibre surface both spectrally and mechanically the influence of the fibre on the atomic density is not fully described by the geometrical factor $g(r)$ used to develop the reduced model. Furthermore, the strong radial confinement of the guided mode around the fibre leads to a large intensity gradient that induces dipole forces on the atoms in the presence of the probe laser. The dipole forces depend on the probe laser power P_0 and its detuning with respect to the atomic transition frequency. To describe the relative atomic density close to the fibre $f_{\delta,P_0}(r)$ during the spectroscopic measurements, Monte-Carlo simulations of classical atomic trajectories in the vicinity of the fibre including the above mentioned effects have been performed. For the v.d.W. interaction the full solution of the cylinder-atom problem has been used, however, the planar surface approximation has also been tested leading to the same results. We simulate 5.000 classical trajectories of thermal atoms inside the cloud. From the number of trajectories that cross a given volume element dV and from their velocity, a value for the relative density of atoms in the volume is inferred. Due to the geometry of the system the simulations can be reduced to a 2D problem. Each trajectory is obtained by numerically solving the 2D-equation of motion given by

$$m_{Cs}\ddot{\vec{r}} = \vec{F}_{\text{dip}}(r) + \vec{F}_{\text{vdW}}(r). \tag{3.38}$$

The first term on the right side denotes the near-resonant dipole force given by

$$\vec{F}_{\text{dip}}(r) = -\frac{\hbar}{2}\frac{\delta - \delta_{\text{vdW}}(r)}{1 + I(r)/I_s + (2(\delta - \delta_{\text{vdW}}(r))/\gamma)^2}\vec{\nabla}(I(r)/I_s), \tag{3.39}$$

where $I(r)$ is the intensity of the evanescent field in the HE_{11} mode with rotating polarisation given by Eqns. (1.20) and (2.13). Although the polarisation is unknown, for symmetry considerations the intensity distribution for the assumed isotropic polarisation is the same as for rotating polarisation. The quantity δ is defined in Eq. (3.3). The spectral effects of the v.d.W. potential are included as a position-dependent detuning of the resonant frequency of the atom $\delta_{vdW}(r) = \Delta\mathcal{E}_{vdW}/\hbar$, while the mechanical effects are included in the second term of the right side of Eq. (3.38), given by

$$\vec{F}_{vdW}(r) = -\vec{\nabla}V_{vdw}(r). \tag{3.40}$$

The value of the potential V_{vdW} of a ground-state atom is used for the calculations. The validity of this approximation will be discussed below.
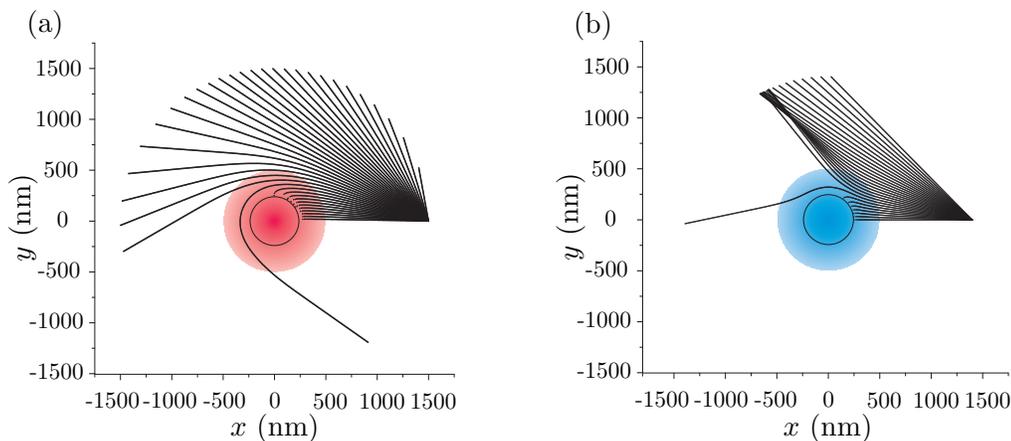
FIGURE 3.28: Simulated atomic trajectories for a probe laser power of 1 nW propagating in the HE_{11} mode of a 250-nm radius optical fibre with detunings $\delta/2\pi = -3$ MHz (a) and $\delta/2\pi = +3$ MHz (b). The atoms have a fixed velocity of 10 cm/s. The fibre is indicated by the circle and the extension of the evanescent field is schematically indicated by the shaded area.

Figures 3.28 (a) and (b) show several simulated atomic trajectories with a probe laser power of 1 nW and detunings -3 and $+3$ MHz, respectively. The modulus of the initial velocity of the atoms v_D is 10 cm/s, corresponding to the mean velocity of the thermal atoms at the Doppler temperature of the MOT $T_D = 125$ μK, and the angular distribution ranges from 0 to $\pi/2$ in (a) and from 0 to $\pi/4$ in (b). The atom source is located at $(1500, 0)$ nm, i. e., at a distance where both the light-induced dipole force and the v.d.W. interaction can safely be neglected. The trajectories in (a) are influenced by the red-detuned probe laser, and the atoms are accelerated towards the fibre. One could intuitively expect that some stable orbits appear. However, this is not possible at the given laser wavelength due to the bad cancellation between the centrifugal potential ($\sim 1/r^2$) and the dipole potential induced by the evanescent field [81]. The effect of the repulsive blue-detuned dipole force becomes apparent in (b). The atoms are repelled from the regions of higher intensity, however, at distances closer than 100 nm from the surface, the net force becomes attractive. This effect has two origins: Firstly, the v.d.W.

shift of the resonant frequency decreases the strength of the repulsive force. Secondly, the v.d.W. force is stronger than the light-induced dipole force at short distances.

The distribution of the modulus of the initial velocity v is determined by a 3D-Maxwell distribution projected to 2D:

$$p(v, T_D) = 4\pi \left(\frac{m_{Cs}}{2\pi k_B T_D}\right)^{3/2} v^2 \exp\left(-\frac{m_{Cs} v^2}{2 k_B T_D}\right). \tag{3.41}$$

The initial angle of the trajectory is then given by the oven distribution [82]

$$\theta = \arccos(\mathcal{R}), \tag{3.42}$$

where $\mathcal{R}$ denotes a function generating random numbers from 0 to 1. Note that for symmetry considerations is not necessary to move the starting point of the atomic trajectories along the azymuthal direction.
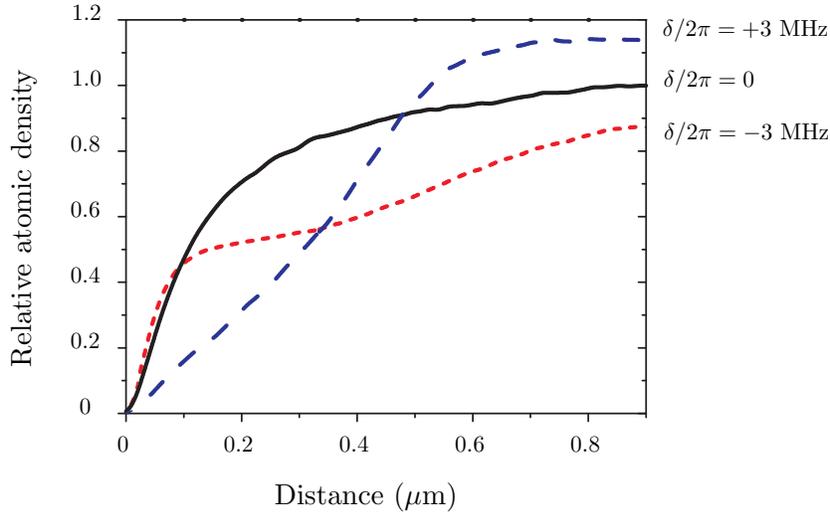
FIGURE 3.29: Simulations of the relative density of the cold atom cloud around an ultra-thin fibre for different detunings of the probe laser versus the distance from the fibre surface; solid line $\delta/2\pi = 0$, dotted line $\delta/2\pi = -3$ MHz, dashed line $\delta/2\pi = +3$ MHz. The following parameters have been used for the simulations: A fibre radius of 250 nm, a probe laser power of 1 nW and a 3D Maxwellian velocity distribution of Cs atoms at a temperature of 125 μK. For the simulation of this three curves 100.000 trajectories were used, which required an overall calculation time of 6 hours.

Figure 3.29 shows the relative atomic density $f_{\delta, P_0}(r)$ as a function of the distance from the fibre surface for $P_0 = 1$ nW and detunings $\delta/2\pi = -3$ (dotted), 0 (solid), and $+3$ MHz (dashed). $f_{\delta, P_0}(r)$ exhibits a strong frequency dependence. In all three cases the relative atomic density is zero at the surface of the fibre due to the v.d.W. force. The reason is that the atoms are strongly accelerated at distances closer to 100 nm from

the surface and, therefore, spend less time in a given volume element dV. Upon collision with the fibre surface, the atoms are either adsorbed or rapidly expelled with a kinetic energy of $E_k/k_B = 300$ K and do not contribute to the density anymore. The density has been normalised to its value at the starting position of the atomic trajectories for zero detuning of the probe laser. The relative density for positive detunings at large distances is larger than the one for zero detuning due to the contribution from repelled atoms. On the other hand, one would naively expect that the density near the fibre becomes larger for the case of negative detunings. This is not the case because the presence of a higher number of atoms is counteracted by a shorter average time of flight of the atoms through a given volume element due to their larger velocities. Indeed, the largest integrated density in the region of the evanescent field defined by $a < r < \Lambda_{11}$ is found for zero detuning. As a test, the simulations have also been performed in absence of v.d.W. interaction, leading to $f_{\delta=0,P_0}(r) = g(r)$, i. e., the geometric factor included in the reduced model (see Eq. (3.20)).

Effects neglected in the simulations

- Van der Waals potential of the excited state: V_{vdw} has been assumed to be the v.d.W. potential of a ground-state atom although the population of the excited state is not negligible during the spectroscopy measurements. In the limit of large saturation, the population is equally distributed between the ground and the excited states, leading to a 50% increase of the v.d.W. potential according to Eq. (3.26). However, the measured signal will not be notably modified by this effect because the mean distance of the probed atoms from the fibre surface also increases with increasing probe laser power (see Sec. 3.8).

- Vibrations of the fibre: The vibrations of the fibre are assumed to be slow compared to the mean velocity of the atoms $v_D = 10$ cm/s. Moreover, no vibrations of the fibre have been observed during the experiment, i. e., the amplitude of the vibrations is smaller than the resolution of the imaging system ~ 10 μm.

- Light-pressure: The movement of the atoms in the axial direction due to the light-pressure force during the interaction time t_D is estimated to be $(\hbar k \gamma / 2 m_{Cs}) \times t_D^2/2 \sim 10$ nm. This value is negligible compared to the 5 mm-length of the fibre waist.

3.7.4   Modelling of the absorbance profiles

The absorbance profiles can be modelled as follows:

$$A(\delta, P_0) = \frac{\hbar\omega}{P_0} \int \rho_{\delta,P_0}(r,z)\Gamma_s(I_{P_0}(r),\gamma(r),\delta - \delta_{\text{vdW}}(r))dV, \qquad (3.43)$$

where the integral ranges over the space outside the fibre. $\Gamma_s(I_{P_0}(r), \gamma(r), \delta - \delta_{\text{vdW}}(r))$ is the scattering rate of an atom in the evanescent field with intensity $I_{P_0}(r)$, with a position dependent spontaneous emission rate $\gamma(r)$ ($\gamma(r)_{\text{total}}$ in Eq. (3.30)), and a v.d.W. shift of the angular frequency of the atomic transition δ_{vdW} given by Eq. (3.27). The density distribution of the atom cloud is now given by

$$\rho(r,z) = \left\{ \frac{n_0}{\sigma^3 (2\pi)^{3/2}} e^{-(r^2+z^2)/2\sigma^2} \right\} f_{\delta,P_0}(r), \tag{3.44}$$

where the relative atomic density near the fibre $f_{\delta,P_0}(r)$ is obtained from the simulations, the term in curly brackets describes the Gaussian density distribution of the unperturbed MOT, and n_0 is a fitting parameter accounting for the number of atoms inside the MOT.
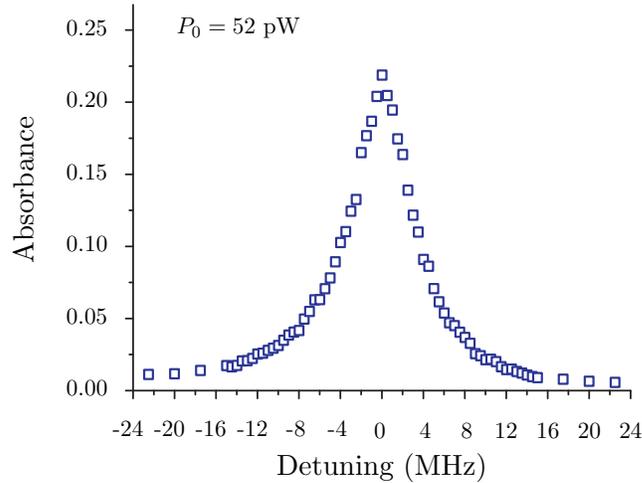
FIGURE 3.30: Simulated absorbance of the atoms as a function of the probe laser detuning with a power of 52 pW.

Figure 3.30 shows the simulated absorbance of the atom cloud as a function of the detuning of the probe laser frequency for a probe power of 52 pW. The number of atoms n_0 has been determined by matching the maximal value of the absorbance with the experimental values. This leads to a peak density at the centre of the cold atom cloud of 7.4×10^9 atoms/cm^3 using Eq. (3.44). Each of the squares shown in the figure are determined by Eq. (3.43) for a given value of the probe laser detuning $\delta/2\pi$, meaning that the relative atomic density $f_{\delta,P_0}(r)$ for the corresponding detuning and laser power is used in the integration. The noise-like variations of the profile stems from the limited amount of trajectories that could simulated. This was due to the complexity of the Monte-Carlo simulations which required a large computing time. In order to infer the linewidth of the simulated absorbance profile the same method as with the experimental values was used.

The effective number of fully saturated atoms contributing to the signal on resonance N_{P_0} reads

$$N_{P_0} = \frac{2}{\gamma_0} \int \rho_{\delta=0}(r,z)\Gamma_s(I_{P_0}(r),\gamma(r),\delta_{\mathrm{vdW}}(r))dV, \qquad (3.45)$$

where the notation used in Eq. (3.43) is followed. Note that N_{P_0} is power dependent and can be lowered by reducing P_0. This is due to saturation: The atoms close to the fibre will not absorb significantly more light while increasing the power, whereas the atoms far from the fibre significantly increase their contribution. This also leads to a power dependency of the mean atom-fibre distance on resonance given by

$$d_{P_0} = <r> - a \qquad (3.46)$$

$$<r> = \frac{\int_a^\infty r^2 \rho_{\delta=0}(r)\Gamma_s(I_{P_0}(r),\gamma(r),\delta_{\mathrm{vdW}}(r))dr}{\int_a^\infty r\rho_{\delta=0}(r)\Gamma_s(I_{P_0}(r),\gamma(r),\delta_{\mathrm{vdW}}(r))dr}, \qquad (3.47)$$

which can be adjusted down to 248 nm for vanishing powers of the probe laser.

3.8 Comparison between the model and the experimental results

Figure 3.31 shows four examples of measured (black solid) and simulated (squares) absorbance profiles for different powers of the probe laser ranging over three orders of magnitude: (a) 6 pW, (b) 52 pW, (c) 200 pW, and (d) 1 nW. The zero-point frequency has been chosen as to be equal for the experimental and simulated values. Note that the simulations predict a small frequency shift on the order of 0.5 MHz in the regime of low powers, however, an observation of this shift was beyond the spectroscopic precision of our experimental setup. The fitted value of the peak atomic density is obtained by matching the simulated absorbance on resonance with the experimental values.

Probe power (pW)	Fitted peak density ($\times 10^9$ at/cm^3)	N_{P_0}	d_{P_0} (nm)
6	6.2	0.3	249
52	7.4	2	281
200	8.6	7	328
1000	8.9	17	407

TABLE 3.2: Values of the probe laser power, fitted peak density, effective number of fully saturated atoms N_{P_0} and mean distance of the probed atoms to the fibre d_{P_0} corresponding to the measurements shown in Fig. 3.31.

The values of the fitted peak density, the effective number of fully saturated atoms N_{P_0}, and the mean distance of the probed atoms to the fibre d_{P_0} corresponding to the measurements on Fig. 3.31 (a)–(d) are shown on Table 3.2. Figures 3.32 (a), (b) and (c) show the variation of the values N_{P_0}, d_{P_0}, and the fitted peak atomic density as a function of the probe laser power, respectively. Surprisingly, the fitted peak density of the cold
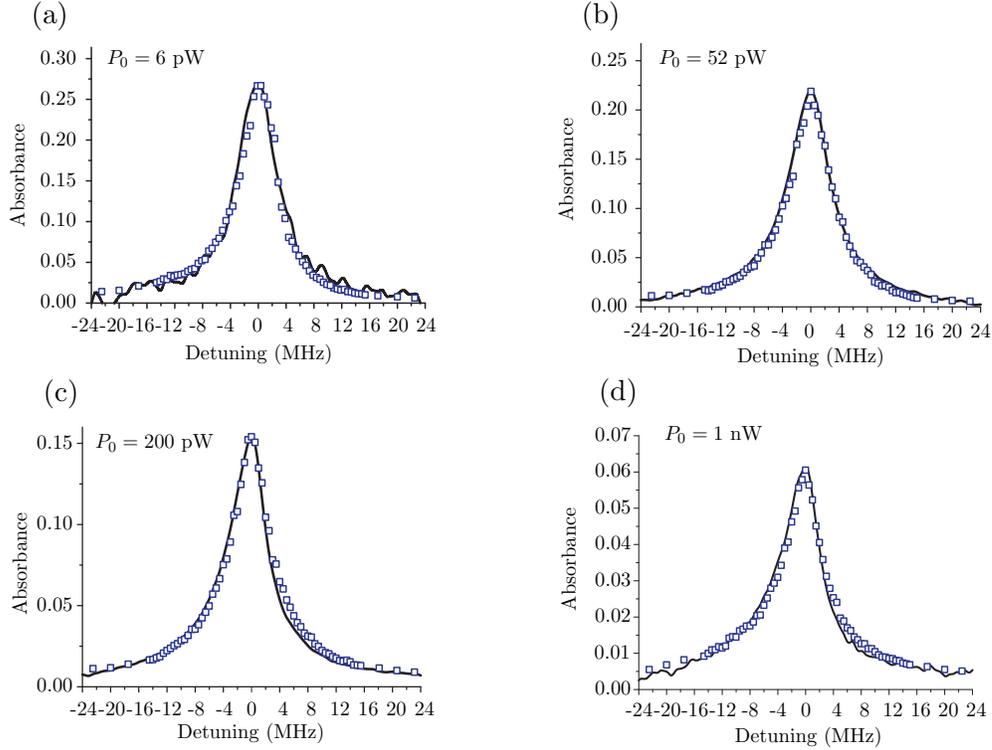
FIGURE 3.31: Measured (black solid) and simulated (squares) absorbance profiles of the atoms as a function of the detuning of the probe laser for a power of (a) 6 pW, (b) 52 pW, (c) 200 pW, and (d) 1 nW. The effective number of fully saturated atoms contributing to the spectra is 0.3, 2, 7, and 17, respectively (see Eq. (3.45)).

atom cloud depends on the power of the probe laser (see (c)). This is presumably due to the accumulation of thermal atoms at the surface of the TOF resulting in a change of the transmission through the fibre as a function of the probe power: When the Cs reservoir is open the atoms are adsorbed on the surface of the fibre as well as on the walls of the vacuum chamber due to the v.d.W. potential. It has recently been shown that a laser propagating through a TOF can produce light-induced atomic desorption (LIAD) of the atoms accumulated on the surface of the waist resulting in a self-modulated transmission as a function of the laser power [83], being the transmission for low powers of the probe laser lower than for large powers. This can lead to an underestimation of the probe laser power at the position of the cold atoms in the regime of low powers. When using this value of the measured probe laser power to simulate the absorbance given by Eq. (3.43), the calculated peak absorbance becomes larger than in the measurement. This results in a lower value of the fitting parameter n_0 when matching the calculations to the experimental data and therefore leads to a lower value of the calculated peak density of the cold atom cloud. The influence of the adsorbed atoms on the transmission through the fibre has also been observed in our setup, specially when using the Cs-dispensers:
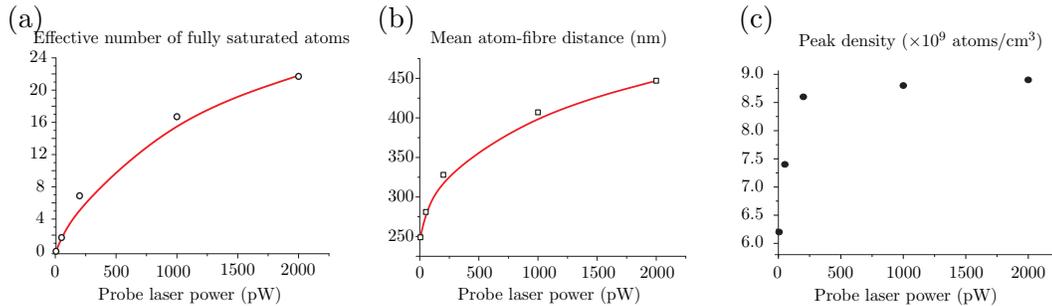
FIGURE 3.32: Effective number of fully saturated atoms on resonance (a) , Mean atom-fibre distance on resonance (b), and peak density of the atom cloud (c) as a function of the probe laser power. The red solid curves are a guide to the eye.

At low powers of the probe laser (1 to 100 pW), the transmission decreases over a time-scale ranging between few seconds to few minutes after turning on the current applied on the dispensers. If an additional off-resonant laser with a power of few tenths of μW is launched through the fibre, the transmission of the probe recovers its original value. When using the Cs reservoir the same effect has also been observed in a minor degree. In addition, a non-reversible decrease of the transmission through the fibre over several months has been observed, possibly due to degradation of the surface at the waist.

Figure 3.33 shows the width of the measured absorbance profiles versus the probe laser power (circles). The linewidths predicted by the full model are shown in red squares. The red line joining the simulated values is a guide to the eye. For comparison, the expected linewidths in absence of light-induced dipole forces and surface interactions (solid line) are also shown. While the full model agrees very well with the experimental data, the reduced model strongly deviates both for high and low powers. For probe laser powers larger than 50 pW, the absorbance profiles are considerably narrower than what would be expected in absence of dipole forces and surface interactions. For 1 nW of probe laser power this narrowing exceeds 40%. As shown in Fig. 3.29, the narrowing can be explained by the effect of the light-induced dipole forces on the density of the atomic cloud. For distances smaller than 370 nm, i. e., in the region that contains more than 75% of the evanescent field power, the largest integrated density of the atomic cloud is predicted in the case of zero detuning. For blue ($\delta/2\pi = +3$ MHz) and red ($\delta/2\pi = -3$ MHz) detunings, this integrated density is lowered due to the effect of the light-induced dipole forces. This results in a reduced absorbance and leads to an effective narrowing of the absorbance profile. In addition, the measured asymmetry of the absorbance profiles for large powers is also reproduced (see Fig. 3.31 (d)). The integrated density for red detunings is larger than for blue detunings (see Fig. 3.29).

Figure 3.34 shows the linewidths for the limit of low probe laser powers, i. e., low saturation and negligible light-induced dipole forces. The measured linewidths approach 6.2 MHz for vanishing powers. This result exceeds the natural Cs D_2 linewidth in free space by almost 20 %. This broadening can be explained by surface interactions, i. e., the
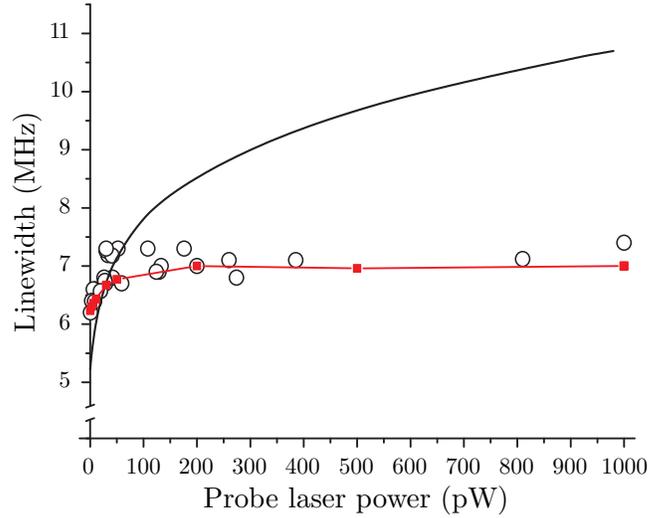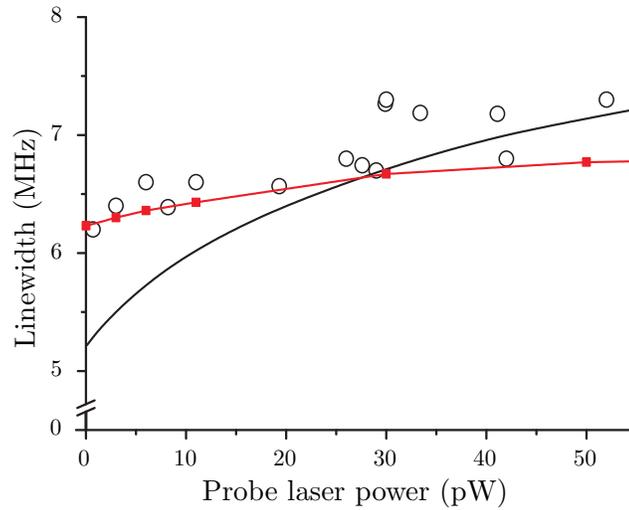
FIGURE 3.33: Linewidth of the absorbance profiles versus the probe laser power for the full range of powers. The squares (circles) correspond to the simulated (experimental) values. The red line joining the simulated values is a guide to the eye. The solid line is the reduced model not taking into account light-induced dipole forces and surface interactions.

vdW shift of the Cs D_2-line and the modification of the spontaneous emission rate of the atoms near the fibre. Both effects have the same magnitude and only their combination yields the very good agreement between the full model and the experimental data.

The v.d.W. interaction and the modification of the spontaneous emission rate of the atoms near the fibre have been described in Sec. 3.7.2. Their influence on the broadening of the absorbance profiles can be sumarised as follows:

- Van der Waals interaction: The resonance frequency of the atoms is red-shifted as a function of the atom-surface distance. When several atoms at different radial positions simultaneously interact with the evanescent field the measured absorbance profiles are inhomogeneously broadened. This also results in a red-shift of the peak of the curves predicted by the simulations that could not be experimentally resolved.

- Increase of the spontaneous emission rate: The spontaneous emission rate of the atoms is directly related to the linewidth of the absorption profiles. Hence, an increase of the spontaneous emission rate of the atoms near the fibre results in a broadening of the lines.

The effect of the surface interactions is only apparent for low laser powers for two reasons: Firstly, the light-induced dipole forces that narrow the profiles must be negligible. Secondly, the mean distance of the probed atoms depends on the probe laser power (see

Eq. (3.47)), i. e., the lower the powers, the closer the probed atoms are to the fibre surface. The limiting value is given by the shape of the evanescent field and by the on-resonance relative atomic density close to the fibre (Fig. 3.29 (solid)). However, for red-detuned frequencies of the probe laser the mean distance of the probed atoms from the fibre surface is further reduced [34].

FIGURE 3.34: Linewidth of the absorbance profiles versus the probe laser power for the range of low powers. The squares (circles) correspond to the simulated (experimental) values. The red line joining the simulated values is a guide to the eye. The solid line is the reduced model not taking into account light-induced dipole forces and surface interactions.

Chapter 4

Probing the fluorescence of laser cooled atoms with an ultra-thin optical fibre

In Chap. 3 it has been demonstrated that the evanescent field arising around a 500-nm diameter ultra-thin optical fibre can be used to probe and mechanically influence laser cooled caesium atoms. It has also been shown that the presence of the guided fibre mode substantially enhances the spontaneous emission of atoms near the fibre surface. The following Chapter deals with the measurement of the spontaneous emission of Cs atoms inside a MOT using the waist of a TOF. The ultra-thin part of a TOF can be used as a sub-wavelength probe to efficiently collect and guide the fluorescence emitted by the atoms. The large evanescent field and the strong confinement of the guided fibre mode results in a substantial probability for an atom to spontaneously emit photons into the guided mode. Recently, it has been theoretically calculated that a Cs atom placed on the surface of a 400-nm diameter fibre can emit about 30% of its fluorescence into the HE_{11} mode [38]. On the experimental side, in an experiment similar to the one presented here the fluorescence of less than 0.1 atoms on average has recently been measured [34].

The experimental setup used for this experiment is the same as the one described in Sec. 3.2. However, in what follows, the probe laser was not used. Instead, the atoms are excited using the cooling laser and their fluorescence coupled to the fibre mode is detected by the APD at one end of the fibre.

Figure 4.1 conceptually describes the experimental scenario (a) and the time-sequence (b). As described in Sec. 3.3.3, the MOT is spatially overlapped with the waist of the TOF. The fluorescence of the atoms is modulated by switching the repump laser that excites the $6^2S_{1/2}F = 3 \rightarrow 6^2P_{3/2}F' = 4$ transition. The repump laser of a Cs MOT is used to counteract the pumping to the $F = 3$ state produced by the off-resonance excitation of the $F = 4 \rightarrow F' = 4$ transition by the cooler laser (see Sec. 3.3.1). Hence,

(a)

(b)

photodetector
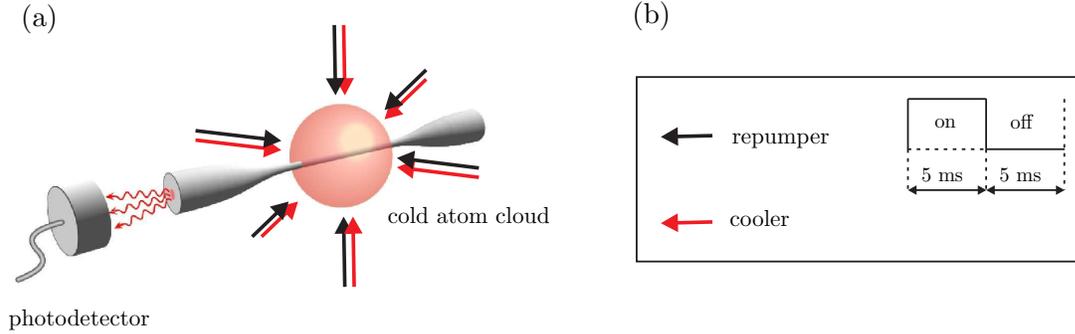
FIGURE 4.1: Sketch of the experimental setup (a) and the timing sequence of the experiment (b). A cloud of laser cooled atoms is spatially overlapped with a 500-nm diameter waist of a TOF. The coupling of the fluorescence emitted by the atoms into the guided fibre mode is measured using a photodetector.

by switching the repump laser on and off the atoms can be optically pumped into the $F = 3$ state. In this state, the atoms do not absorb photons from the cooling laser and their fluorescence ceases. The experimental time-sequence is divided into the following intervals: During the first 5 ms the repump laser is on. The MOT cools and traps the atoms and a significant part of the photons scattered by the atoms during the cooling is emitted into the fibre mode and is subsequently detected with the APD. During this period the population remains mostly in the $F = 4$ and the $F' = 5$ states. During the second period of 5 ms the repump laser is blocked using a chopper wheel.

The population of the energy levels during the two periods is schematically shown in the upper graphs of Figs. 4.2 (a) and (b), respectively. The resonant transitions of the cooling and repump lasers are indicated by the solid arrows. The off-resonant excitation $F = 4 \rightarrow F' = 4$ is indicated by the dashed arrow. The curly arrows indicate the spontaneous emission. In the lower graphs the corresponding coupling of the atomic fluorescence into the guided fibre mode is schematically shown. Figure 4.2 (a) describes how the atoms located within the decay length of the evanescent field spontaneously emit into the guided fibre modes. On the other hand, atoms the that are outside this decay length will not contribute to this process [34]. Figure 4.2 (b) schematically shows that the atoms that have been optically pumped into the $F = 3$ level do not emit fluorescence.

Figure 4.3 shows the measured power at one fibre end as a function of time using the experimental sequence described in Fig. 4.1 (b). The signal has been averaged over 4096 traces. Note that the total amount of power coupled into the guided mode is twice as large since the detection is only performed at one end of the fibre. The black line shows the measurement with an optimal alinement between the fibre waist and the MOT. The rise time of the detected power is on the order of the rise time of the APD (~ 0.2 ms), whereas the decay time is much longer (~ 1 ms). The latter is due to the finite time
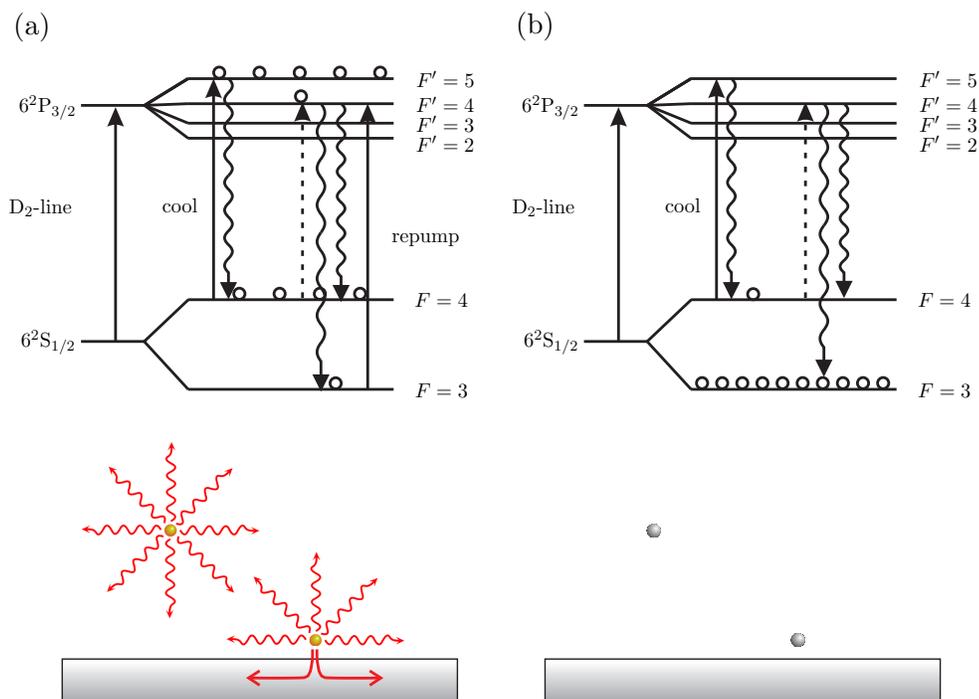
FIGURE 4.2: On the top the level scheme of the D_2-line of Cs and the laser induced transitions with (left) and without (right) repump laser is shown. The solid arrows denote the resonant laser excitations, the dashed arrow the off-resonant $F = 4 \rightarrow F' = 4$ excitation, the curly arrows the spontaneous emission, and the circles the population distribution. On the bottom the coupling of the atomic fluorescence at the fibre waist is schematically shown, correspondingly.
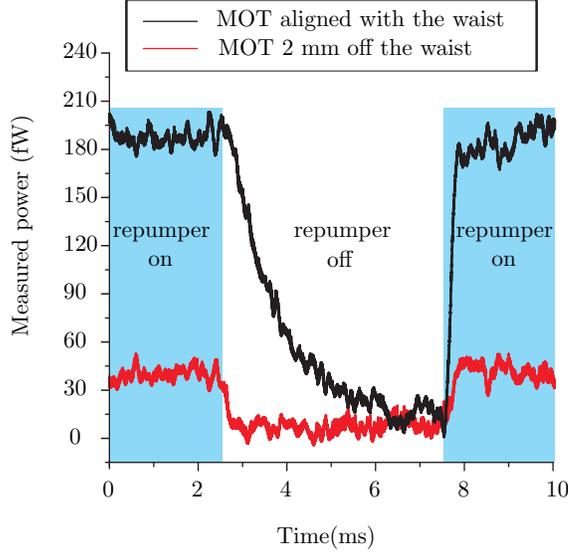
FIGURE 4.3: Detected power at the fibre end as a function of time with optimal alinement between the fibre and the MOT (black) and 2 mm displacement of the MOT (red). The periods where the repump laser is on (off) are shaded in blue (white).

it takes to optically pump the atoms into the $F = 3$ level. The probability for the atoms to be excited on the $F = 4 \rightarrow F' = 4$ transition in the MOT is small compared to the probability of the $F = 4 \rightarrow F' = 5$ transition. Hence, the pumping process is long compared to the lifetime of the atom. This relative probability can be estimated as $\sim 10^{-4}$, i.e., one atom scatters on average 10^4 photons from the cooling laser before being pumped into the $F = 3$ state. This results in an expected time constant of the optical pumping on the order of 1 ms [84].

As a comparison, a reference measurement with a misalinement of 2 mm between the fibre waist and the MOT is shown (red). This was done using a permanent magnet that allows displacement of the MOT over several mm. The atoms are too far from the waist to emit into the guided mode and the detected signal therefore corresponds to the coupling of the repump laser at the waist. The constant coupling of the cooling laser does not contribute to the measured signal which was recorded in AC modus. Note that the rise and decay times for the reference measurement are on the order of the reaction time of the APD. The amount of power emitted by the atoms into the guided mode can then be estimated by substracting the two measurements.

The power detected in the measurement shown in Fig. 4.3 is proportional to the population in the $F = 4$ state. Hence, the population distribution among the hyperfine levels of the ground state can be inferred from this measurement. Figure 4.4 shows the time variation of the population in the $F = 4$ state $p_4(t)$ normalised to the total population in the ground state $p_4(t) + p_3(t)$ upon switching off the repump laser. Note that $p_3(t)$ denotes the population in the $F = 3$ state. An exponential function of the
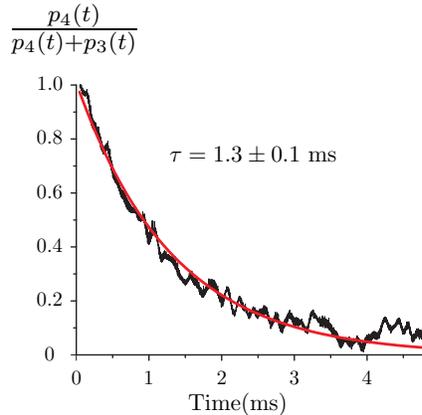
$$\frac{p_4(t)}{p_4(t)+p_3(t)}$$

FIGURE 4.4: Decay of the population in the $F = 4$ hyperfine state $p_4(t)$ normalised to the total population of the ground state $p_4(t) + p_3(t)$ (black). The red curve is an exponential function that has been fitted to the experimental values with a decay constant equal $\tau = 1.3 \pm 0.1$ ms. $t = 0$ corresponds to the time when the repump laser is switched off.

form $f(t) = f_0 \exp[-t/\tau]$ (red) has been fitted to the experimental values yielding a decay constant of $\tau = 1.3$ ms. This result is in good agreement with the expected time constant of the optical pumping of 1 ms.

The value of the probability for one atom to be pumped into the $F = 3$ state can now be determined: Using Eq. (2.15) in Sec. 2.2 the scattering rate of the atoms in the MOT can be estimated. Assuming a total intensity of the molasses of $I_{\mathrm{MOT}} = 10 I_s$ and a red-detuning of the cooling laser equal to the natural linewidth a value of 10.9×10^6 s^{-1} is obtained for the scattering rate. Matching this result to the measured time constant of the optical pumping into the $F = 3$ state equal $\tau = 1.3$ ms yields a value of $(0.7 \pm 0.1) \times 10^{-4}$ for the pumping probability. This is in good agreement with the expected probability of 10^{-4}.

One could expect that the presence of the fibre affects the time constant of the optical pumping process being considered. This is not the case for two reasons: Firstly, the optical pumping of the atoms takes place at any distance from the fibre surface. Secondly, one atom spends in average 1 μs in the vicinity of the fibre (see Sec. 3.6.4), which is negligible compared to the time it takes to pump the atoms into the $F = 3$ state (1.3 ms).

4.1   Emission rate into the guided mode

The total power measured in Fig. 4.3 when the repump laser is on can be used to investigate the efficiency of the TOF as a tool for probing the atomic fluorescence. The spontaneous emission rate of the atoms into the guided mode at the surface of the fibre

is a measure of this efficiency. The total amount of power coupled into the guided fibre mode is given by

$$P_{\text{guided}} = \int \hbar\omega\rho(r,z)\frac{\gamma_{\text{guided}}(r)}{\gamma(r)}\Gamma_s(I_{\text{MOT}},\gamma(r),\delta_{\text{MOT}}-\delta_{\text{vdW}})dV. \tag{4.1}$$

$\Gamma_s(I_{\text{MOT}},\gamma(r),\delta_{\text{MOT}}-\delta_{\text{vdW}})$ is the scattering rate of an atom illuminated by the molasses of the MOT including the surface interactions (see Sec. 3.7). $\gamma(r)$ is the total spontaneous emission rate of the atom ($\gamma_{\text{total}}(r)$ in Eq. (3.30)), δ_{vdW} is the v.d.W. shift of the atomic transition frequency given by Eq. (3.27), and $\rho(r,z)$ the density of the atom cloud given by

$$\rho(r,z) = \left\{\frac{n_0}{\sigma^3(2\pi)^{3/2}}e^{-(r^2+z^2)/2\sigma^2}\right\}f(r). \tag{4.2}$$

n_0 is the number of atoms inside the MOT and the relative density factor $f(r)$ is obtained as described in Sec. 3.7. The spontaneous emission rate of the atoms into the guided mode $\gamma_{\text{guided}}(r)$ is given by

$$\gamma_{\text{guided}}(r) \simeq \gamma_a\gamma_0\frac{|\vec{E}(r)|^2}{|\vec{E}(a)|^2}. \tag{4.3}$$

Hence, the spontaneous emission rate into the guided mode at the fibre surface is $\gamma_{\text{guided}}(a) \simeq \gamma_a\gamma_0$, where γ_0 is the spontaneous emission rate of the atoms in free-space. By comparing Eq. (4.1) with the experimental values shown in Fig. 4.3 the value of $\gamma_{\text{guided}}(a)$ can be deduced. Assuming a peak density of the atom cloud equal 1×10^{10} atoms/cm^3 (see Sec. 3.8), an overall intensity of the molasses of $I_{\text{MOT}} = 10I_s$, and a red-detuning of the cooling laser equal to the natural linewidth a value of $\gamma_a = 0.19$ is obtained. According to Eqns. (3.37), γ_a has a theoretically calculated value of 0.28.

Comparison with the previous measurements of the atomic absorption

The measurements described in Chap. 3 can also be used to deduce a value for $\gamma_{\text{guided}}(a)$. The experimental sequence used for this measurements has been described in Sec. 3.5 and will not be repeated here.

The upper graph of Fig. 4.5 shows a measurement of the transmission of the probe laser as a function of time in the presence of the atoms (black) and in their absence (red). The latter was realised by switching off the magnetic field. The centre pulse starting at $t = 0$ corresponds to the transmission of the probe laser. This is not relevant for the calculations presented in this section. In the following, the description will be focused on the cooling period shaded in blue. During this period the atoms are trapped and cooled in the MOT. The power detected at one end of the fibre with (black) and without (red) atoms is shown in the lower graph. The spontaneous emission into the guided fibre mode is given by the difference between the two measurements leading to a value of about 500 fW. This value is much larger than the value of the fluorescence shown in Fig. 4.3. This difference between the two measurements is probably due to the different
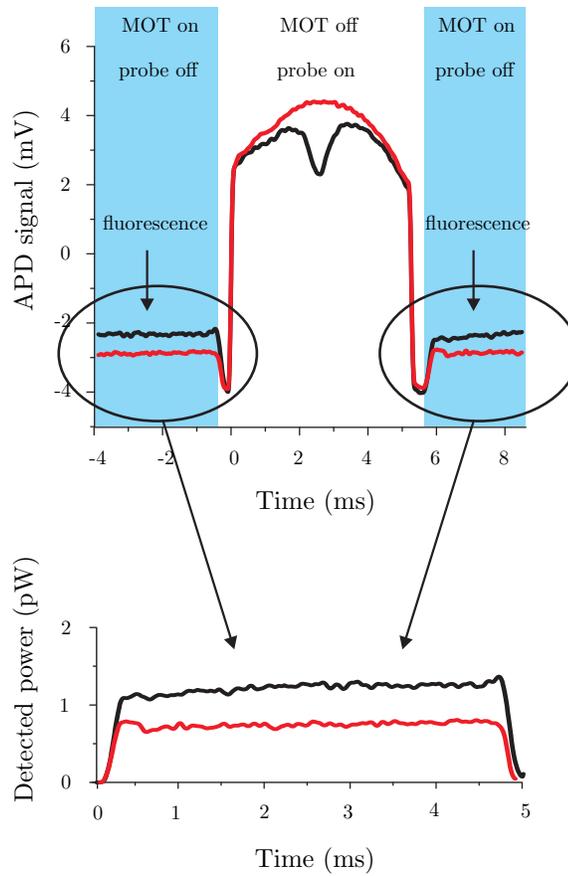
FIGURE 4.5: Upper graph: Measured signal in the APD as a function of time during the experimental sequence described in Sec. 3.5 with (black) and without atoms (red). The cooling cycle is shaded in blue. Lower graph: Power detected at one end of the fibre during the cooling cycle. The power calibration of the APD is 1.38 mV/pW. $t = 0$ corresponds to the time when the cooling cycle starts.

density of the atom cloud. Indeed, the density of the atom cloud can vary in one order of magnitude when modifying the power or the detuning of the molasses.

Using the results of 9 measurements equivalent to the one shown in Fig. 4.5 performed under the same experimental conditions, an average value of (313 ± 112) fW is obtained for the detected fluorescence of the atoms. This leads to a value of $\gamma_a = 0.35 \pm 0.13$. A peak density of the atom cloud equal 1×10^{10} atoms/cm^3 (see Sec. 3.8), an overall intensity of the molasses of $I_{\mathrm{MOT}} = 10 I_s$, and a red-detuning of the cooling laser equal to the natural linewidth have been assumed for the calculations.

The two estimations of the value γ_a demonstrate the good effectiveness of the collection of the atomic fluorescence at the ultra-thin part of the TOF. An optimisation of the fibre radius as described in Sec. 1.2.3 could further improve the sensitivity up to 30%.

Chapter 5

Towards atom-trapping in evanescent field dipole traps around ultra-thin optical fibres

Dipole traps which rely on the dipole forces arising from the interaction of neutral atoms with far-detuned light fields have been one of the key advances in quantum optics in the last decade. Such traps have been used in many variants to trap and guide single neutral atoms [3], form an all-optical Bose-Einstein condensate (BEC) [85], or form a BEC of diatomic molecules [86] among others. Moreover, the atoms located in the trap are embedded in a far-detuned optical field providing weak resonant interaction that allows to control their external degrees of freedom while preserving the coherence of the atomic internal states [87]. The latter is a necessary condition for the implementation of quantum information processing. Within this context, the precise control of the interaction between the trapped atoms (acting as a storage unit of the information) and the photons (acting as the carriers of the information) is a crucial issue [88]. In the previous Chapters ultra-thin optical fibres have been proven to be a very promising tool to control this interaction: guided photon to atom (Chap. 3) and atom to guided photon (Chap. 4). In a theoretical proposal it has been shown that trapping and guiding of neutral atoms in the evanescent field arising around the waist of a TOF is conceivable [39]. This method would allow to mechanically manipulate the atoms while controlling their coupling to the guided fibre modes thereby realising fibre-coupled atomic ensembles. Such a configuration would, e. g., be promising for slow-light light experiments with ensembles of fibre-coupled atoms [40] and for the implementation of two-photon quantum gates using electromagnetically induced transparency (EIT) [41]. One scheme to trap Cs atoms in the evanescent field around a 500-nm diameter fibre based on a two-colour dipole trap is described in this Chapter both theoretically (Sec. 5.1) and experimentally (Sec. 5.2).

5.1   Two-colour evanescent field dipole trap

The characteristic decay length Λ of the evanescent field intensity outside the fibre depends on the wavelength of the guided light. This feature makes it possible to concieve a two-colour trapping scheme for Cs atoms around an ultra-thin optical fibre where the two laser frequencies have opposite signs of the detuning with respect to the atomic transition frequency. The right combination of a repulsive potential (blue-detuned) with a shorter decay length and an attractive potential (red-detuned) with a longer decay length leads to a trapping minimum at a few hundred nanometres from the fibre surface. While the attractive potential prevents the atoms from escaping towards larger radial positions, the repulsive potential counteracts the attractive potential and the v.d.W. potential near the surface preventing the atoms from colliding with the fibre. In addition, coupling the red-detuned laser from both fibre ends in a standing wave configuration produces a sinusoidal modulation of its intensity along the fibre axis allowing 3-dimensional confinement of the atoms. This modulation leads to the formation of an array of microtraps along the fibre waist with a period of about half a micrometre extending over a length of several millimetres.

The wavelength-dependency of the decay length of the evanescent field can be appreciated in Figs. 5.1 (a) and (b). In (a) the radial variation of the intensity of the electric field propagating in the HE_{11} mode of a 250-nm radius optical fibre with rotating polarisation is shown (see Sec. 1.2.1). For comparison, two different wavelengths have been used: 780 nm (blue solid) and 1064 nm (red dashed). The surface is indicated by the vertical line at $r = 250$ nm. On the right hand side of the surface the different characteristic decay lengths of the intensity in the evanescent field for different wavelengths become apparent. The 780-nm field is more tightly bound to the fibre than the 1064-nm field. The appropriate choice of the laser powers allows to adjust the radial position where the light-induced potentials cancel. Figure 5.1 (b) shows the variation of the characteristic decay length of the evanescent field as a function of the V parameter (see Eq. (1.14) in Sec. 1.2). A larger wavelength leads to a larger characteristic decay length of the evanescent field.

5.1.1   Linearly polarised fields

I will now calculate the trapping potential created by two linearly polarised fields propagating along the fibre. The dipole potential created by the evanescent field of two x-polarised lasers with different frequencies propagating in the fundamental mode of the fibre is given by

$$U_d(r, \phi) = \frac{1}{2}(\text{Re}[\alpha_1]|\vec{E}_1(r, \phi)|^2 + \text{Re}[\alpha_2]|\vec{E}_2(r, \phi)|^2), \qquad (5.1)$$

where $|\vec{E}_i(r, \phi))|^2$ with $i = 1, 2$ denotes the value of the cycle-averaged squared electric field outside the fibre given by Eq. (1.29). $\text{Re}[\alpha_i]$ is the real part of the polarisability of
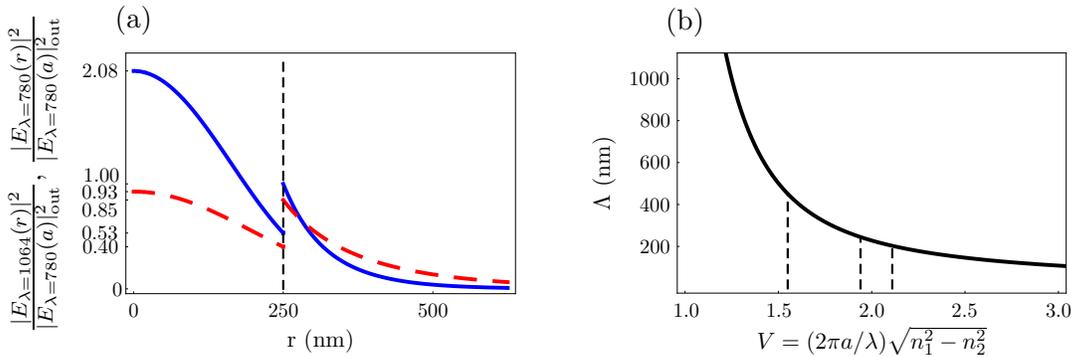
FIGURE 5.1: (a) absolute value of the squared electric field propagating in the HE_{11} mode at wavelengths of 780 (blue solid) and 1064 nm (red dashed) normalised to the value $|E_{\lambda=780}(a)|^2_{\text{out}}$ as a function of the radial position. The power of the two lasers is assumed to be equal. (b) variation of the characteristic decay length Λ as a function of the V parameter. The three vertical dashed lines indicate the values of $\Lambda_{\lambda=1064} = 452$, $\Lambda_{\lambda=852} = 244$, and $\Lambda_{\lambda=780} = 200$ nm corresponding to three different wavelengths considered in this work, 1064, 852, and 780 nm. The calculations have been performed for a fixed fibre radius of 250 nm.

a multilevel atom in a far-detuned electric field given by Eq. (2.27). If the second laser is set in a standing wave configuration, an additional axial modulation of the intensity of the field arises [42] yielding,

$$U_d(r, \phi, z) = \frac{1}{2}(\text{Re}[\alpha_1]|\vec{E}_1(r, \phi)|^2 + 4\text{Re}[\alpha_2]|\vec{E}_2(r, \phi)|^2 \cos^2[\beta_2 z]). \tag{5.2}$$

The total potential experienced by the atoms is given by the sum of the dipole potential U_d and the van der Waals potential V_{vdW} (Eq. (3.22)) as

$$U(r, z) = U_d(r, z) + V_{\text{vdW}}(r). \tag{5.3}$$

The v.d.W. potential between a ground-state Cs atom and an infinite planar silica surface given by Eq. (3.28) is used. As explained in Sec. 3.7.2, this is always a conservative assumption.

Figure 5.2 shows the variation of the trapping potential for a ground-state Cs atom in the evanescent field as a function of the distance from the fibre surface along the x-axis (a) and along the y-axis (b) at $z = 0$. The calculations have been performed for a fibre radius of 250 nm, a blue-detuned laser ($\vec{E}_1$) at a wavelength of 780 nm with a power of $P_{780} = 30$ mW and a red-detuned laser ($\vec{E}_2$) at a wavelength of 1064 nm with a total power of $P_{1064} = 13$ mW (6.5 mW in each of the arms of the standing wave). Note that the total amount of power coupled into the fibre is 43 mW, which is a reasonable value for a fibre in UHV environment.[1] The plot of the trapping potential

---

[1]Appropriately fabricated fibres with a radius ranging from 200 to 500 nm can carry more than 300 mW in such an environment without fusing. This is, to the author's knowledge, an unprecedented achievement which is, yet, not fully understood.

in the x-direction (parallel to the polarisation of the fields) is shown in (a). The 1.5-mK depth of the potential at the minimum suffices to trap Cs atoms that have been previously trapped and cooled in a MOT (see Sec. 3.3.1). On the other hand, the potential in the y-direction (perpendicular to the polarisation of the fields) shown in (b) is significantly shallower with a depth of 0.78 mK. This behaviour stems from the different strength of the evanescent field depending on the orientation of the polarisation with respect to the fibre surface, leading to a "strong" (a) and a "weak" (b) direction of the potential. The minimum of the trapping potential is located in the "strong" direction at a distance of $d = 240$ nm from the fibre surface. The trapping oscillation frequency in the x-direction at the potential minimum calculated using an harmonic oscillator approximation is $\omega_r/2\pi = 428$ kHz. The extension of the trapping volume along the radial direction for an atom at a temperature of 100 μK is equal to 85 nm.

To account for the experimental inaccuracies in the adjustment of the laser powers the blue dashed and red dotted curves are shown in Figs. 5.2 (a) and (b). The blue dashed line has been calculated for the case where the power of the blue-detuned laser is $P_{780} = 1.15 \times 30$ mW and the power of the red-detuned laser $P_{1064} = 0.85 \times 13$ mW. This implies an inaccuracy of 15% in the adjustment of the powers but also an anti-correlation of the variations leading to a "worst case" situation: An increase in the power of the blue-detuned laser (repulsive potential) shifts the trapping minimum towards larger radial positions and decreases the depth of the trap. A decrease of the power of red-detuned laser (attractive potential) has a similar effect. Hence, the trap depth decreases to 0.89 mK in the "strong" direction and the trapping minimum is displaced towards larger radial position at a distance of 299 nm from the fibre surface. Despite the shallowing of the trap, the depth still suffices to trap laser cooled Cs atoms. The inverse situation is described by the red dotted line. The power of the blue-detuned laser is set to $P_{780} = 0.85 \times 30$ mW and the power of the red-detuned laser to $P_{1064} = 1.15 \times 13$ mW. The trap depth increases to 2.55 mK and the trapping minimum is displaced towards the fibre surface at a distance of 179 nm. The repulsive potential created by the blue-detuned laser is still sufficient to counteract the v.d.W. potential. Thereby, a positive valued maximum of the potential separating the atoms from the fibre is maintained. If the v.d.W. potential cannot be totally counteracted, the free atoms may find a path towards the fibre surface before being cooled into the trap. This will result in a lower loading efficiency. This treatment shows that the proposed trap configuration is robust against experimental inaccuracies in the adjustment of the laser powers.

Figure 5.3 shows the contour plots of the trap in the planes $x = 0$ (a) and $y = 0$ (b) for the same parameters as in Fig. 5.2 (black solid). Although the v.d.W. potential has been taken into account in the calculations, the contours are too close to the fibre to be recognisable and have been suppressed from the plot. The trap exhibits a periodicity of $\pi/\beta_2 = 498$ nm in the axial direction, which corresponds to the standing-wave periodicity of $\lambda/2$, where $\lambda = 2\pi/\beta_2$ is the wavelength of the red-detuned laser in the fibre and β_2 the propagation constant. The axial oscillation frequency of the trap in the plane $x = 0$ is calculated to be 651 kHz. The extension of the trapping volume along the axial direction for an atom with a kinetic energy corresponding to 100 μK is 54 nm. The

contour plot of the trap in the plane $z = 0$ is shown in Fig. 5.4, exhibiting the symmetry breaking already seen in Figs. 5.2 (a) and (b). The calculated trap frequency and trap size in this direction are 98 kHz and 363 nm, respectively. The resulting configuration consists of two axial arrays of microtraps at each side of the fibre with an estimated volume of 1.7×10^{-15} cm^3 for each microtrap at the considered atomic temperature.

Scattering rate, trapping lifetime and coherence time of the atoms in the trap

Following the notation introduced in Eq. (5.1), the scattering rate of a multi-level atom at the axial position of the microtrap reads

$$\Gamma_s = \frac{1}{2\hbar}(\text{Im}[\alpha_1]|\vec{E}_1(r,\phi)|^2 + 4\text{Im}[\alpha_2]|\vec{E}_2(r,\phi)|^2), \tag{5.4}$$

where $\text{Im}[\alpha_i]$ is the complex part of the polarisability of the atom given by Eq. (2.28). A total scattering rate of 28 s^{-1} for a Cs atom located at the trapping minimum is obtained. The individual scattering rates of the red- and blue-detuned lasers are $\Gamma_{1064} = 5.7$ s^{-1} and $\Gamma_{780} = 22.3$ s^{-1}, respectively. The coherence time of one atom in the microtrap is limited by the scattering rate of the atoms as

$$\tau_{\text{coh}} = \frac{1}{\Gamma_s}, \tag{5.5}$$

leading to a value of $\tau_{\text{coh}} = 36$ ms. Every scattered photon imparts an energy equal two times the recoil energy $\mathcal{E}_i^{(\text{rec})} = (\hbar\beta_i)^2/2m_{Cs}$ where β_i is the propagation constant of the fields $i = 1, 2$ in the HE$_{11}$ mode. The absorption of photons from the dipole lasers results in a heating of the atoms that limits their lifetime in the trap. For a trap depth of U_0, the quantity [39]

$$\tau_{\text{trap}} = \frac{U_0}{2\sum_i \mathcal{E}_i\Gamma_i} \tag{5.6}$$

provides a good estimation of the trap lifetime due to recoil heating. The value of the lifetime of a Cs atom in the microtrap is then $\tau_{\text{trap}} = 185$ s. Note that this time is much longer than the typical lifetime of the atoms in a dipole trap of ~ 10 s due to background gas collisions at a pressure of 10^{-10} mbar [4]. Hence, the recoil heating is not a limiting factor for the lifetime of the atoms in the trap.

Light Shifts

The quantum-mechanical interpretation of the dipole potential is based on light-induced energy shifts of the atomic levels in the presence of an external field. In some special cases the light shift of the ground state of the atom is equivalent to the dipole potential in the (semi)classical picture of the atom-field interaction. This is the case for the light-shifts induced by a π-polarised field, where the different magnetic sub-levels of the ground

(a)

(b)
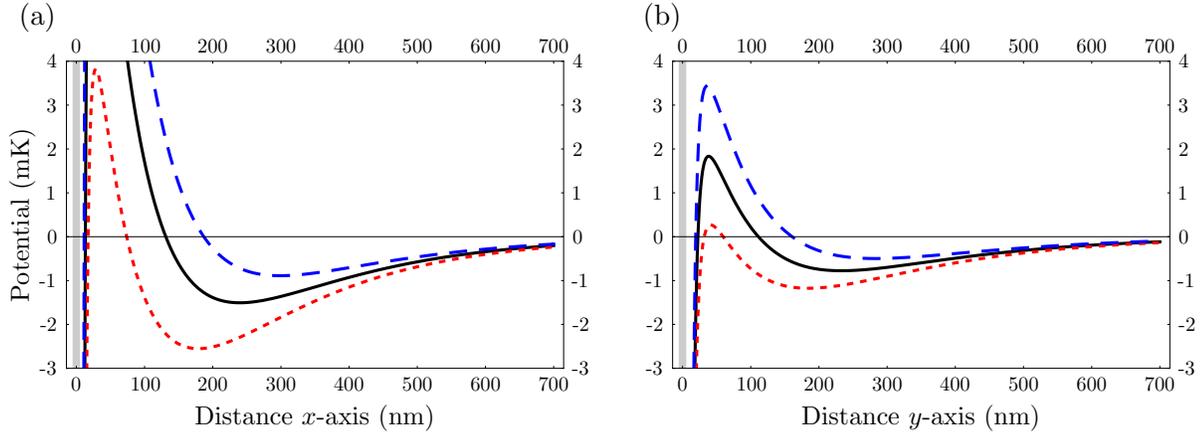
FIGURE 5.2: Variation of the trapping potential at $z = 0$ as a function of the distance from the fibre surface along the x-axis (a) and along the y-axis (b) assuming x-polarisation of the two-colour evanescent field. The solid black curve has been calculated for $P_{1064} = 13$ mW and $P_{780} = 30$ mW. The dashed and dotted curves correspond to two cases of a mismatch in the laser powers: Blue dashed line for $P_{1064} = 0.85 \times 13$ mW and $P_{780} = 1.15 \times 30$ mW, and red dotted line for $P_{1064} = 1.15 \times 13$ mW and $P_{780} = 0.85 \times 30$ mW. The surface of the fibre is indicated by the vertical grey line.

(a)

(b)
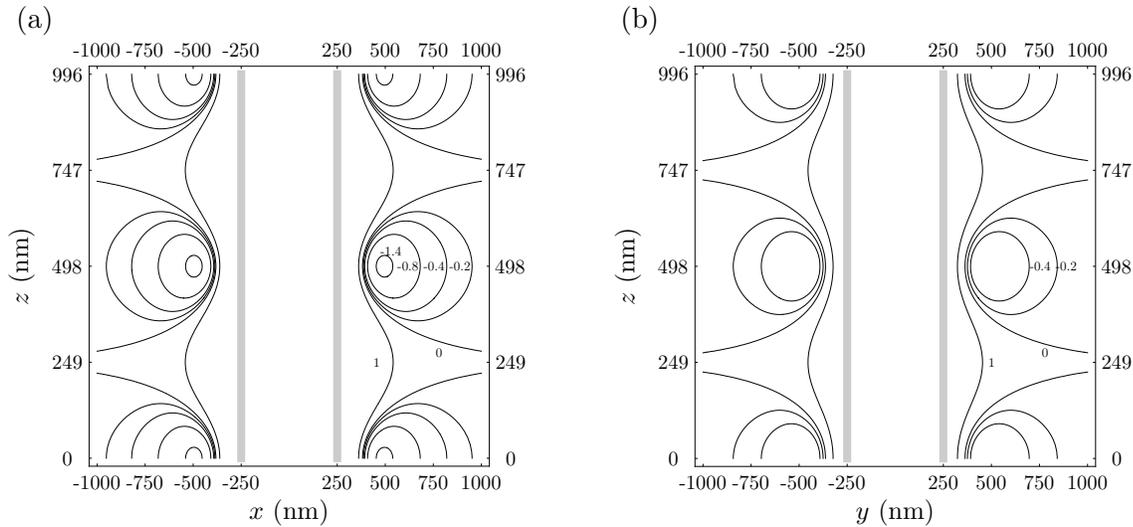
FIGURE 5.3: Contour plot of the trap in the planes $y = 0$ (a) and $x = 0$ (b) for the same parameters as in Fig. 5.2 (black solid). The fibre surface is indicated by the two vertical grey lines and the equipotential lines are labelled in mK.
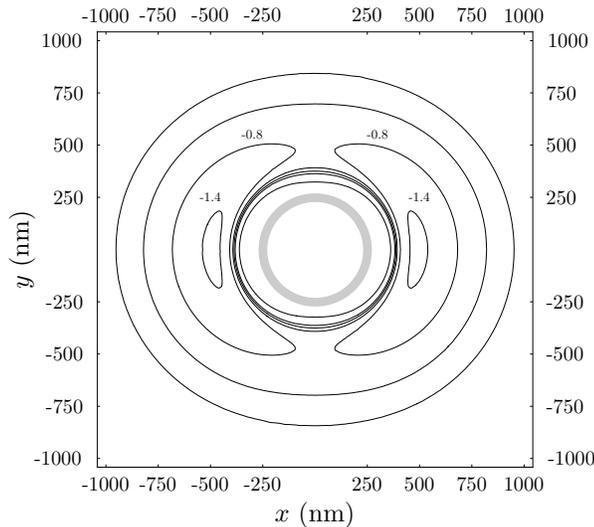
FIGURE 5.4: Contour plot of the trap in the plane $z = 0$ for the same parameters as in Fig. 5.2 (black solid). The fibre surface is indicated by the grey circle. The shown equipotential lines take the values: 1, 0, -0.2, -0.4, -0.8, -1.4, -0.4, and -0.2 mK (from smaller to greater radial position).

state are equally shifted. In the case of circular polarisation the magnetic sub-levels of the ground state undergo a different shift. The light-induced shifts of the energy levels of a Cs atom in a two-colour evanescent field trap can be calculated using Eq. (2.29) from Sec. 2.3.2. For the case of a linearly-polarised external field, the quantisation axis can be set parallel to the electric field and, therefore, π-polarisation can be used for the calculations. Note that in the case of the evanescent field arising around the fibre, this is an approximation valid when $|E|^2 \gg |E_z|^2$.[2] Indeed, $|E_z|^2/|E|^2 \simeq 0.26$ for 780 nm and $|E_z|^2/|E|^2 \simeq 0.17$ for 1064 nm at about 100 nm from the fibre surface along the polarisation direction. The reader should thus bear in mind that the results obtained in this section may deviate from the full calculations to some extent.

Figure 5.5 shows the light shifts of the $6^2P_{3/2}F' = 5$ (upper graphs) and $6^2S_{1/2}F = 4$ (middle graphs) states of a Cs atom in the two-colour evanescent considered in Fig. 5.2 as a function of the distance from the fibre surface in the x- (left column) and y-directions (right column). The shifts of the energy levels produced by the v.d.W. potential have also been taken into account (see Sec. 3.7.2). On the upper graphs the m_F-dependency of the shifts of the excited state becomes apparent. For π-polarised light this dependency is scalar, i. e., the levels with the same value of $|m_F|$ quantum number are degenerate. For the ground state the different magnetic sub-levels are fully degenerate. The frequency shifts of the $6^2S_{1/2}F = 4 \rightarrow 6^2P_{3/2}F' = 5$ excitation transition are shown in the graphs on the bottom (dashed). The frequency shift averaged over the magnetic sub-levels is

---

[2]The z-component of the electric field in the HE$_{11}$ mode is dephased by $\pi/2$ with respect to the transverse component $E_\perp$ (see Eqns. 1.27). Hence, the polarisation is elliptical.

indicated by the solid curve, leading to an average value of ~ 30 MHz for an atom trapped in the evanescent field potential. Note that the values of the ground-state potential predicted by the classical and quantum-mechanical calculations coincide with an accuracy better than 1%.

5.1.2   Circularly polarised fields

The trapping potential created by two circularly polarised fields propagating in the fibre has not yet been experimentally implemented. However, due to the interesting geometry of the trap it will be briefly described here. The trapping potential created in the evanescent field by two circularly polarised laser fields with different frequencies propagating in the fundamental mode of the fibre is given by

$$U(r,z) = \frac{1}{2}(\text{Re}[\alpha_1]|\vec{E}_1(r)|^2 + 4\text{Re}[\alpha_2]|\vec{E}_2(r)|^2 \cos^2[\beta_2 z]) + V_{\text{vdW}}(r). \qquad (5.7)$$

Note that the red-detuned laser ($E_2(r)$) is set in a standing-wave configuration. $|\vec{E}_i(r)|^2$ is the value of the cycle-averaged squared electric field outside the fibre given by Eq. (1.20) and $\text{Re}[\alpha_i]$ the real part of the polarisability of a multilevel atom given by Eq. (2.27). As in the above section, the v.d.W. potential of a planar silica surface $V_{\text{vdW}}(r)$ given by Eq. (3.28) is used. Note that the potential given by Eq. (5.7) is cylindrically symmetric in contrast to the potential created by the linearly polarised fields given by Eq. (5.1).

Figure. 5.6 shows the radial variation of the trapping potential of a ground-state Cs atom in the evanescent field of an ultra-thin optical fibre assuming the same parameters as in Fig. 5.2. Black solid, $P_{780} = 30$ mW of blue-detuned laser light ($\vec{E}_1$) and $P_{1064} = 13$ mW of red-detuned laser light ($\vec{E}_2$). Blue dashed, $P_{780} = 1.2 \times 30$ mW and $P_{1064} = 0.8 \times 13$ mW. Red dotted, $P_{780} = 0.8 \times 30$ mW and $P_{1064} = 1.2 \times 13$ mW.

The trapping potential described by the black solid line has minimum at 237 nm from the fibre surface. The depth of the potential is 1.1 mK. The radial frequency of the trap takes the value $\omega_r/2\pi = 348$ kHz and the extension of the trapping volume along the radial direction for an atom with a kinetic energy corresponding to 100 μK is 100 nm. The trapping potential described by the dashed blue curve has a trap depth of 0.58 mK and the trapping minimum is located at a distance of 313 nm from the fibre surface. Hence, the trap is shallower than the one described by the black solid curve and the trapping minimum has been displaced to larger radial positions. The red dotted curve describes the inverse situation. The trap depth increases to 2.2 mK and the trapping minimum is displaced towards the fibre surface at a distance of 160 nm, however, the repulsive potential created by the blue-detuned laser suffices to maintain a positive valued maximum of the potential separating the atoms from the fibre.

Note that the variation of the laser power is here assumed to be 20% whereas for linearly polarised fields it was considered to be 15%. The cylindrical symmetry of the dipole potential for circular polarisation of the fields better counteracts the v.d.W. potential and the trap is thus more stable against mismatch of the laser powers.
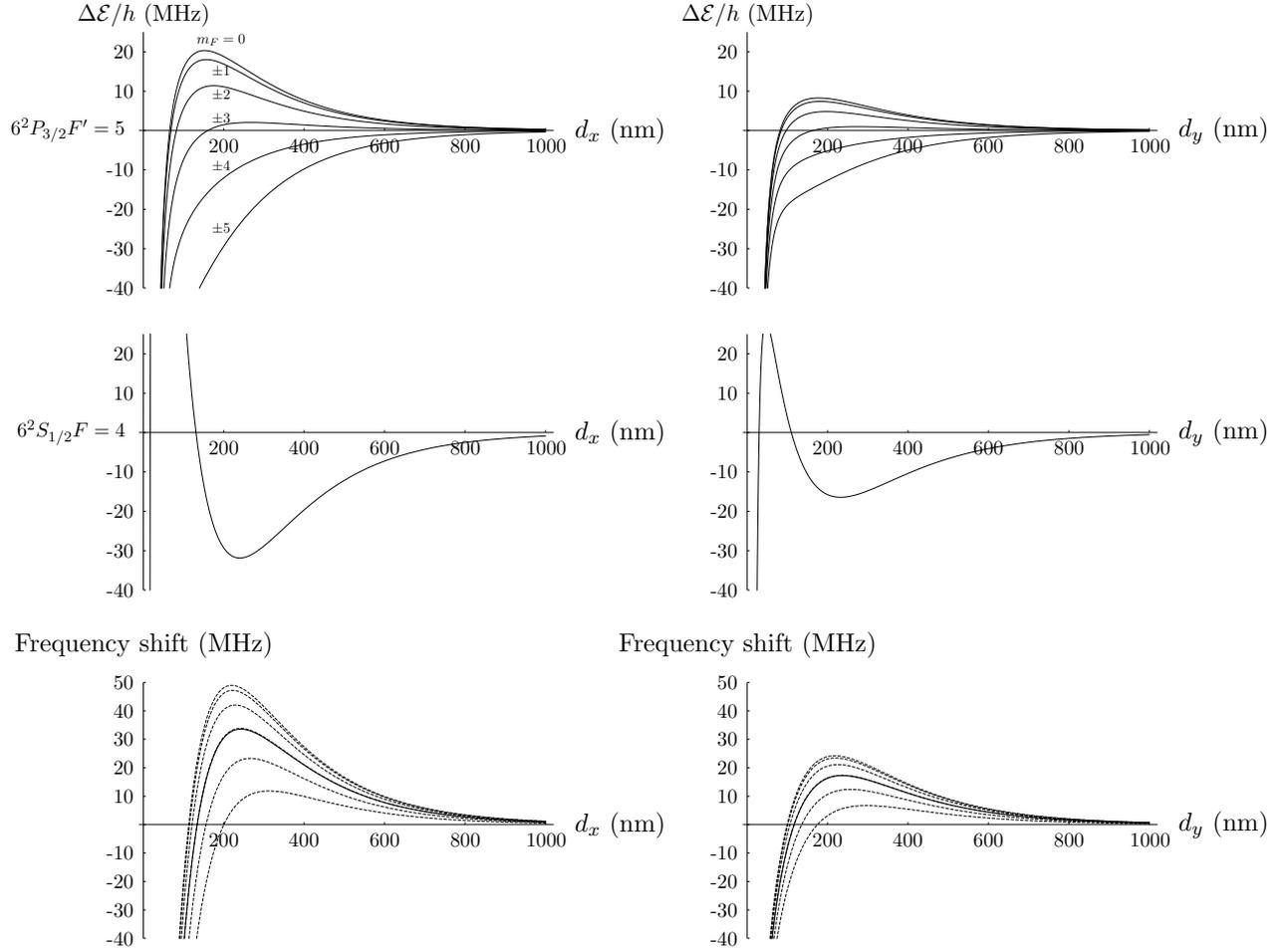
FIGURE 5.5: Frequency shifts induced on the $6^2P_{3/2}F' = 5$ (upper graphs) and $6^2S_{1/2}F = 4$ (middle graphs) states by the two-colour evanescent field as a function of the distance from the fibre surface along the x-axis d_x (left column) and along the y-axis d_y (right column). The labels denote the m_F sub-levels. Bottom: Shift of the $6^2S_{1/2}F = 4 \rightarrow 6^2P_{3/2}F' = 5$ transition frequency (dashed). The solid curve is the average over the m_F sub-levels. The calculations have been performed for the same parameters as in Fig. 5.2. The shifts of the energy levels produced by the v.d.W. potential have also been taken into account (see Sec. 3.7.2).

Figure 5.7 shows the contour plot of the trap in the plane $x = 0$ for the same parameters as in Fig. 5.6 (black solid). The axial oscillation frequency of the trap is calculated to be 553 kHz. The trap size in the axial direction for an atom with a kinetic energy corresponding to 100 μK is 64 nm. The cylindrical symmetry of the potential can be appreciated in the contour plot of the trap in the plane $z = 0$ shown in Fig. 5.8. The trap size in the azimuthal direction can be estimated as $2\pi r_{min} \simeq 3$ μm, where r_{min} denotes the radial position of the trapping minimum. Hence, each of the microtraps has a toroidal shape with an estimated volume of 7.4×10^{-14} cm^3 at the considered temperature of the atoms.

The scattering rates, trap lifetime and coherence time of the atoms in the trap can be calculated using Eqns. (5.4)–(5.6). The scattering rates for the blue- and red-detuned lasers are 15.5 s^{-1} and 2 s^{-1}, respectively. The coherence time is 57 ms and the trapping lifetime is 205 s.

As mentioned in Sec. 5.1.1, the potential created in the evanescent field of two circularly-polarised lasers induces a different energy shift of the magnetic sub-levels of the ground state of the Cs atom. Hence, depending on the polarisation of the fields the magnetic sub-levels of the ground state of the atoms will be differently shifted. In this case, the classical picture is valid as an approximation of the potential averaged over the magnetic sub-levels.

5.2   Experimental Setup

Figures 5.9 and 5.10 show the schematic of the new experimental setup located at the University of Mainz. A list of the labelled elements is given in Table 5.1 together with the section were their description can be found. The most significant changes with respect to the original setup are listed below.

- New elements: The new elements used in the setup are denoted with the symbol * in Table 5.1. The description of those elements can be found in the sections indicated in the table. The new elements that do not provide a significant modification of the setup are not described. These are: Optics (4–10, 18, 25, 26, 34, 43), spectroscopy setups (20 and 21), vacuum measurement and sealants (28, 30, and 42), photodetectors (37).

- Laser setup: The cooling (1), repump (2) and probe (3) lasers are described in Sects. 3.3.1 and 3.4. The two dipole lasers (38, 39) with the corresponding setup to couple them into the polarisation maintaining TOF (17) and to subsequently separate them again are described in Sec. 5.2.2. The TOF is described in Sec. 5.2.1.

- Optical table: The vacuum chamber (11) and the lasers (1–3, 38, 39) are now mounted on the same optical table (see Fig. 5.10). To avoid the coupling of vibrations from the pumps to the lasers, several vibration damping elements (40 and 44) have been installed (see Sec. 3.3.1)
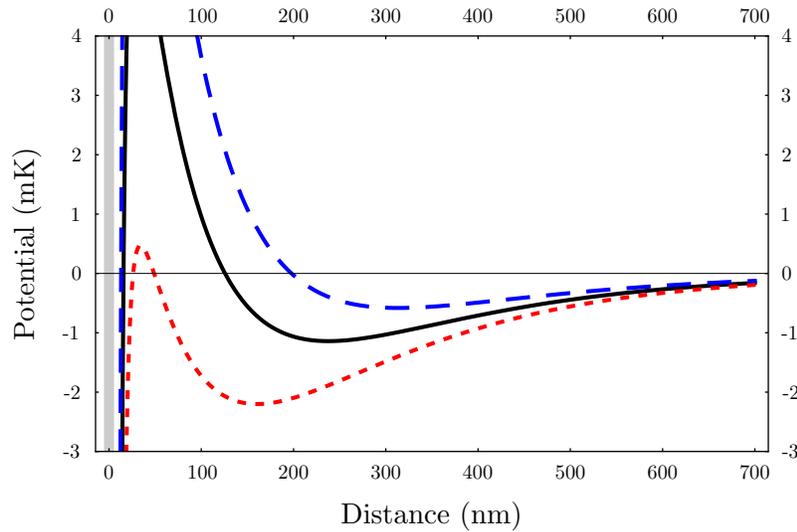
FIGURE 5.6: Variation of the trapping potential given by Eq. 5.7 at $z = 0$ as a function of the distance from the fibre surface. The solid black curve has been calculated assuming $P_{1064} = 13$ mW for the red-detuned laser and $P_{780} = 30$ mW for the blue-detuned laser. The dashed and dotted curves correspond to the mismatched laser powers: Blue dashed line for $P_{1064} = 0.8 \times 13$ mW and $P_{780} = 1.2 \times 30$ mW, and red dotted line for $P_{1064} = 1.2 \times 13$ mW and $P_{780} = 0.8 \times 30$ mW. The surface of the fibre is indicated by the vertical grey line.
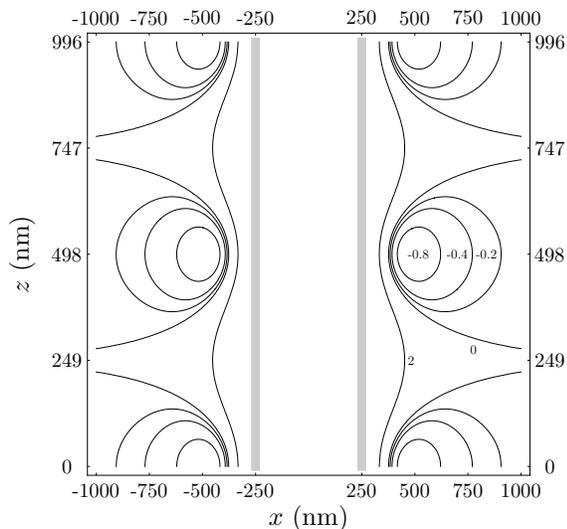
FIGURE 5.7: Contour plot of the trap in the plane $x = 0$ for the same parameters as in Fig. 5.6 (black solid). The fibre surface is indicated by the two vertical grey lines. The equipotential lines are labelled in mK.
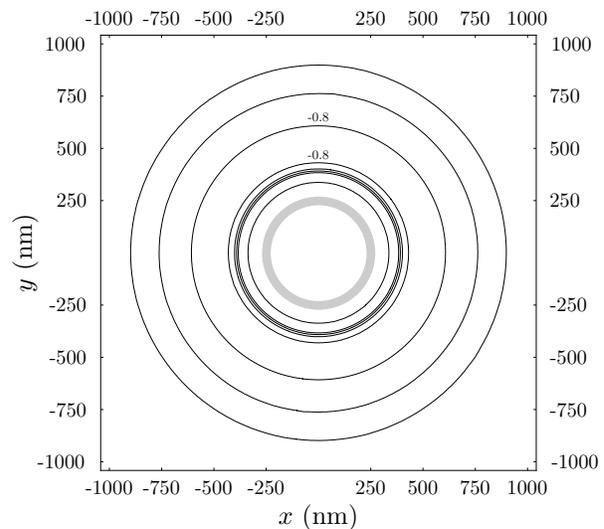
FIGURE 5.8: Contour plot of the trap in the plane $z = 0$ for the same parameters as in Fig. 5.6 (black solid). The fibre surface is indicated by the grey circle. The shown equipotential take the values: 2, 0, -0.2, -0.4, -0.8, -0.8, -0.4, and -0.2 mK (from smaller to greater radial position).

- Fibre cluster (41): The guiding of the lasers from the optical table to the chamber is realised by means of optical fibres that issue from a fibre cluster with the integrated optics necessary for the adjustment of the power and the polarisation of the six MOT beams (see Sec. 3.3.1).

- Frequency control of the MOT beams: The detuning of the cooling and repump lasers is controlled by AOMs (8) in double pass configuration. This is relevant for the efficient loading of dipole traps (see Outlook).

- Laminar flow box: A laminar flow box is located above the vacuum chamber (see Fig. 5.10). This is only used during the installation of the TOF into the vacuum chamber to minimise the risk contamination of the waist of the fibre by dust.

5.2.1   Polarisation maintaining TOF

The creation of a two-colour dipole trap for Cs atoms around an ultra-thin optical fibre requires an optimal control of the polarisation at the waist. For this purpose, a polarisation maintaining (PM) TOF is used. The chosen fibre is a Liekki Passive-10/123-PM with a numerical aperture NA=0.078. The core diameter is 10 μm and the cladding diameter is 123 μm in the untapered region. The target diameter at the waist is 500 nm.

The fibre has a "Panda" structure based on two off-axis stress applying parts (SAP) at each side of the core (see Fig. 5.11). The stress induces a birefringence of $\Delta n = 2.2 \times 10^{-4}$ in the core thereby splitting the two orthogonal polarisation bases into two distinct modes. This is only the case in the untapered region of the fibre because the core does not participate in the guiding at the waist. The effect of the SAP on the guiding properties at the waist is unknown. However, since the cylindrical symmetry is broken the propagation constant of the two polarisation bases will probably be also different there. One might expect that the presence of the SAP at the waist of the fibre modifies the intensity profile of the evanescent field outside the fibre. This is also unknown. However, the SAP, which are usually made of boron-doped silica have a refractive index only about 1% smaller than the refractive index of the cladding and their volume corresponds to approximately 20% to 30% of the total volume of the fibre (see e. g., [89]). Hence, I assume that their effect on the evanescent field can be neglected and that the description of the trapping potentials described in Sec. 5.1.1 holds.

Experimentally, it has been found that for a TOF with a diameter of 500 nm at the waist, the polaristion at the output of the TOF has an eccentricity of $\varepsilon = 0.92$ when the polarisation axis of the input light is parallel either to the slow or the the fast axes of the fibre. The eccentricity is given by

$$\varepsilon = \sqrt{(l_2^2 - l_1^2)/l_2^2}, \tag{5.8}$$
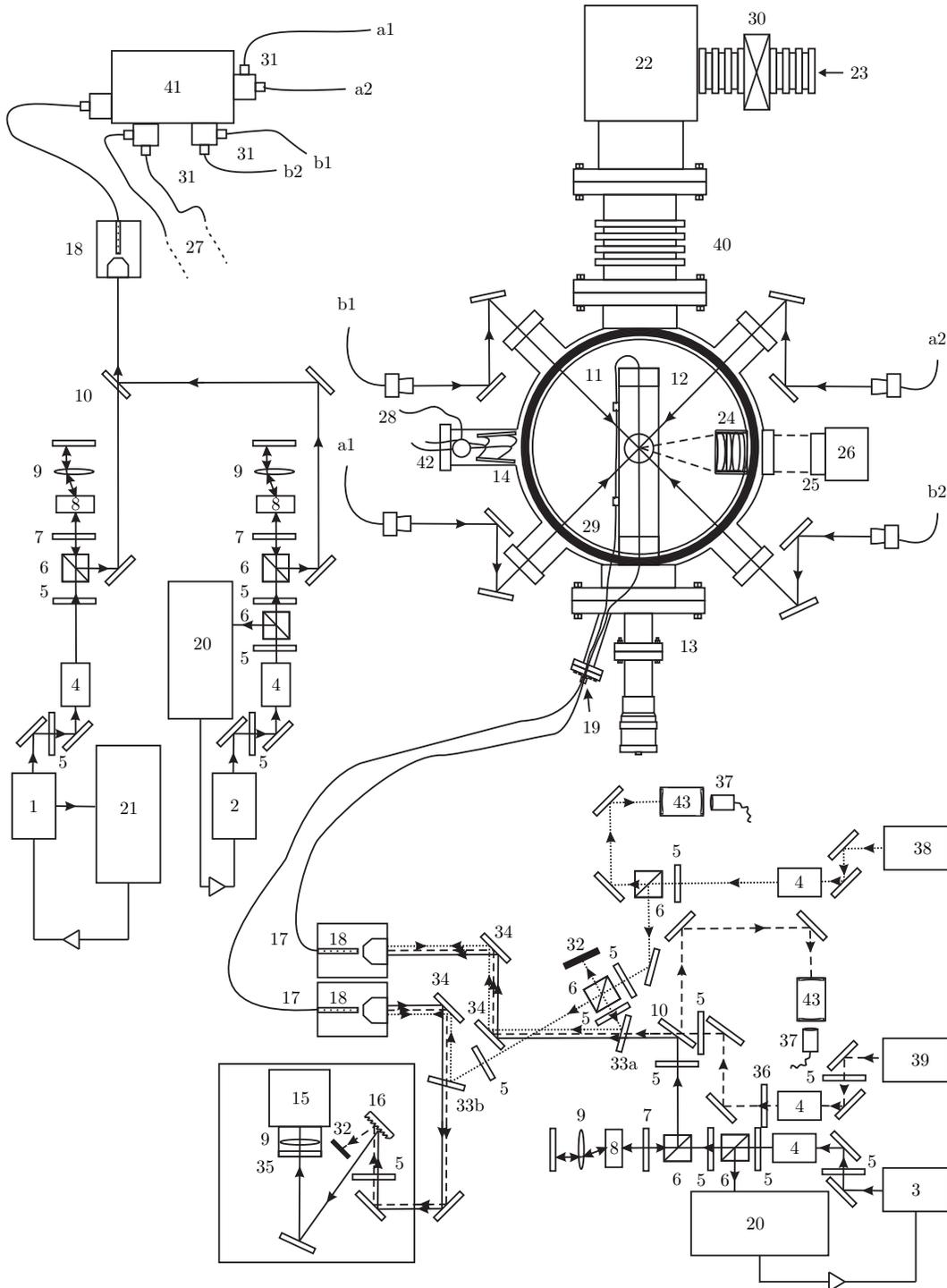
FIGURE 5.9: Schematic of the new experimental setup located at the University of Mainz. The mirrors have not been labelled. The dotted and dashed arrows indicate the path of the red- and blue-detuned laser beams. The solid arrows indicated the probe, cooler and repump laser beams.
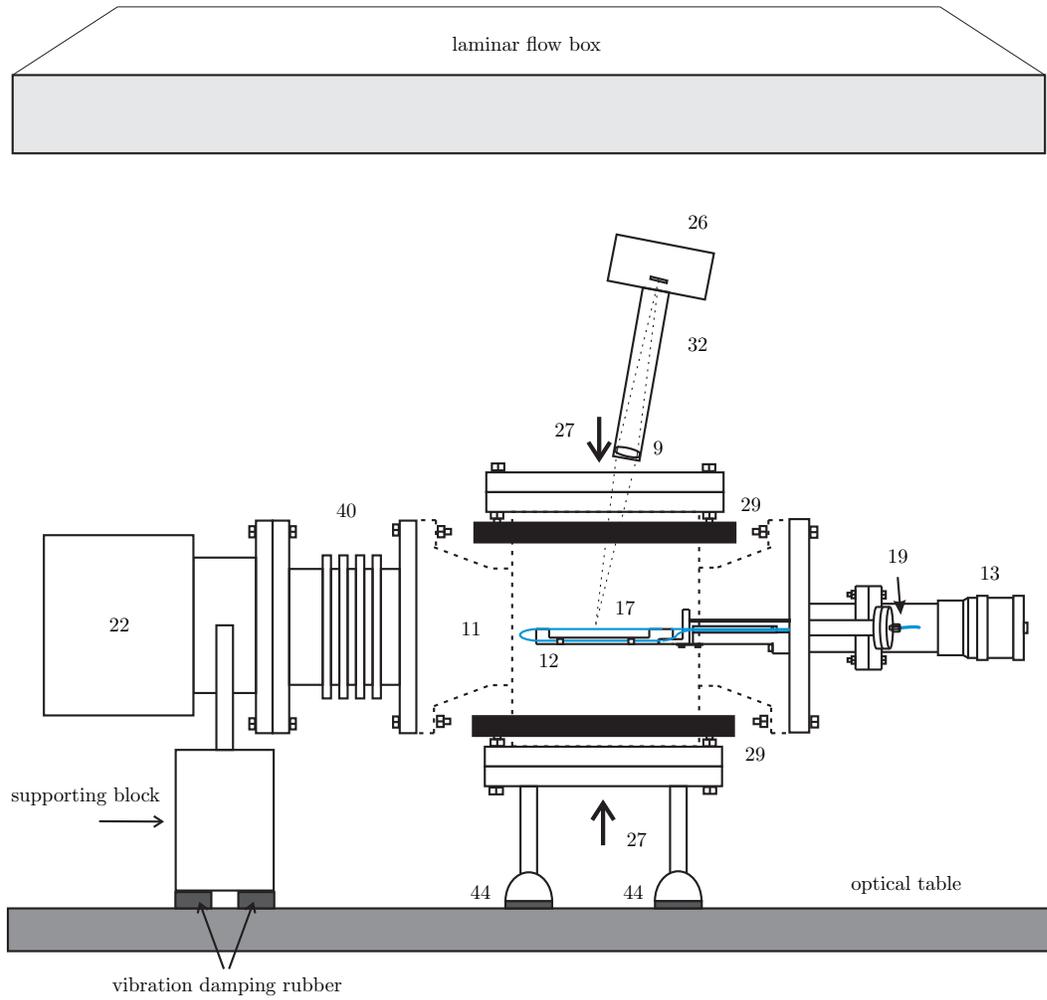
FIGURE 5.10: Schematic of the vacuum apparatus in the new setup located at the University of Mainz.

Number	Description	Section
1	cooling laser*	3.3.1
2	repump laser*	3.3.1
3	probe laser*	3.4
4	Faraday isolator*	–
5	$\lambda/2$ plate*	–
6	polarisation beam splitter*	–
7	$\lambda/4$ plate*	–
8	acousto-optical modulator*	3.4
9	convex lens*	–
10	glass substrate*	–
11	vacuum chamber	3.3.1
12	fibre mount	3.3.2
13	fibre positioner	3.3.2
14	Cs dispensers*	3.3.1
15	avalanche photodiode (APD)	3.4
16	holographic diffraction grating*	–
17	TOF*	5.2.1
18	fibre coupler*	–
19	vacuum feed-through for fibres	3.3.2
20	polarisation spectroscopy setup*	3.3.1
21	saturation spectroscopy setup*	3.3.1
22	turbo-molecular pump with magnetic bearings*	3.3.1
23	pre-vacuum pump*	3.3.1
24	microscope objective	3.3.3
25	camera objective*	3.3.3
26	CCD camera*	3.3.3
27	to vertical MOT beam	3.3.1
28	pressure gauge*	3.3.1
29	magnetic coils	3.3.1
30	vacuum valve*	–
31	polarisation-maintaining optical fibre	5.2.1
32	beam dump	–
33a,b	dichroic mirrors*	5.2.2
34	broad-band mirrors*	–
35	optical band-pass filter*	5.2.2
36	optical low-pass filter*	5.2.2
37	photodetector*	–
38	Nd-YAG laser at 1064 nm*	5.2.2
39	diode laser at 780 nm*	5.2.2
40	vibration damper*	3.3.1
41	fibre cluster*	3.3.1
42	electrical feed-through*	3.3.1
43	Fabry-Perot spectrum analyser*	–
44	Vibration damping mounts*	3.3.1

TABLE 5.1: List of elements labelled in Figs. 5.9 and 5.10.
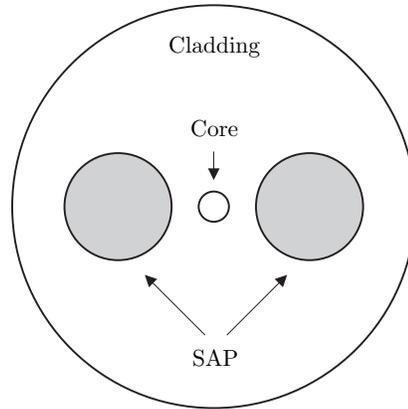
FIGURE 5.11: Schematic of the "Panda" structure of the optical fibre.
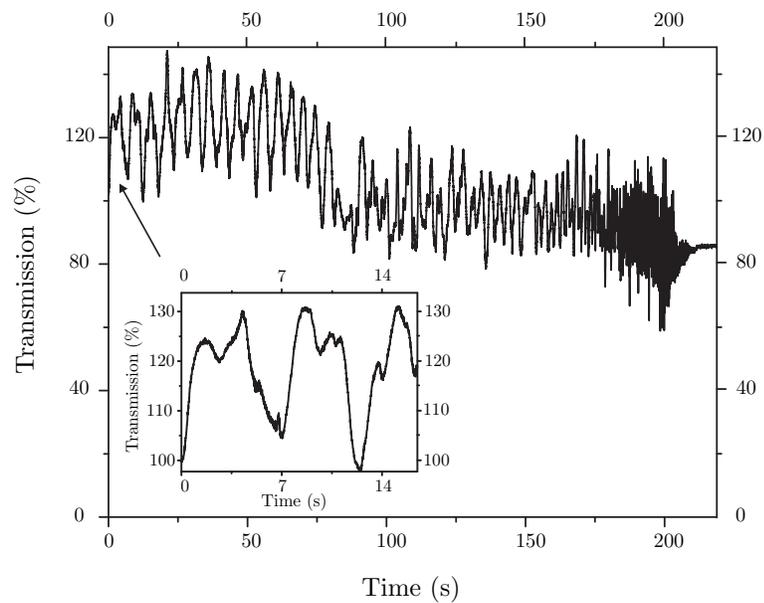
FIGURE 5.12: Transmission through a single-mode polarisation maintaining optical fibre (Liekki Passive-10/123-PM) during the pulling process normalised to the transmission of the untapered fibre. The measurements were done using a 852 nm diode laser.

where l_1 and l_2 are the two axes of an ellipse. This is approximately independent of the wavelength of the transmitted light within a range from 780 to 1064 nm. Moreover, the polarisation axis of the output light remains constant over time scales longer than hours.

Figure 5.12 shows the measured transmission through the PM-fibre during the pulling process. The transmission of the tapered fibre is about 83% of its original value. The inset of the figure shows the variation of the transmission during the first 17 seconds of the pulling process. Note that the transmission oscillates from the very beginning of the pulling process exceeding its original value in about 30% at the maximum. This is due to a bending of the fibre during the pulling process. As it can be deduced from the small numerical aperture, this fibre has a very small refractive index difference between the core and the cladding. Hence, it is specially sensitive to bending. Each of the pulling steps modifies this bending and thereby the transmission through the fibre.

5.2.2 Dipole lasers

- Red-detuned laser: A single-frequency Nd-YAG laser (38) (Spectra Physics EXLSR-1064-800-CDRH) emitting at a wavelength of 1064 nm with 650 mW optical output power is used. The total transmission through a TOF with 500 nm diameter at the waist ranges between 40 and 60 %, including the coupling efficiency at the fibre input.

- Blue-detuned laser: A grating-stabilised diode laser (39) (Toptica LD-780-0150-02) emitting at a wavelength of 780 nm with a maximal output power of 150 mW is used. The transmission through a 500-nm diameter TOF including the coupling efficiency ranges between 60 and 80%.

The setup used for the coupling of the dipole lasers into the optical fibre is shown in Fig. 5.9. The red- (dotted arrows), blue-detuned (dashed arrows) and probe (solid arrows) lasers are combined using a phase-neutral dichroic mirror (Laseroptik) (33a) with a specified reflectivity $R > 99.8\%$ at a wavelength of 1064 nm and a transmission $T > 98\%$ at wavelengths ranging from 780 to 852 nm. The probe (3) and blue-detuned (39) lasers are previously overlapped with a glass substrate (10). The red-detuned laser (38) is also coupled at the other fibre end (17) using a second dichroic mirror (33b). This is also used to separate the Nd-YAG laser from the rest of the lasers. In order to separate the probe from the blue-detuned laser a holographic diffraction grating (16) is used. In addition, a bandpass filter (Thorlabs FB850-40) centred at 850 nm with 40 nm bandwidth (35) is mounted in front of the APD (15). The measured transmission of the filter is 80% at 852 nm and $< 0.01\%$ at 780 nm. In order to eliminate the radiation emitted at 852 nm by the blue-detuned laser, a low-pass filter (Thorlabs FES0800) with a transmission of 80% at 780 nm and $< 0.01\%$ at 852 nm is used (36). With this setup, the background signal detected by the APD lies in the low pW regime, while keeping the overall detection efficiency of the probe laser as high as 60%.

5.3   Experimental results

The influence of the two-colour evanescent field on laser cooled Cs atoms in the vicinity of a 500-nm diameter TOF has been clearly observed. However, the efforts to load the trap using the theoretically calculated parameters of the dipole lasers with atoms that have been previously trapped and cooled in the MOT were so far unsuccessful. The attempts consisted on simultaneously operating the MOT and the dipole trap during several seconds and then measure the transmission of a resonant probe beam a few tenths of milliseconds after switching off the MOT. This failure may be an indication that the process of cooling the atoms in such a surface trap using the molasses of the MOT is inefficient due to the steepness of the potential or due to the presence of the fibre. One possible approach to tackle the problem consists in using an external dipole trap in which the atoms can be cooled and subsequently transferred to the evanescent field surface trap. This will be briefly described in the outlook. In the following, some measurements of the light-induced shifts are presented.

5.3.1   Light-induced shifts

Figure 5.13 shows the measured absorbance profile of the cold atom cloud in the presence of the dipole laser fields described in Sec. 5.2.2. The measurements have been performed using the experimental sequence shown in Fig. 3.13 of Sec. 3.5.1 with the dipole lasers in continuous operation. The probe laser is launched through the fibre simultaneously with the red-detuned laser alone (red-dashed), with the blue-detuned laser alone (blue-dotted), and with both dipole lasers (black solid). The chosen parameters for the lasers are: 53 pW for the probe laser, 3 mW for the red-detuned laser (Nd-YAG at 1064 nm) and 1.8 mW for the blue-detuned laser (diode laser at 780 nm). The three lasers had the same polarisation (linear) and were coupled as a running wave. The point of zero detuning has been fitted to the maximal absorbance of the cloud in the presence of both dipole lasers. Note that the powers used for the dipole lasers are low compared to the powers necessary for operating the trap. It has been observed that the linewidths become broader for increasing powers of the trapping fields. At powers larger than 1 to 5 mW the maximal absorbance decreases to a point where the absorbance profiles are not measurable using this method. This broadening can be explained by the light-shifts of the atomic transition frequency which depend on the magnetic sub-levels of the excited state (see Figs. 5.5). Since the atomic population is distributed among all the magnetic sub-levels, this results in an inhomogeneous broadening of the absorbance profile. The measured linewidths of the absorbance profiles are $\sim$10 MHz (black solid), $\sim$11 MHz (blue dotted), and $\sim$12 MHz (red dashed). Using Eqns. (2.23) and (2.27) it can be shown that the maximal dipole force induced by the probe laser with 53 pW is one to two orders of magnitude smaller than the dipole force induced by the red- and blue-detuned laser fields with a few mW of power. Hence, no significant narrowing of the profiles due to variations of the density of the atom cloud during the spectroscopy occurs in this case.
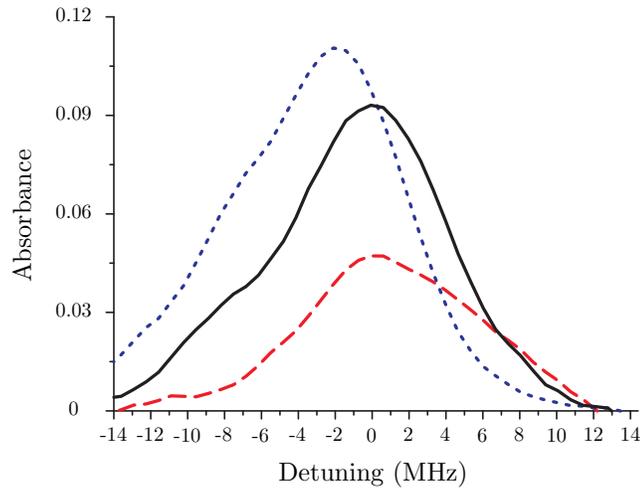
FIGURE 5.13: Measured absorbance of the cold atom cloud as a function of the detuning of the probe laser for three configurations of the dipole fields: 1.8 mW of the blue-detuned laser light (blue dotted), 3 mW of the red-detuned laser light (red dashed), 1.8 and 3 mW of the blue- and red-detuned laser light, respectively (black solid). The power of the probe laser was set to 53 pW.

The absorbance of the cloud in the presence of the red-detuned dipole field (red dashed) is clearly asymmetric. The integrated absorbance for positive values of the detuning is larger than the integrated absorbance for negative values. This is due to the light-induced shift of the excitation transition of the atoms produced by the red-detuned laser. As shown in Fig. 2.3 of Sec. 2.3.2 a Cs atom interacting with a red-detuned light field at a wavelength of 1064 nm undergoes a frequency shift of the atomic levels. The energy of the ground state $6^2S_{1/2}F = 4$ is lowered and the energy of the excited state $6^2P_{3/2}F' = 5$ is rised (averaging over the magnetic sub-levels). Hence, the frequency of the atomic transition increases in the presence of the red-detuned dipole laser. One could expect that this produces a shift in the curve but not necessarily an asymmetry of the profile. Indeed, the asymmetry stems from the fact that the atoms closer to the fibre undergo a larger light-shift of the transition frequency and at the same time have a higher contribution to the absorbance. The latter stems from the intensity profile of the evanescent field of the probe laser, which decays (quasi) exponentially outside the fibre. A blue-detuned light field produces the opposite effect (see Fig. 2.3). This can be appreciated in the dotted curve showing the absorbance profile of the cloud in the presence of the blue-detuned laser.

The peak absorbance of the profile measured in the presence of the blue-detuned laser is larger than in the other two cases. This might be due to the smaller decay length of the evanescent field of the 780-nm laser and due to the lower laser power compared to the red-detuned laser.

The profiles shown in Fig. 5.13 can now be compared to the profile in the absence of

dipole fields. Such a measurement has not been performed with the new setup. For the purpouse of the comparison, the reader is referred to Fig. 3.31 (b) from Sec. 3.8 where a measurement for a probe laser power of 52 pW performed with the original setup is shown. The peak absorbance is 0.23 and the linewidth 7.3 MHz. While the peak absorbance is greater than the peak absorbance of the profiles shown in Fig. 5.13, the linewidth is narrower. As mentioned above, this broadening of the profiles in the presence of the red- and blue-detuned laser fields stems from the inhomogeneous broadening produced by the different shifts of the Zeeman sub-levels. Note that the comparison is only qualitative since the experiments were performed with different fibres, Newport FS-F for Fig. 3.31 and Liekki Passive-10/123-PM for Fig. 5.13. Nevertheless, it has been observed that the absorbance profiles measured with the two fibres in the absence of the dipole laser fields are comparable.

The measurements presented in this section show a clear influence of the two-colour evanescent field on the spectral properties of laser cooled Cs atoms. A further analysis of the absorbance profiles using the simulations described in Sec. 3.7.3 including the two-colour evanescent field may also prove the mechanical influence of the dipole lasers on the atoms.

Conclusions

In this thesis I investigated the interaction of laser cooled caesium atoms with the evanescent field arising around ultra-thin optical fibres with diameter smaller than the guided light. The ultra-thin optical fibres are produced by tapering a standard telecommunication optical fibre with the custom-made tapering facility available in our group [36]. In the first part of this thesis I extensively analysed the guiding properties of such fibres. The knowledge of the propagation properties of the guided fibre modes is essential for using them as a tool to investigate cold atoms. Moreover, such modes are of high interest by themselves exhibiting characteristics not found in free propagating beams. The discontinuity of the intensity at the fibre surface and the strong confinement of the electric field are two examples of that [37].

I developed an experiment that allows to spectroscopically investigate a cloud of laser cooled atoms using a tapered-optical fibre (TOF). By overlapping a magneto-optical trap (MOT) with the waist of a TOF the transmission of a frequency scanned probe laser launched through the fibre was measured in the presence of the atoms. In order to accurately analyse the interaction of the atoms with the evanescent field of the fibre I developed a theoretical model that describes the absorbance profiles of the atom cloud as a function of the frequency of the probe laser. The model includes a detailed analysis of the density of the atom cloud in the vicinity of the fibre using Monte-Carlo simulations of the atomic trajectories inside the cloud. The results of this analysis were confirmed in a recent publication using a different approach [90]. The modelling of the absorbance profiles revealed the importance of two effects that strongly influence the atoms both spectrally and mechanically: The light-induced dipole forces and the surface interactions.

I also showed that ultra-thin optical fibres can be used as an efficient tool to measure the fluorescence of the cold atom cloud. The efficiency of this method relies on the interaction of the atoms with the fibre leading to an enhancement of the atomic spontaneous emission rate into the guided fibre mode.

During the last year and a half of my graduate work I built a new experimental setup at the University of Mainz that allows to couple two additional dipole lasers into the TOF. I also experimentally solved the problem of fabricating fibres that do not fuse when a laser with a power of several milliwatts is launched through it. This is an indispensable condition to create the two-colour evanescent field dipole traps described

in this thesis. The spectral influence of the two-colour evanescent field on the atoms was spectroscopically investigated. The light-shifts of the energy levels of the atoms induced by the dipole lasers were clearly observed by measuring the absorbance profile of the atom cloud.

As a concluding remark, this thesis demonstrates that ultra-thin optical fibres are an efficient tool to enhance light-matter interaction in two directions: Guided photon to atom and atom to guided photon. In a long-term perspective, this enhanced interaction can be used in combination with the atom manipulation technologies to prepare ensembles of fibre-coupled atoms. For this purpouse, the first steps towards atom trapping and manipulation around ultra-thin fibres have already been done.

Chapter 6

Outlook

In this Chapter I present the actual status of the experiment and briefly describe the latest measurements that have been performed towards the direction of atom trapping and manipulation using the evanescent field of a TOF (Sec. 6.1). In the last Section a novel type of evanescent field surface trap that allows atom trapping in the dark, thereby suppressing the light shifts of the energy levels is described (Sec. 6.2).

6.1 External dipole trap to approach the atoms to the fibre

Due to the difficulties of loading the atoms into the surface microtraps presented in Sec. 5.1.1, an external dipole trap creating a purely attractive potential for Cs atoms has been set up. The atoms are loaded into the external dipole trap which is overlapped with the fibre waist and, as a next step, an adiabatic transfer of the atoms into the evanescent field dipole trap should be possible [91].

Figure 6.1 schematically shows the setup for the external dipole trap. A red-detuned laser beam (Nd-YAG, (3)) with Gaussian profile at a wavelength of 1064 nm is tightly focused inside the vacuum chamber (13) through the microscope objective (7). The laser is transmitted through a PM single-mode optical fibre (2) and overlapped with the lateral imaging system (see Sec. 3.3.3) using a polarisation beam-splitter (PBS) (6). A band-pass filter for 850 nm (see Sec. 5.2.2) is used to remove the scattered light from the dipole beam that would otherwise saturate the CCD-chip. The power of the laser beam is 320 mW. The beam radius at the focus is calculated to be 7 μm, leading to a depth of the potential of 700 μK at the trapping minimum (11). The focal point of the beam is overlapped with the MOT (12). An imaging beam (9) is coupled through a view-port underneath the chamber. The beam goes upwards through the centre hole of the mount (8) to the MOT. The atom cloud absorbs part of the light of the imaging beam creating a shadow. The shadow is then imaged with a $2f - 2f$ imaging system ((1) and (14)).
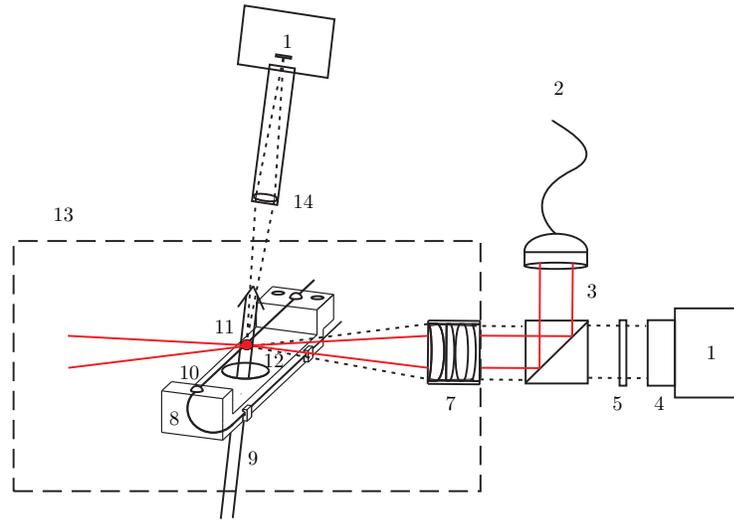
FIGURE 6.1: Experimental setup used for the external dipole trap. Labels: 1 CCD-camera, 2 PM-fibre, 3 Nd-YAG laser, 4 camera objective, 5 band-pass filter, 6 PBS, 7 microscope objective, 8 fibre mount, 9 imaging beam, 10 TOF, 11 dipole trap, 12 MOT, 13 vacuum chamber, 14 convex lens.

Table 6.1 shows the experimental sequence used to load the dipole trap and image the atoms. The described sequence has been optimised by using a method of trial-error. There are other combinations of the parameters that lead to an efficient loading of the trap. In the first period of 3 s the atoms are trapped and cooled in the MOT. The parameters used for the MOT beams and the magnetic field gradient are shown in the Table. During the next period of 120 ms the dipole trap is loaded. The dipole beam is switched on and the dipole trap therefore operates simultaneously with the MOT. The power and the detuning of the MOT beams vary as a function of time during this period. The chosen characteristic time of the variation is 80 ms. The magnetic field gradient maintains its original value. In the next period a time-delay of 60 ms is introduced where the MOT beams and the magnetic field are off. During this period the atoms from the MOT that are not trapped in the dipole potential are released. Hence, the duration of the delay must be longer than the time it takes the atoms released from the MOT to leave the region of the dipole trap $\sim$10 ms. In the last period an absorption image of the atoms is recorded during an integration time of 40 μs. The power of the imaging laser is set to 90 μW and the $1/\sqrt{e}$-radius of the beam is $\sigma = 1.5$ mm. During this period the dipole beam is off in order to eliminate the light shifts of the energy levels.

Figure 6.2 shows the absorption image of the atom cloud released from the external dipole trap. The measurement was performed using the sequence described in Table 6.1. Note that the extension of the atom cloud along the x-direction is about the same as for the MOT. The dimensions of the cloud are estimated to be 1 mm along the x-axis

	MOT loading	dipole trap loading	delay	imaging
time duration	3 s	120 ms	60 ms	40 μs
cooling laser	$P_0 = 150$ mW, $\delta_0 = -\gamma$	$P(t) = (P_0/3) + (2P_0/3)\exp\left[-t/(80\text{ ms})\right]$, $\delta(t) = \delta_0(10 - 9\exp\left[-t/(80\text{ ms})\right])$	off	off
repump laser	$P_0 = 160$ μW, $\delta_0 = 0$	$P(t) = P_0 \exp\left[-t/(80\text{ ms})\right]$, $\delta = 0$	off	off
magnetic field gradient	8 Gauss/cm	8 Gauss/cm	off	off
Nd-YAG	off	$P = 320$ mW	$P = 320$ mW	off
imaging laser	off	off	off	$P_0 = 90$ μW $\sigma = 1.5$ mm

TABLE 6.1: Experimental sequence for the loading of atoms in the dipole trap and subsequently image them. The power P and detuning of the lasers in each of the steps are shown.
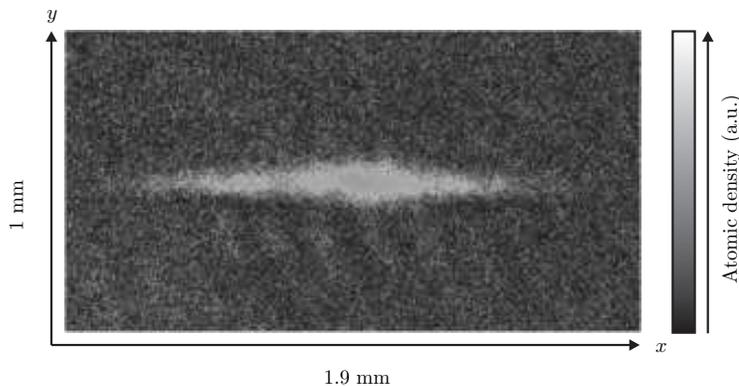
FIGURE 6.2: Absorption image of the atoms released from the dipole trap. The absorption image was taken with a 40 μs integration time.

and 0.15 mm along the y-axis.

By overlapping the dipole trap with the waist of the fibre, the interaction of cold atoms with the surface of the fibre can be systematically investigated [92]. Moreover, when coupling the dipole beams described in Sec. 5.2.2 into the fibre, the lifetime of the atoms in the trap as a function of the parameters of the guided dipole beams can be measured. Finally, an adiabatic transfer of the atoms trapped in the external dipole trap into the two-colour evanescent field dipole trap should be possible [91].

6.2   Blue-detuned evanescent field traps based on two-mode interference

We have recently proposed a novel concept of blue-detuned evanescent field surface traps for cold neutral atoms based on two-mode interference in ultra-thin optical fibres [93]. When two or more transverse modes with the same frequency co-propagate in the fibre, their different phase velocities cause a stationary interference pattern to establish. Intensity minima of the evanescent field at any distance from the surface can be created and an array of optical microtraps can thus be obtained around the fibre. In this section, I discuss one possible combination of two low order modes, the HE_{11} and the TE_{01}, yielding a trap at one to two hundred nanometres from the fibre surface which, using a few ten milliwatts of trapping laser power, has a depth on the order of 1 mK and a trapping lifetime exceeding 100 seconds for Cs atoms.

6.2.1   Modal dispersion and polarisation configuration

Let us assume a fibre-field configuration where only four modes can propagate: The fundamental mode HE_{11} and the first three higher order modes, the TE_{01}, the TM_{01} and the HE_{21}. Assuming that the modes can be pairwise excited, three pairs of modes can be used to trap cold neutral atoms in the intensity minima formed at the positions of destructive interference in the evanescent field surrounding the fibre. These combinations are $HE_{11}+TE_{01}$, $HE_{11}+HE_{21}$ and $TE_{01}+HE_{21}$.[1] Here, I will only discuss the trap resulting from the interference between the HE_{11} and TE_{01} modes. The other combinations can be found in [93].

Figure 6.3 shows the propagation constant β for the first seven modes in the fibre normalised to the wavenumber in free space k_0 as a function of the V parameter given by Eq. (1.14) in Sec. 1.2. The dashed vertical line located at $V = 3.11$ indicates the value of the V parameter for the configuration considered here: An ultra-thin optical fibre of pure silica ($n_1 = 1.452$) with a radius $a = 400$ nm, surrounded by vacuum ($n_2 = 1$) and a wavelength of $\lambda = 850.5$ nm. At this value of V the phase velocities of the four modes that can propagate differ significantly. This difference will cause an interference pattern to establish along the fibre and, in addition, results in different radial decay lengths of the evanescent field outside the fibre for each mode. The modal dispersion can therefore be used to create a tailored evanescent field resulting from the interference of two or more co-propagating modes. One blue-detuned neutral atom trap using two co-propagating modes exhibits three-dimensional confinement: Radially, due to the tailored evanescent field, axially, due to the difference in the phase velocity, and

---

[1]The TM_{01} mode cannot be used to create a trap: The necessary degree of cancellation of the electric field at the position of destructive interference only occurs if the polarisation in both modes matches reasonably good. Since the projection of the electric field on the propagation axis z for the TM_{01} mode is much larger than for the rest of the considered modes the TM_{01} mode does not have the necessary degree of polarisation matching with the rest of the modes to form a useful trap.
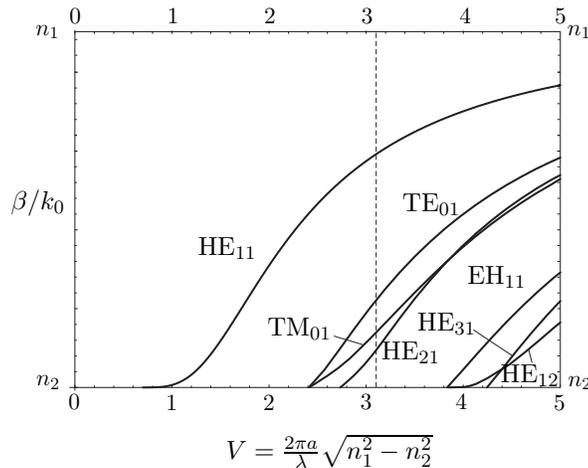
FIGURE 6.3: Normalised propagation constant β/k_0 versus the V parameter. The dashed vertical line located at $V = 3.11$ indicates the configuration considered in this section.

azimuthally, because the different modes have different polarisation distributions around the fibre axis.

Figures 6.4 and 6.5 show the vector plots of the electric field component transverse to the fibre axis $\vec{E}_\perp = (E_x, E_y)$ at $t = 0$ and $z = 0$ propagating in the HE_{11} and TE_{01} modes, respectively. The HE_{11} mode is assumed to be x-polarised and is given by Eqns. (1.26) and (1.27) in Sec. 1.2.2 with φ_0 set to zero. The TE_{01} mode is given by Eqns. (1.30) and (1.31) in Sec. 1.2.4. The decay lengths of the two modes in the considered configuration are $\Lambda_{11} = 164$ and $\Lambda_{01} = 277$ nm, respectively.

6.2.2 $HE_{11}+TE_{01}$ trap

As an example, I discuss the properties of the trap resulting from the interference between the HE_{11} and TE_{01} modes for Cs atoms. By choosing the appropriate power distribution between the modes, an array of local minima of the field intensity at any distance from the fibre surface can be created at the positions where the two fields optimally cancel. For blue-detuned light with respect to the atomic transition frequency a dipole force proportional to the negative gradient of the field intensity is then exerted on the atoms confining them in the intensity minima (see Sec. 2.3).

The trap can be created with 50 mW of light and the fibre-field parameters described above. With 72% of the power propagating in the HE_{11} mode and 28% in the TE_{01} mode, a trap for cold Cs atoms with a trapping minimum at 134 nm from the fibre surface is formed. The depth of the trap is 0.92 mK and the trapping lifetime resulting from heating due to spontaneous scattering of photons exceeds 100 seconds for Cs atoms with an initial kinetic energy corresponding to 100 μK.
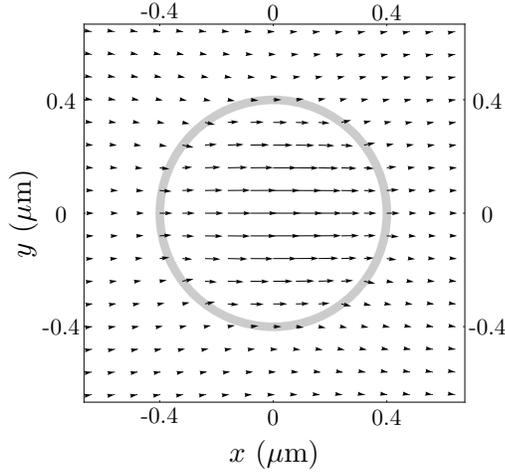
FIGURE 6.4: Field plot of the electric field component perpendicular to the fibre axis $\vec{E}_\perp = (E_x, E_y)$ for the HE$_{11}$ mode at $t = 0$, $z = 0$ and for $\varphi_0 = 0$ (see Eqns. (1.26) and (1.27)). The fibre is indicated by the grey circle. The following parameters have been used: $a = 400$ nm, $n_1 = 1.452$, $n_2 = 1$, and $\lambda = 850.5$ nm.
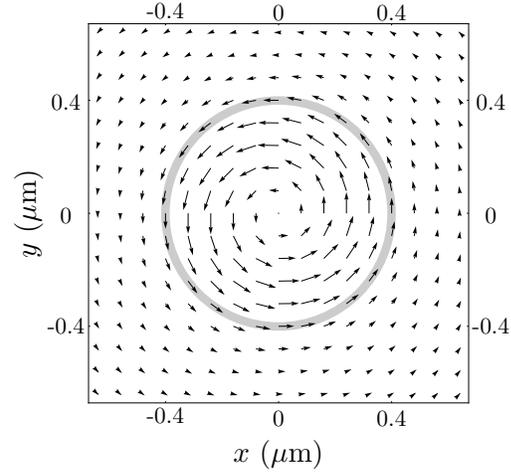
FIGURE 6.5: Field plot of the electric field $\vec{E}$ for the TE$_{01}$ mode at $t = 0$ and $z = 0$ (see Eqns. (1.30) and (1.31)). The fibre is indicated by the grey circle. The fibre parameters are identical to Fig. 6.4.

Figure 6.6 shows a contour plot of the trapping potential including the van der Waals (v.d.W.) surface potential in the plane $z = 4.61$ μm (Eq. (3.28) in Sec. 3.7.2). The fibre surface is indicated by a grey circle and the equipotential lines are labelled in mK. The trapping minimum is located at $\phi = \pi/2$, $r = 534$ nm and $z = 4.61$ μm. The trapping minimum lies on the y-axis because here the polarisation of the two modes matches and the interference is maximally destructive. This polarisation matching between the two modes can be understood when comparing Figs. 6.4 and 6.5.

The contour plot of the trapping potential in the plane $x = 0$ is shown in Fig. 6.7. The fibre surface is indicated by two vertical grey lines. The interference between the modes creates an array of traps in the axial direction with a periodicity given by the beat length of the two co-propagating modes, $z_0 = 2\pi/(\beta_{11} - \beta_{01}) = 4.61$ μm. In addition, there is a second array of traps on the opposite side of the fibre with same periodicity which is shifted by $z_0/2$. The potential has a $\sin^2((\beta_{11} - \beta_{01})z)$ dependence in the axial direction.

Figure 6.8 shows the trapping potential along the y-axis. The fibre surface is indicated by the vertical grey line. The solid black line corresponds to the sum of the light-induced potential and the v.d.W. potential when 72% of the power propagates in the HE$_{11}$ mode. The dashed and dotted lines correspond to the same potential assuming slightly different power distributions between the modes: The parameter τ is defined such that $P_{11} = \tau P$ and $P_{01} = (1 - \tau)P$, where P denotes the total power transmitted through the fibre, P_{11} the power propagating in the HE$_{11}$ mode, and P_{01} the power propagating in the

TE$_{01}$ mode. I assume that τ can be controlled with a precision of $\sigma = 0.05\sqrt{\tau_0(1-\tau_0)}$, i. e., $\sigma = 0.025$ for $\tau_0 = 0.5$. For the case of $\tau_0 = 0.72$ the power distribution between the modes τ would then be controlled within ± 0.022. This value is considered to be a conservative assumption for the precision of the power distribution between the two modes. For the case of $P_{11} = (\tau_0 + \sigma)P$ (dotted line) the trap is 27% shallower compared to the trap for $P_{11} = \tau_0 P$ (solid line), whereas for the case of $P_{11} = (\tau_0 - \sigma)P$ (dashed line) the trap is 30% deeper. While the trap depth increases when decreasing τ, the trapping minimum is also shifted towards the fibre. When further decreasing τ the depth of the trap thus drastically reduces because the v.d.W. potential becomes larger than the light-induced potential. Furthermore, the potential barrier in the direction towards the fibre becomes narrower which would eventually lead to tunnelling of the atoms. The parameters presented here have been chosen in such a way that even with realistic experimental uncertainties the trap remains sufficiently deep and the tunnelling is negligible compared to the trapping lifetime. Note that the total potential is slightly negative at its minimum due to the influence of the v.d.W. potential. Since the z-component of the electric field in the HE$_{11}$ mode vanishes at $\phi = \pi/2$, the polarisation in the two modes perfectly matches at the intensity minimum and the v.d.W. potential at this position is the only influence on the atoms.

Using a harmonic potential approximation the trapping frequencies can be calculated. These are: $\omega_\phi/2\pi \approx 1.07$ MHz in the azimuthal direction, $\omega_z/2\pi \approx 528$ kHz in the axial direction, and $\omega_r/2\pi \approx 770$ kHz in the radial direction. The extensions of the trapping volume in this directions for Cs atoms with a kinetic energy corresponding to 100 μK are: 34 nm, 68 nm, and 47 nm, respectively.

The calculations of the lifetime have been performed assuming Cs atoms with an initial kinetic energy equivalent to 100 μK trapped in a three dimensional classical harmonic potential with oscillation amplitudes corresponding to the above given extensions of the trapping volume. From that, the mean squared field amplitude at the position of the atom has been calculated by integrating over all possible classical oscillation modes. Using this method, a scattering rate of 39 photons/second and a trapping lifetime of 108 seconds is found.
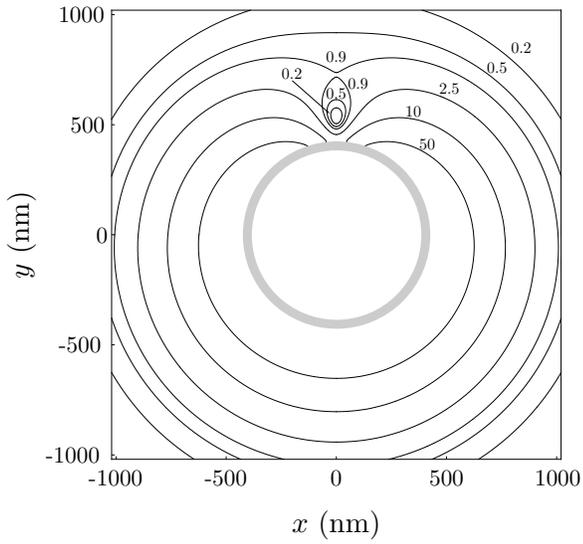
FIGURE 6.6: Contour plot of the $HE_{11}+TE_{01}$ trap for Cs atoms in the plane $z = 4.61$ μm for the following parameters: $P = 50$ mW, $\tau = 0.72$, $\lambda = 850.5$ nm, $a = 400$ nm, $n_1 = 1.452$, and $n_2 = 1$. The fibre surface is indicated by the grey circle and the equipotential lines are labelled in mK.
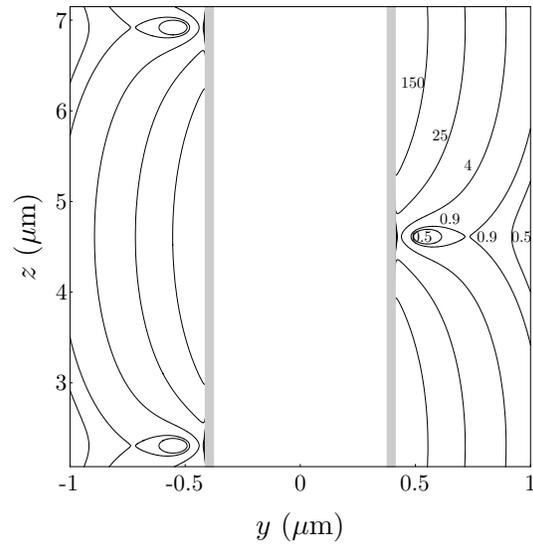
FIGURE 6.7: Contour plot of the $HE_{11}+TE_{01}$ trap in the plane $x = 0$ for the same parameters as in Fig. 6.6. The fibre surface is indicated by the two vertical grey lines and the equipotential lines are labelled in mK.
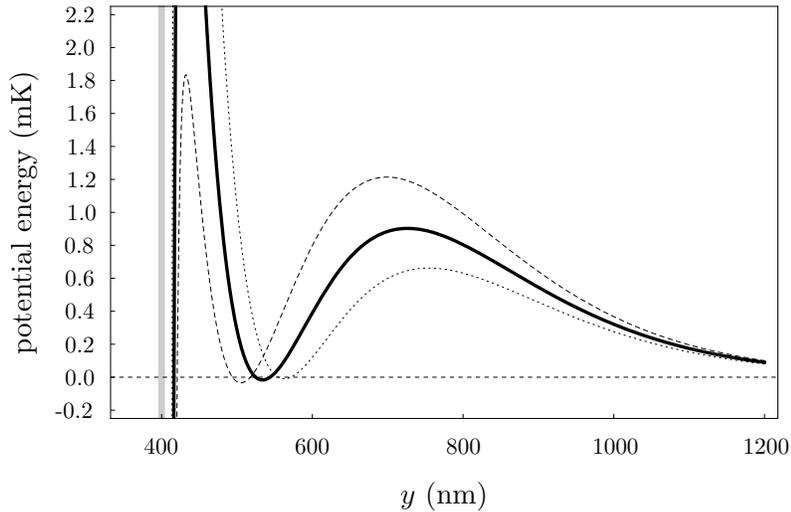
FIGURE 6.8: Plot of the trapping potential versus the position along the y axis for $P_{11} = \tau_0 P$ (solid line), $P_{11} = (\tau_0 + \sigma)P$ (dotted line) and $P_{11} = (\tau_0 - \sigma)P$ (dashed line). The parameters are the same as in Fig. 6.6. The fibre surface is indicated by the vertical grey line. See text for details.

Appendix A

Maxwell's equations in a step-index circular optical fibre
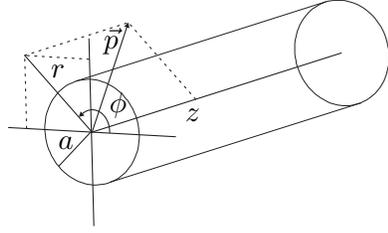
$$n(r) = \begin{cases} n_1 & \text{if } r < a \\ n_2 & \text{if } r > a \end{cases} \text{ with } n_1 > n_2 \tag{A.1}$$

FIGURE A.1: Geometry of the fibre and variation of the refractive index as a function of r

This appendix is dedicated to solve the Maxwell's equations in an optical fibre. The the refractive index n as a function of r is given by Eq. (A.1), where a denotes the fibre radius, n_1 the refractive index inside the fibre, and n_2 the refractive index in the surrounding medium. For simplicity, we use cylindrical coordinates. The Maxwell's equations are given by [29]

$$\vec{\nabla} \times \vec{H} = \varepsilon(r)\frac{\partial \vec{E}}{\partial t}, \tag{A.2}$$

$$\vec{\nabla} \times \vec{E} = -\mu_0\frac{\partial \vec{H}}{\partial t}, \tag{A.3}$$

$$\vec{\nabla} \cdot (\varepsilon(r)\vec{E}) = 0, \tag{A.4}$$

$$\vec{\nabla} \cdot \vec{H} = 0. \tag{A.5}$$

$$\tag{A.6}$$

From Eqns. (A.2)–(A.5), the wave equation of the fields

$$\vec{\nabla}^2\vec{E} - \mu_0\varepsilon(r)\frac{\partial^2 \vec{E}}{\partial t^2} = -\vec{\nabla}(\frac{\vec{E}}{\varepsilon(r)} \cdot \vec{\nabla}\varepsilon(r)) \tag{A.7}$$

can be deduced. Firstly, we apply the curl operation on Eq. (A.3) and use the relation $\vec{\nabla} \times (\vec{\nabla} \times \vec{E}) = \vec{\nabla}(\vec{\nabla} \cdot \vec{E}) - \nabla^2 \vec{E}$. Secondly, we use Eqns. (A.2) and (A.4) to simplify the resulting relation obtaining Eq. (A.7). The form of the wave equation for $\vec{H}$ is identical as Eq. (A.7) and will not be explicitly given. The right-hand term in (A.7) is in general non-zero. However, due to the symmetry of the problem, $\partial \varepsilon(r)/\partial z$ vanishes. Hence, the components E_z and H_z can be solved first and E_r, H_r, E_ϕ and H_ϕ can be expressed in terms of E_z and H_z. For the next steps the form of the following operators in cylindrical coordinates will be useful:

$$[\vec{\nabla} \cdot \vec{A}]_{r,\phi,z} = \partial_r A_r + \frac{1}{r}\partial_\phi A_\phi + \partial_z A_z, \tag{A.8}$$

$$[\vec{\nabla} \times \vec{A}]_{r,\phi,z} = (\frac{1}{r}\partial_\phi A_z - \partial_z A_\phi)\hat{r} + (\partial_z A_r - \partial_r A_z)\hat{\phi} + (\partial_r A_\phi - \frac{1}{r}\partial_\phi A_r)\hat{z}, \tag{A.9}$$

$$[\nabla^2]_{r,\phi,z} = \partial_r^2 + \frac{1}{r}\partial_r + \frac{1}{r^2}\partial_\phi^2 + \partial_z^2. \tag{A.10}$$

Due to the geometry of the problem, the solutions of Eq. (A.7) for the z-component take the form of

$$E_z(\vec{r}, t) = E_z(r, \phi) \exp[i(\omega t - \beta z)], \tag{A.11}$$

where β is the axial propagation constant of the field. Substituting Eq. (A.11) into Eq. (A.7) and using Eq. (A.10) we obtain the wave equation in cylindrical coordinates

$$\left[\partial_r^2 + \frac{1}{r}\partial_r + \frac{1}{r^2}\partial_\phi^2 + (k^2 - \beta^2)\right]E_z(r, \phi) = 0, \tag{A.12}$$

where $k^2 = \mu_0 \varepsilon \omega^2$. This equation is separable with solutions of the form

$$E_z(r, \phi) = R(r) \exp[\pm il\phi], \tag{A.13}$$

where $l = 0, 1, 2, ...$ Then, Eq. (A.12) becomes the Bessel differential equation for the radial functions $R(r)$

$$\left[\partial_r^2 + \frac{1}{r}\partial_r + (k^2 - \beta^2 - \frac{l^2}{r^2})\right]R(r) = 0. \tag{A.14}$$

The general solutions of Eq. (A.14) are Bessel functions of order l depending on the sign of the magnitude $k^2 - \beta^2$:

If $k^2 - \beta^2 > 0$ then, $R(r) = c_1 J_l(hr) + c_2 Y_l(hr)$, with $h^2 = k^2 - \beta^2$, \quad (A.15)

If $k^2 - \beta^2 < 0$ then, $R(r) = c_3 I_l(qr) + c_4 K_l(qr)$, with $q^2 = \beta^2 - k^2$. \quad (A.16)

J_l denotes the Bessel function of the first kind, Y_l the Bessel function of the second kind, I_l the modified Bessel function of the first kind and K_l the modified Bessel function of the second kind, all of them of order l. Note that the axial propagation constant β of any lossless mode must lie within the range of values given by

$$n_2 k_0 \leq \beta \leq n_1 k_0, \tag{A.17}$$

where $k_0 = \omega/c$ is the wavevector of the propagating field in vacuum. Therefore, the solution will take the form of Eq. (A.15) for $r < a$, and the form of Eq. (A.16) for $r > a$. $\beta \leq n_2 k_0$ leads to another set of solutions where the fields do not only propagate axially, but also radially, i. e., leading to *lossy* fibre modes.

The fields must be finite as $r \to 0$. Since Y_l diverges for small arguments, we deduce that $c_2 = 0$. Analogously, the guided fields must vanish for large r. Since I_l diverges as $r \to \infty$, we deduce that $c_3 = 0$. Therefore, E_z and H_z can be expressed as

$$E_z(r, \phi, z, t) = A J_l(hr) \exp[i(\omega t \pm l\phi - \beta z)], \tag{A.18}$$
$$H_z(r, \phi, z, t) = B J_l(hr) \exp[i(\omega t \pm l\phi - \beta z)], \tag{A.19}$$
$$h = \sqrt{n_1^2 k_0^2 - \beta^2} \tag{A.20}$$

for $r < a$, and

$$E_z(r, \phi, z, t) = C K_l(qr) \exp[i(\omega t \pm l\phi - \beta z)], \tag{A.21}$$
$$H_z(r, \phi, z, t) = D K_l(qr) \exp[i(\omega t \pm l\phi - \beta z)], \tag{A.22}$$
$$q = \sqrt{\beta^2 - n_2^2 k_0^2} \tag{A.23}$$

for $r > a$. Using the expressions above together with Eqns. (A.2), (A.3) and (A.9), E_r, E_ϕ, H_r and H_ϕ can be expressed in terms of E_z and H_z.

For $r < a$:

$$E_r(r, \phi, z, t) = -\frac{\beta}{h}\left[iAJ_l'(hr) - \frac{\omega\mu_0(\pm l)}{\beta}B\frac{J_l(hr)}{hr}\right]\exp[i(\omega t \pm l\phi - \beta z)],$$

$$E_\phi(r, \phi, z, t) = \frac{\beta}{h}\left[(\pm l)A\frac{J_l(hr)}{hr} + \frac{i\omega\mu_0}{\beta}BJ_l'(hr)\right]\exp[i(\omega t \pm l\phi - \beta z)],$$

$$E_z(r, \phi, z, t) = AJ_l(hr)\exp[i(\omega t \pm l\phi - \beta z)], \tag{A.24}$$

$$H_r(r, \phi, z, t) = -\frac{\beta}{h}\left[iBJ_l'(hr) + \frac{\omega\varepsilon_1(\pm l)}{\beta}A\frac{J_l(hr)}{hr}\right]\exp[i(\omega t \pm l\phi - \beta z)],$$

$$H_\phi(r, \phi, z, t) = \frac{\beta}{h}\left[(\pm l)B\frac{J_l(hr)}{hr} - \frac{i\omega\varepsilon_1}{\beta}AJ_l'(hr)\right]\exp[i(\omega t \pm l\phi - \beta z)],$$

$$H_z(r, \phi, z, t) = BJ_l(hr)\exp[i(\omega t \pm l\phi - \beta z)], \tag{A.25}$$

where $J_l'(hr) = dJ(hr)/d(hr)$ and $\varepsilon_1 = n_1^2 \varepsilon_0$ is the dielectric constant inside the fibre.

For $r > a$:

$$E_r(r, \phi, z, t) = \frac{\beta}{q}\left[iCK_l'(qr) - \frac{\omega\mu_0(\pm l)}{\beta}D\frac{K_l(qr)}{qr}\right]\exp[i(\omega t \pm l\phi - \beta z)],$$

$$E_\phi(r, \phi, z, t) = -\frac{\beta}{q}\left[(\pm l)C\frac{K_l(qr)}{qr} + \frac{i\omega\mu_0}{\beta}DK_l'(qr)\right]\exp[i(\omega t \pm l\phi - \beta z)],$$

$$E_z(r, \phi, z, t) = CK_l(qr)\exp[i(\omega t \pm l\phi - \beta z)], \tag{A.26}$$

$$H_r(r,\phi,z,t) = \frac{\beta}{q}\Big[iDK_l'(qr) + \frac{\omega\varepsilon_2(\pm l)}{\beta}C\frac{K_l(qr)}{qr}\Big]\exp[i(\omega t \pm l\phi - \beta z)],$$

$$H_\phi(r,\phi,z,t) = -\frac{\beta}{q}\Big[(\pm l)D\frac{K_l(qr)}{qr} - \frac{i\omega\varepsilon_2}{\beta}CK_l'(qr)\Big]\exp[i(\omega t \pm l\phi - \beta z)],$$

$$H_z(r,\phi,z,t) = DK_l(qr)\exp[i(\omega t \pm l\phi - \beta z)], \tag{A.27}$$

where $K_l'(qr) = dK(qr)/d(qr)$ and $\varepsilon_2 = n_2^2\varepsilon_0$ denotes the dielectric constant in the surrounding medium. The term $\pm l$ in the exponential was introduced in Eqns. (A.13), the ansatz functions for the solution of the wave function in cylindrical coordinates. This leads to the solutions of the fields for circular polarisation, the $+$ $(-)$ sign corresponding to the solution for clockwise (counterclockwise) rotation of the transverse field $\vec{E}_\perp = (E_x, E_y)$ around the fibre axis. The solutions for linearly polarised light are obtained using another type of ansatz functions: $E_z(r,\phi) = R(r)\cos[l\phi]$ and $E_z(r,\phi) = R(r)\sin[l\phi]$. In addition, as shown in Sec. 1.2.1, the number l is related to the orbital angular momentum of the propagating electromagnetic field. This introduces an interesting relation between the polarisation of the field and its orbital angular momentum in optical fibres. The magnitudes A B, C, D and β, are determined by the boundary conditions and by the total power of the electromagnetic field given by

$$E_{\phi,z}(r=a)|_1 = E_{\phi,z}(r=a)|_2,$$
$$H_{\phi,z}(r=a)|_1 = H_{\phi,z}(r=a)|_2, \tag{A.28}$$

$$P = \frac{\omega}{2\pi}\int_0^{\frac{2\pi}{\omega}} dt \int_S S_z dS. \tag{A.29}$$

The sub-indices 1 and 2 in Eqns. (A.28) account for the regions where $r < a$ and $r > a$, respectively. P is the total power transmitted through the fibre and S_z is the component of the Poynting vector along the fibre axis. Imposing the boundary conditions given by (A.28) on Eqns. (A.24)–(A.27) the following relations for the constants A B, C and D are obtained:

$$AJ_l(ha) - CK_l(qa) = 0,$$

$$A\Big[\frac{i(\pm l)}{h^2 a}J_l(ha)\Big] + B\Big[-\frac{\omega\mu_0}{h\beta}J_l'(ha)\Big] + C\Big[\frac{i(\pm l)}{q^2 a}K_l(qa)\Big] + D\Big[-\frac{\omega\mu_0}{q\beta}K_l'(qa)\Big] = 0,$$

$$BJ_l(ha) - DK_l(qa) = 0,$$

$$A\Big[\frac{\omega\varepsilon_1}{h\beta}J_l'(ha)\Big] + B\Big[\frac{i(\pm l)}{h^2 a}J_l(ha)\Big] + C\Big[\frac{\omega\varepsilon_2}{q\beta}K_l'(qa)\Big] + D\Big[\frac{i(\pm l)}{q^2 a}K_l(qa)\Big] = 0. \tag{A.30}$$

Equations (A.30) lead to a nontrivial solution for the constants provided that the determinant of their coefficients equals zero [44]. This requirement leads to the mode condition that determines the propagation constant β for each mode,

$$\Big(\frac{J_l'(ha)}{haJ_l(ha)} + \frac{K_l'(qa)}{qaK_l(qa)}\Big)\Big(\frac{n_1^2 J_l'(ha)}{haJ_l(ha)} + \frac{n_2^2 K_l'(qa)}{qaK_l(qa)}\Big) = l^2\Big[\Big(\frac{1}{ha}\Big)^2 + \Big(\frac{1}{qa}\Big)^2\Big]^2\Big(\frac{\beta}{k_0}\Big)^2, \tag{A.31}$$

and to the relations between the constants A, B, C and D given by

$$\frac{C}{A} = \frac{J_l(ha)}{K_l(qa)},$$

$$\frac{B}{A} = \frac{i\beta(\pm l)}{\omega\mu_0}\left(\frac{1}{h^2 a^2} + \frac{1}{q^2 a^2}\right)\left(\frac{J_l'(ha)}{ha J_l(ha)} + \frac{K_l'(qa)}{qa K_l(qa)}\right)^{-1},$$

$$\frac{D}{A} = \frac{C}{A^2}\frac{B}{}.$$

(A.32)

Note that B/A is complex producing a relative phase of $\pi/2$ between E_r and E_ϕ and, thus circular polarisation of the transverse field. Finally, Eq. (A.29) allows the determination of A by imposing the desired power of the electromagnetic field. In practice P is measured with a photodetector at the output of the fibre.

List of Figures

List of Tables

Bibliography

[1] J. Ph. Poizat and P. Grangier, *Experimental realization of a quantum optical tap*, Phys. Rev. Lett. **70**, 271–274 (1993).

[2] G. Nogues, A. Rauschenbeutel, S. Osnaghi, M. Brune, J. M. Raimond and S. Haroche, *Seeing a single photon without destroying it*, Nature **400**, 239–242 (1999).

[3] S. Kuhr, W. Alt, D. Schrader, M. Müller, V. Gomer, and D. Meschede, *Deterministic Delivery of a Single Atom*, Science **293**, 278 (2001).

[4] H. J. Metcalf and P. van der Straten, *Laser cooling and trapping*, (Springer-Verlag, New York, 1999).

[5] L.-M. Duan, M. D. Lukin, I. J. Cirac, and P. Zoller, *Long-distance quantum communication with atomic ensembles and linear optics*, Nature **414**, 413–418 (2001).

[6] D. N. Matsukevich, T. Chanelière, M. Bhattacharya, S.-Y. Lan, S. D. Jenkins, T. A. B. Kennedy, and A. Kuzmich, *Entanglement of a Photon and a Collective Atomic Excitation*, Phys. Rev. Lett. **95**, 040405 (2005).

[7] S. Choi, H. Deng, J. Laurat, and H. J. Kimble, *Mapping photonic entanglement into and out of a quantum memory*, Nature **452**, 67–71 (2008).

[8] P. W. H. Pinkse, T. Fischer, P. Maunz, and G. Rempe, *Trapping an atom with single photons*, Nature **404**, 365–368 (2000).

[9] C. J. Hood, T. W. Lynn, A. C. Doherty, A. S. Parkins, and H. J. Kimble, *The Atom-Cavity Microscope: Single Atoms Bound in Orbit by Single Photons*, Science **287**, 5457 (2000).

[10] M. Khudaverdyan, W. Alt, I. Dotsenko, T. Kampschulte, K. Lenhard, A. Rauschenbeutel, S. Reick, K. Schörner, A. Widera, and D. Meschede, *Controlled insertion and retrieval of atoms coupled to a high-finesse optical resonator*, New J. Phys. **10**, 7 073023 (2008).

[11] J. M. Raimond, M. Brune, and S. Haroche, *Manipulating quantum entanglement with atoms and photons in a cavity*, Rev. of Mod. Phys. **73** (2001).

[12] T. Aoki, B. Dayan, E. Wilcut, W. P. Bowen, A. S. Parkins, T. J. Kippenberg, K. J. Vahala and H. J. Kimble, *Observation of strong coupling between one atom and a monolithic microresonator*, Nature **443**, 671–674 (2006).

[13] A. M. Armani, R. P. Kulkarni, S. E. Fraser, R. C. Flagan and K. J. Vahala, *Label-Free, Single-Molecule Detection with Optical Microcavities*, Science **317**, 5839 (2007).

[14] D. K. Armani, T. J. Kippenberg, S. M. Spillane and K. J. Vahala, *Ultra-high-Q toroid microcavity on a chip*, Nature **421**, 925–928 (2003).

[15] D. P. DiVincenzo, *The physical implementation of quantum computation*, Fortschr. Phys. **48**, 771 (2000).

[16] H. J. Carmichael, *Quantum trajectory theory for cascaded open systems*, Phys. Rev. Lett. **70**, 2273-2276 (1993).

[17] S. J. van Enk and H. J. Kimble, *Single atom in free space as a quantum aperture*, Phys. Rev. A **61**, 051802 (2000).

[18] N. Lindlein, R. Maiwald, H. Konermann, M. Sondermann, U. Peschel, and G. Leuchs, *A new 4π-geometry optimized for focusing onto an atom with a dipole-like radiation pattern*, Laser Physics **17**, 927-934 (2007).

[19] S. M. Iftiquar, *Application of photon scanning tunneling microscope to measure optical near field for atom manipulation*, Ultramicroscopy **103**, 109 (2005).

[20] D. Bloch, M. Ducloy, *Atom-Wall interaction*, Adv. At. Mol. Opt. Phys. **50**, (B. Bederson and H. Walther eds., Elsevier-Academic Press, 2005).

[21] Yu. B. Ovchinnikov, I. Manek, and R. Grimm, *Surface Trap for Cs atoms based on Evanescent-Wave Cooling*, Phys. Rev. Lett. **79**, 2225-2228 (1997).

[22] M. Hammes, D. Rychtarik, V. Druzhinina, U. Moslener, I. Manek-Hnninger, R. Grimm, *Optical and evaporative cooling of caesium atoms in the gravito-optical surface trap*, J. of Mod. Optics **47**, 14 2755-2767 (2000).

[23] V. V. Ivanov, R. A. Cornelussen, H. B. van Linden van den Heuvell, and R. J. C. Spreeuw, *Observation of modified radiative properties of cold atoms in vacuum near a dielectric surface*, J. Opt. B: Quantum Semiclass. Opt. **6**, 454 (2004).

[24] V. I. Balykin, V. S. Letokhov, Yu. B. Ovchinnikov, and A. I. Sidorov, *Quantum-State-Selective Mirror Reflection of Atoms by Laser Light*, Phys. Rev. Lett. **60**, 2137-2140 (1988).

[25] N. Westbrook, C. I. Westbrook, A. Landragin, G. Labeyrie, L. Cognet, V. Savalli, G. Horvath, A. Aspect, C. Hendel, K. Moelmer, J.-Y. Courtois, W. D. Phillips,

R. Kaiser, and V. Bagnato, *New Physics with Evanescent Wave Atomic Mirrors: The van der Waals Force and Atomic Diffraction*, Physica Scripta. **78**, 712 (1998).

[26] J. P. Dowling and J. Gea-Banacloche, *Evanescent Light-Wave Atom Mirrors, Resonators, Waveguides, and Traps*, Adv. At. Mol. Opt. Phys. **37**, 1 (1996).

[27] A. H. Barnett, S. P. Smith, M. Olshanii, K. S. Johnson, A. W. Adams, and M. Prentiss, *Substrate-based atom waveguide using guided two-color evanescent light fields*, Phys. Rev. A **61**, 023608 (2000).

[28] J. P. Burke Jr., Sai-Tak Chu, G. W. Bryant, C. J. Williams, and P. S. Julienne, *Designing neutral-atom nanotraps with integrated optical waveguides*, Phys. Rev. A **65**, 043411 (2002).

[29] A. W. Snyder, J. D. Love, *Optical Waveguide Theory*, (Kluwer Academic Publishers, London, 2000).

[30] T. Legero, T. Wilk, M. Hennrich, G. Rempe, and A. Kuhn, *Quantum Beat of Two Single Photons*, Phys. Rev. Lett. **93**, 7 (2004).

[31] A. Muller, H. Zbinden and N. Gisin, *Quantum cryptography over 23 km in installed under-lake telecom fibre*, Europhys. Lett. **33**, 335-340 (1996).

[32] Y. Colombe, T. Steinmetz, G. Dubois, F. Linke, D. Hunger, and J. Reichel, *Strong atom-field coupling for Bose-Einstein condensates in an optical cavity on a chip*, Nature **450**, 272–276 (2007).

[33] F. Warken, E. Vetsch, D. Meschede, M. Sokolowski, and A. Rauschenbeutel, *Ultrasensitive surface absorption spectroscopy using sub-wavelength diameter optical fibers*, Optics Express **15**, 19 11952-11958 (2007).

[34] K. P. Nayak *et al.*, *Optical nanofiber as an efficient tool for manipulating and probing atomic fluorescence*, Optics Express **15**, 9 5431 (2007).

[35] G. Sagué, E. Vetsch, W. Alt, D. Meschede and A. Rauschenbeutel, *Cold Atom Physics Using Ultra-Thin Optical Fibers: Light-Induced Dipole Forces and Surface Interactions*, Phys. Rev. Lett. **99**, 163602 (2007).

[36] F. Warken, *Ultradünne Glasfasern als Werkzeug zur Kopplung von Licht und Materie*, Ph.D. thesis, Rheinische Friedrich-Wilhelms Universität, Bonn (2007).

[37] F. Le Kien, J. Q. Liang, K. Hakuta, and V. I. Balykin, *Field intensity distributions and polarization orientations in a vacuum-clad subwavelength-diameter optical fiber*, Opt. Commun. **242**, 445 (2004).

[38] Fam Le Kien, S. Dutta Gupta, V. I. Balykin, and K. Hakuta, *Spontaneous emission of a cesium atom near a nanofiber: Efficient coupling of light to guided modes*, Phys. Rev. A **72**, 032509 (2005).

[39] Fam Le Kien, V. I. Balykin, and K. Hakuta, *Atom trap and waveguide using a two-color evanescent light field around a subwavelength-diameter optical fiber* Phys. Rev. A **70**, 063403 (2004).

[40] A. K. Patnaik, J. Q. Liang, and K. Hakuta, *Slow light propagation in a thin optical fiber via electromagnetically induced transparency*, Phys. Rev. A **66**, 063808 (2002).

[41] C. Ottaviani, S. Rebić, D. Vitali, P. Tombesi, *Quantum phase-gate operation based on nonlinear optics: Full quantum analysis*, Phys. Rev. A **73**, 010301(R) (2006).

[42] E. Hecht, *Óptica*, (Addison Wesley Iberoamericana, Madrid, 2000).

[43] I. H. Malitson, *Interspecimen Comparison of the Refractive Index of Fused Silica*, J. Opt. Soc. Am. **55**, 1205-1208 (1965).

[44] A. Yariv, *Optical Electronics*, (Sanders College Publishing, Philadelphia, 1991).

[45] J. Bures and R. Ghosh, *Power density of the evanescent field in the vicinity of a tapered fiber*, J. Opt. Soc. Am. A **16**, 8 (1999).

[46] Fam Le Kien, V. I. Balykin, and K. Hakuta, *Angular momentum of light in an optical nanofiber*, Phys. Rev. A **73**, 053823 (2006).

[47] F. Warken und A. Rauschenbeutel, in preparation.

[48] F. Orucevic, V. Lefevre-Seguin, J. Hare, *Transmittance and Near-Field Characterization of Sub-Wavelength Tapered Optical Fibers*, Optics Express **15**, 21 13625 (2007).

[49] J. D. Love and W. M. Henry, *Quantifying loss minimisation in single-mode fibre tapers*, Electron. Lett. **22**, 921 (1986).

[50] J. D. Jackson, *Classical electrodynamics*, (Wiley, New York, 1962).

[51] A. Ashkin, *Trapping of Atoms by Resonance Radiation Pressure*, Phys. Rev. Lett. **40**, 729 (1978).

[52] D. A. Steck, *Cesium D Line Data* (23 January 1998, Revision 1.5, 21 November 2002), http://steck.us/alkalidata/.

[53] D. Schrader, *A neutral atom quantum register*, Ph.D. thesis, Rheinische Friedrich-Wilhelms Universität, Bonn (2004).

[54] A. Messiah, *Quantum Mechanics*, (Volume II), 12th edition, (North Holland Publishing, New York, 1981).

[55] Fam Le Kien, V. I. Balykin, K. Hakuta, *State-Insensitive Trapping and Guiding of Cesium Atoms Using a Two-Color Evanescent Field around a Subwavelength-Diameter Fiber*, J. Phys. Soc. Jpn. **74**, 3 910-917(2005).

[56] M. Boustimi, J. Baudon, P. Candori, and J. Robert, *van der Waals interaction between an atom and a metallic nanowire*, Phys. Rev. B **65**, 155402 (2002).

[57] V. V. Klimov and M. Ducloy, *Spontaneous emission rate of an excited atom near a nanofibre*, Phys. Rev. A **69**, 013812 (2004).

[58] P. Maunz, T. Puppe, T. Fischer, P. W. H. Pinkse, and G. Rempe, *Emission pattern of an atomic dipole in a high-finesse optical cavity*, Optics Letters **28**, 1 (2003).

[59] Newport Corporation, www.newport.com

[60] C. G. Townsend, N. H. Edwards, C. J. Cooper, K. P. Zetie, and C. J. Foot, A. M. Steane, P. Szriftgiser, H. Perrin, and J. Dalibard, *Phase-space density in the magneto-optical trap*, Phys. Rev. A **52**, 1423 (1995).

[61] A. Höpe, D. Haubrich, G. Müller, W. G. Kaenders and D. Meschede, *Neutral Cesium Atoms in Strong Magnetic-Quadrupole Fields at Sub-Doppler Temperatures*, Europhys. Lett. **22**, 669-674 (1993).

[62] M.-O. Mewes, M. R. Andrews, N. J. van Druten, D. S. Durfee, D. M. Kurn, and W. Ketterle, *Bose-Einstein Condensation in a Gas of Sodium Atoms*, Phys. Rev. Lett. **75**, 22 (1995).

[63] M. Greiner, O. Mandel, T. Esslinger, T.W. Hänsch, and I. Bloch, *Quantum Phase Transition from a Superfluid to a Mott Insulator in a Gas of Ultracold Atoms*, Nature **415**, 39–44 (2002).

[64] S. Chu, L. Hollberg, J. E. Bjorkholm, A. Cable, and A. Ashkin, *Three-dimensional Viscous Confinement and Cooling of Atoms by Resonance Radiation Pressure*, Phys. Rev. Lett. **55**, 48 (1985).

[65] E. L. Raab, M. Prentiss, A. Cable, S. Chu, and D. E. Pritchard, *Trapping of Neutral Sodium Atoms with Radiation Pressure*, Phys. Rev. Lett. **59**, 2631 (1987).

[66] J. Dalibard and C. Cohen-Tannoudji, *Laser cooling below the Doppler limit by polarization gradients: simple theoretical models*, JOSA B **6**, 11 2023-2045 (1998).

[67] A. L. Migdall, J. V. Prodan, and W. D. Phillips, T. H. Bergeman and H. J. Metcalf, *First Observation of Magnetically Trapped Neutral Atoms*, Phys. Rev. Lett. **54**, 2596-2599 (1985).

[68] K. G. Libbrecht, R. A. Boyd, P. A. Willems, T. L. Gustavson, and D. K. Kim, *Construction of Stabilized Lasers and Lithium Cells*, Am. J. Phys. **63**, 729 (1995).

[69] W. Demtröder, *Laserspektroskopie*, (Springer-Verlag, Berlin, 1993).

[70] E. R. I. Abraham and E. A. Cornell, *Teflon feedthrough for coupling optical fibers into ultrahigh vacuum systems*, Applied Optics **37** 10 (1998).

[71] W. Alt, *Optical control of single neutral atoms*, Ph.D. thesis, Rheinische Friedrich-Wilhelms Universität, Bonn (2004).

[72] K. C. Harvey and C. J. Myatt, *External-cavity diode laser using a grazing-incidence diffraction grating*, Opt. Lett. **16**, 910 (1991).

[73] T. M. Brzozowski, M. Maczazyńska, M. Zawada, J. Zachorowski and W. Gawlik, *Time-of-flight measurement of the temperature of cold atoms for short trap-probe distances*, J. Opt. B: Quantum Semiclass. Opt. **4**, 62-66 (2002).

[74] T. Passerat de Silans, B. Farias, M. Oriá, M. Chevrollier, *Laser-induced quantum adsorption of neutral atoms in dielectric surfaces*, Appl. Phys. B **82**, 367-371 (2006).

[75] A. Laliotis *et al.*, *Testing the distance-dependence of the van der Waals interaction between an atom and a surface through spectroscopy in a vapor nanocell*, Proc. of SPIE **6604**, 660406-1 (2007).

[76] A. Derevianko, W. R. Johnson, M. S. Safronova and J. F. Babb, *High-Precision Calculations of Dispersion Coefficients, Static Dipole Polarizabilities, and Atom-Wall Interaction Constants for Alkali-Metal Atoms*, Phys. Rev. Lett. **82** 18 3589 - 3592 (1999).

[77] M. Fichet *et al.*, *Exploring the van der Waals atom-surface attraction in the nanometric range*, Europhys. Lett. **77**, 54001 (2007).

[78] L. Spruch, Y. Tikochinsky, *Elementary approximative derivations os some retarded Casimir interactions involving one or two dielectric walls*, Phys. Rev. A **48**, 6 (1993).

[79] E. A. Hinds and V. Sandoghdar, *Cavity QED level shifts of simple atoms*, Phys. Rev. A **43**, 398 - 403 (1991).

[80] O. Keller, M. Xiao and S. Bozhevolnyi, *Configurational resonances in optical near-field microscopy: a rigorous point-dipole approach*, Surf. Sci. **280**, 217-230 (1993).

[81] V. I. Balykin, K. Hakuta, Fam Le Kien, J. Q. Liang, and M. Morinaga, *Atom trapping and guiding with a subwavelength-diameter optical fiber*, Phys. Rev. A **70**, 011401(R) (2004).

[82] P. T. Greenland, M. A. Lauder, and D. J. H. Wort, *Atomic beam velocity distributions*, J. Phys. D: Appl. Phys **18**, 1223-1232 (1985).

[83] S. M. Hendrickson, T. B. Pittman and J. D. Franson, *Nonlinear transmission through a tapered fiber in rubidium vapor*, quant-ph/0808.3932 (2008).

[84] S. Kuhr, *A controlled quantum system of individual neutral atoms*, Ph.D. thesis, Rheinische Friedrich-Wilhelms Universität, Bonn (2003).

[85] M. D. Barrett, J. A. Sauer and M. S. Chapman, *All-Optical Formation of an Atomic Bose-Einstein Condensate*, Phys. Rev. Lett. **87**, 010404 (2001).

[86] S. Jochim, M. Bartenstein, A. Altmeyer, G. Hendl, S. Riedl, C. Chin, J. Hecker Denschlag, and R. Grimm, *Bose-Einstein Condensation of Molecules*, Science express 1093280 (2003).

[87] D. Schrader, I. Dotsenko, M. Khudaverdyan, Y. Miroshnychenko, A. Rauschenbeutel, and D. Meschede, *Neutral Atom Quantum Register*, Phys. Rev. Lett. **93**, 150501 (2004).

[88] P. Grangier, G. Reymond, N. Schlosser, *Implementations of Quantum Computing Using Cavity Quantum Electrodynamics Schemes*, Fortschr. Phys. **48**, 9-11 (2000).

[89] http://www.fujikura.co.uk/fibre_optics/products/speciality_fibre/panda_fibre.html

[90] Fam Le Kien and K. Hakuta, *Position distribution of cold thermal atoms in the vicinity of a dielectric surface*, Phys. Rev. A **77**, 042903 (2008).

[91] M. Hammes, D. Rychtarik, H.-C. Nägerl, and R. Grimm, *Cold-atom gas at very high densities in an optical surface microtrap*, Phys. Rev. A **66**, 051401 (2002).

[92] Fam Le Kien, S. Dutta Gupta, and K. Hakuta, *Phonon-mediated decay of an atom in a surface-induced potential*, Phys. Rev. A **75**, 062904 (2007).

[93] G. Sagué, A. Baade and A. Rauschenbeutel, *Blue-detuned evanescent field surface traps for neutral atoms based on mode interference in ultra-thin optical fibres*, arXiv:0806.3909, Accepted for publication in New J. Phys. (2008).

Agraïments/Danksagung

Vull agraïr a la meva família el suport incondicional que sempre m'han donat. Durant la meva infantesa em van donar l'oportunitat de créixer en un hogar feliç. Durant la meva adolescència em van inculcar els valors de l'esforç i de la constància per a aconseguir els objectius desitjats. Malauradament, vaig haber d'esperar a la joventut per descobrir-ho per mi mateix. En la jove maduresa que visc actualment miro enrera i agraeixo de tot cor a la meva mare Rosa Maria i al meu pare Jaume que m'hagin donat tot el que ara soc. Menció a part mereix el meu germà. Ell ha suportat estoïcament els meu erràtic aprenentatge de l'ofici de germà gran. La seva alegria i la manera positiva que té d'encarar la vida sempre em sorprendran.

Als ich vor weniger als vier Jahren nach Deutschland kam verabschiedete ich mich von meiner Großmutter und dabei brachte sie mir meine ersten zwei Wörter auf Deutsch bei "*Guten Tag*, das kannst du immer anwenden" hat sie gesagt. Seitdem ist viel Wasser den Rhein hinunter geflossen. Ich habe eine neue Sprache und eine neue Kultur kennengelernt, die für mich damals genau so fremd waren wie ich sie jetzt als meine eigene schätze. Das ist der Verdienst der Leute, die ich in Deutschland und insbesondere im IAP in Bonn und im Institut für Physik in Mainz kennengelernt habe. Damit meine ich vor allem die Menschen, die mit mir die Lebenserfahrung einer Doktorarbeit gemeinsam erlebt haben: Mika Khudaverdian, Michael Haas, Florian Warken, Yevhen Miroshnychenko − die Liste ist einfach zu lang −. Besonders möchte ich mich bei Eugen Vetsch bedanken. Er hat Tag und Nacht Hand in Hand mit mir an dem Experiment gearbeitet und dadurch hat sich eine feste Freundschaft entwickelt. Diese Kombination hat zu dem Erfolg des Experiments geführt. Alldies wäre auch nicht möglich gewesen ohne die Beratung und Unterstützung von Wolfgang Alt und Dietmar Haubrich. Mittlerweile gibt es eine neue Generation von Physiker, die das Experiment entwickeln. Daniel Reitz und Regine Schmidt arbeiten jetzt mit Eugen zusammen und leisten eine hervorragende Arbeit. Das gibt mir das erleichternde Gefühl, dass das Experiment in guten Händen ist. Alex Baade hat als Diplomand mit mir zusammen gearbeitet und eine aussergewöhnliche Arbeitsfähigkeit gezeigt. Ruth García hat mit ihrer unendlichen Geduld meine Dissertation gelesen und korrigiert, außerdem hat sie mich auch persönlich unterstützt. Bei allen diesen Menschen möchte ich mich herzlichst bedanken.

Ganz besonders möchte ich mich bei meinen zwei Betreuern bedanken: Prof. Meschede und Prof. Rauschenbeutel. Beide haben mir die Möglichkeit gegeben, in einem höchst innovativen Experiment zu promovieren und die Kenntnisse der Quantenoptik ein bisschen zu erweitern. Bei Prof. Meschede bedanke ich mich dafür, dass er so eine multikulturelle Arbeitsgruppe leitet, wo Menschen aus der ganzen Welt über die Sprache der Physik intereagieren. Dort habe ich mich sehr wohl gefühlt. Bei Prof. Rauschenbeutel möchte ich mich aus zweierlei Gründen bedanken: Zum einen hat er mich im persönlichen Bereich immer sehr unterstützt, und zum anderen ist er immer ein ausführlicher Prüfer und optimaler Berater gewesen.

Zu Guter Letzt, möchte ich mich bei meiner Freundin Genia ganz herzlich bedanken. Sie hat vorallem in der letzen Zeit sehr wenig von mir gehabt und mir trotzem sehr viel gegeben.